UNIVERSITÀ DEGLI STUDI DI NAPOLI
"FEDERICO II"

DOTTORATO IN FISICA FONDAMENTALE ED APPLICATA

XXIII CICLO

DIPARTIMENTO DI SCIENZE FISICHE

Ph. D. T H E S I S

Defended by

Vito PALLADINO

Simulation, realization and test of veto systems for the NA62 experiment

Coordinator : Prof. Lorenzo MARRUCCI
Advisor : Dr. Fabio AMBROSINO

Accademic Year 2009/2010

To whom near and far

Acknowledgments

It is a pleasure to thank those who made this thesis possible.

I am heartily thankful to Dr. Fabio Ambrosino, Dr. Giulio Saracino and Prof. Marco Napolitano, whose encouragement, guidance and support from the initial to the final level enabled me to develop an understanding of the subject. My deepest gratitude is also due to Paolo Massarotti how was a constant presence and a irreplaceable friend all along these three years. I am grateful to Mimmo for all chats. A special thanks to Valeri Falaleev for his constant support during my stay at CERN and to all NA62 photon veto working group. Not forgetting Naples MuRAY group without whose help this study would not have been successful.

I wold like to thank my family for support and patience.

All my best friends who always been there.

Last but not least Angelica for her love.

Lastly, I offer my regards to all of those who supported me in any respect during the completion of the project.

Thank you,

Vito.

Contents

Introduction iii

1 Standard Model tests with rare kaon decays 3
1.1 CKM matrix . . . 3
1.1.1 Standard parametrization . . . 4
1.1.2 Wolfenstein parametrization . . . 4
1.1.3 Unitarity Triangle . . . 5
1.2 $K \to \pi\nu\bar{\nu}$ rare decays . . . 6
1.2.1 B($K^+ \to \pi^+\nu\bar{\nu}$) and relative uncertainties . . . 7
1.2.2 B($K_L^0 \to \pi^0\nu\bar{\nu}$) and relative uncertainties . . . 8
1.2.3 Experimental status . . . 9
1.2.4 Sensitivity to New Physics . . . 9
1.3 R_K in Standard Model and beyond . . . 10
1.3.1 Experimental Status . . . 11
1.4 NA62 Phase I . . . 11
1.4.1 Apparatus, Trigger Logic and Measurement Strategy . . . 13
1.4.2 Signal Selection and Main Background . . . 13
1.4.3 Preliminary result . . . 15
1.4.4 Future prospective . . . 15

2 The NA62 experiment 17
2.1 General strategy . . . 17
2.1.1 Tracking system . . . 18
2.1.2 Timing . . . 21
2.1.3 Veto system . . . 21
2.1.4 Particle Identification . . . 22
2.1.5 Summary of Detectors Layout . . . 24
2.2 Beam Line . . . 25
2.3 CEDAR . . . 25
2.4 Gigatracker . . . 28
2.5 STRAW chamber . . . 29
2.6 RICH . . . 33
2.7 Photon Veto system . . . 36
2.7.1 Large Angle Veto . . . 36
2.7.2 Liquid Krypton electro-magnetic calorimeter . . . 37
2.7.3 IRC and SAC Calorimeters . . . 37
2.8 MUon Veto . . . 41
2.9 CHarged ANTIcounter . . . 43
2.10 CHarged hODoscope . . . 43
2.11 Trigger and Data AcQuisition . . . 44

3 Large Angle photon Veto system **47**
3.1 Technology choice . . . 48
3.2 Prototypes test and results comparison . . . 49
3.2.1 Readout and data acquisition . . . 49
3.2.2 Beam Tagging System . . . 50
3.2.3 KLOE like and CKM prototype tests . . . 52
3.2.4 exOPAL prototype test . . . 56
3.2.5 Conclusions . . . 60
3.3 General layout . . . 63
3.3.1 Basic block . . . 63
3.4 Cleaning and test procedures . . . 64
3.4.1 Clean Procedure . . . 64
3.4.2 Test Procedure . . . 65
3.4.3 Problems Found . . . 65
3.5 LAV Station realization . . . 69
3.5.1 Gain curve measurement and equalization . . . 70
3.6 Module construction . . . 74
3.7 Preparation and installation of the blocks into the cylinder . . . 75
3.7.1 Readout electronics . . . 77
3.8 ANTI-A1 test beam . . . 78
3.8.1 Results . . . 78
3.8.2 Conclusions . . . 86

4 CHarged ANTIcounter **89**
4.1 Requirements . . . 89
4.2 General Layout . . . 90
4.3 Basic Scintillator Layout . . . 92
4.4 Mechanics and Supports . . . 94
4.5 Photodetectors . . . 98
4.6 Prototype construction . . . 101
4.7 Read-out . . . 108
4.7.1 Front End Electronics . . . 110
4.8 Preliminary prototype test . . . 110
4.9 Simulation . . . 113
4.9.1 Efficiency . . . 113
4.9.2 Data Rate . . . 118
4.9.3 Fake veto percentage . . . 121

Conclusions **123**

A Solid State Photon Detector **125**
A.1 Introduction . . . 125
A.2 Photon detectors with internal gain . . . 125
A.2.1 Avalanche PhotoDiode (APD) . . . 125

A.2.2 Geiger-mode Avalanche PhotoMultiplier (G-APD) 127
A.3 Main SiPM features and physical phenomena 127
A.3.1 Photon Detection Efficiency (PED) and Gain 127
A.3.2 Dark current, afterpulses and optical cross talk 130
A.3.3 Nuclear counter effect and radiation hardness 131
A.3.4 Signal shape 131

Bibliography **133**

Introduction

During my PhD course I have been involved in research activities into the frame of the NA62 experiment, which main goal is the measurement of the branching fraction B($K^+ \to \pi^+ \nu\bar{\nu}$). NA62 is a very challenging experiment due to ultra rare nature of this decay (BR $\sim 8\times10^{-11}$). The study of the decay $K^+ \to \pi^+ \nu\bar{\nu}$ is very important because it allows the first direct measurement of CKM element V_{td}. Moreover it could provide signals of physics beyond Standard Model (SM) as that decay is highly sensitive to new physics.

The experiment will be located at CERN experimental SPS North Area (hence the acronym NA). It is a fixed target experiment done using a unseparated 75 GeV/c beam of positive hadrons, produced by a 400 GeV/c proton beam. K^+, although being only 6% of the beam, are produced in a very abundant fashion, and will allow us to collect enough statistics to reach a $\sim$10% relative uncertainty after a 2 years long data taking. To reach such level of uncertainty and to keep signal/background ratio below 10, the apparatus is designed in order to provide both particle identification and kinematical rejection.

My work was focused on two veto subsystems with different scope, different architecture and different dimensions: the Large Angle photon Veto (or LAV) and the CHarged ANTIcounter (or CHANTI).

The LAV is made of 12 different stations all along the decay region. Each station is ring shaped. The main task of LAV is to veto photons from π^0 decay with an inefficiency lower than 10^{-4}, to reduce background from $K^+ \to \pi^+\pi^0$. In order to choose the best technology to implement the detector we have had an intense R&D program. Three different prototypes were tested and finally a solution that uses lead glass blocks from former OPAL electromagnetic calorimeter was chosen. The prototype used to measure inefficiency was made in Naples and tested at Laboratori Nazionali di Frascati beam test facility with electrons of energy between 300 and 500 MeV/c. Unfortunately the area at CERN where blocks were stored was flooded and all blocks were involved. This major event forced a massive recovering campaign, of which I was responsible. During recovering operations many problems were found and (most of them) solved. However not all flooded blocks may be used for LAV. Part of them were damaged (9%) and an other part showed an abnormal behaviour. During the recovering operation the design of the LAV was refined and construction started. In order to reduce costs we opted for a read-out electronics based on Time over Threshold (ToT) technique. The first station out of 12 was realized and tested at CERN in June-September 2009. It was an important mile stone. The test was intended, basically, as confirmation of ToT usefulness and as check of off-line equalization procedure that each block needes to pass before being mounted. To test ToT, signals were splitted and read on one side by custom ToT electronics and from the other side by a commercial CAEN QDC, in order to produce a ToT versus charge curve. Surprisingly not a unique curve was found. After an accurate data

analysis the problem was isolated and a solution proposed, consisting in changing the HV dividers of all blocks. A second module was built with new dividers and tested again at CERN. Preliminary data analysis (still going) is showing that the problem is solved and ToT can be used as read-out solution.

The other item I was involved on is the CHANTI project. It is a small detector that will be placed just after last station of incoming Kaon tracking system (called Giga TracKer or GTK). GTK is made of three silicon station hit by the 800 MHz incoming beam of hadrons. About 0.3% of particles crossing the GTK undergo in inelastic collision in which the incoming hadron strongly interacts with a nuclei of GTK station producing many particles, among them pions. If inelastic events involves the third station a signal event could be mimicked if only a pion is detected. CHANTI aims to veto these events detecting the cloud of particles produced together with pion. It is made by a series of guard ring made by X and Y scintillating bars planes. Bars have a triangular shape, thus are naturally staggered. Each bar is read through a Wave Length Shifter fiber coupled to a Silicon PhotoMultiplier (SiPM). A detailed Monte Carlo was adopted to improve geometry design and to estimate the efficiency of CHANTI; moreover neutron fluence, crucial if SiPM are to be used, was estimated. Finally we designed and constructed a first full size prototype. Preliminary results about response and time resolution have been done using cosmic rays.

The plan of the thesis is as follows.

First two chapters introduce the motivation for NA62 experiment, give an almost detailed description of the apparatus and present the measurement strategy.

The third chapter is dedicated to LAV. The comparison of the three different technologies, considered for ring implementation, and the reasons for choosing the lead glass solution are reported. The block recovery and the construction procedure are described in detail as well as tests done using a prototype and the first full size ring.

The work done for CHANTI is described in the fourth chapter, starting with simulation that helped to define geometry and to obtain information about data rate, inefficiency and neutron fluence. The construction procedure is then described and first results about response and time resolution are reported.

I reported on the arguments treated in this thesis at the following international conferences: CALOR08, 14th Lomonosov Conference and IEEE NSC '09. Moreover the discussion on CHANTI contained on technical design report of NA62 (published as CERN document) is largely based on the third chapter of this thesis.

Chapter 1

Standard Model tests with rare kaon decays

The Standard Model (SM) is, up to now, the best description of elementary interactions and particles we have. SM was able to explain many phenomena, and many others were predicted. Proofs that SM is a good description of real life up to energies reached in laboratory up to now, are, for example, the prediction of top mass value, the intermediate bosons of weak interaction hypothesis, the running coupling constant, etc.

However there are some open questions that are not well understood and for which SM has no answers. Examples are: electric charge quantization, gravity, hierarchy, etc. But also the high number of parameters suggests that SM needs to be "updated" and a different theory developed.

Nowadays LHC experiments are pushing on the border of our knowledge increasing the energy scale. This is one way to stress SM and search for new physics evidences. However this is not the only way. New physics could appear also if precision measurements of very precisely predicted parameters are done. Of course this could give only indirect proofs, however it could be just enough to discriminate between different theories.

On example of those kind of measurements, is the $K^+ \to \pi^+ \nu\bar{\nu}$ Branching Ratio (BR) and its neutral mode. It could be one way to stress SM, and at the same time have evidence of new physics, with high precise measurements. Moreover it has the potential to determine, for the first time, directly the V_{td} element of CKM matrix.

1.1 CKM matrix

The CKM matrix connects the weak eigenstates (d', s', b') and the corresponding mass eigenstates d, s, b (in both basis the up-type mass matrix is diagonal and the up-type quarks are unaffected by this transformation):

$$\begin{pmatrix} d'_L \\ s'_L \\ b'_L \end{pmatrix} = \begin{pmatrix} V_{ud} & V_{us} & V_{ub} \\ V_{cd} & V_{cs} & V_{cb} \\ V_{td} & V_{ts} & V_{tb} \end{pmatrix} \begin{pmatrix} d_L \\ s_L \\ b_L \end{pmatrix} = V_{CKM} \begin{pmatrix} d_L \\ s_L \\ b_L \end{pmatrix} \tag{1.1}$$

The CKM matrix contains all the flavor-changing and CP-violating couplings of the Standard Model. It is a unitary matrix if the number of quark families is three. Several parameterizations of the CKM matrix have been proposed in the literature.

1.1.1 Standard parametrization

If $c_{ij} = cos\theta_{ij}$ and $s_{ij} = sin\theta_{ij}$ (i, j = 1, 2, 3), the standard parametrization is given by:

$$V_{CKM} = \begin{pmatrix} c_{13}s_{13} & c_{13}s_{12} & s_{13}e^{-i\delta} \\ -c_{13}s_{12} & c_{12}c_{23} - s_{12}s_{23}s_{13}e^{i\delta} & c_{13}s_{23} \\ s_{12}s_{23} - c_{12}c_{23}s_{13}e^{i\delta} & -s_{23}c_{12} - s_{12}c_{23}s_{13}e^{i\delta} & c_{13}c_{23} \end{pmatrix} \tag{1.2}$$

where δ is the phase CP violating phase. All the parameters c_{ij} and s_{ij} can be chosen to be positive and δ may vary in the range [0,2π]. However, measurements of CP violation in K decays force δ to be in the range [0,π]. From phenomenological studies we know that s_{13} and s_{23} are small numbers, consequently, to a very good accuracy we can say:

$$s_{12} \equiv |V_{us}|,\ s_{13} \equiv |V_{ub}|,\ s_{23} \equiv |V_{cb}|. \tag{1.3}$$

this means that we can chose as our independent parameters:

$$|V_{us}|,\ |V_{ub}|,\ |V_{cb}|,\ \delta. \tag{1.4}$$

These three parameters can be extracted from tree level decays mediated by the transitions s→u, b→u and b→c, respectively. The remaining parameter, the phase δ, responsible for the violation of the CP symmetry, can be extracted from CP-violating transitions but also from CP-conserving ones, using three-generation unitarity [8].

1.1.2 Wolfenstein parametrization

The absolute values of the elements of the CKM matrix show a hierarchical pattern with the diagonal elements being close to unity, the elements $|V_{us}|$ and $|V_{cd}|$ being of order 0.2, the elements $|V_{cb}|$ and $|V_{ts}|$ of order 4×10^{-2} whereas $|V_{ub}|$ and $|V_{td}|$ are of order 5×10^{-3}. The Wolfenstein parametrization [45] exhibits this hierarchy in a transparent manner. It is an approximate parametrization of the CKM matrix in which each element is expanded as a power series in the small parameter $\lambda \sim |V_{us}| = 0.22$, with this assumption:

$$V_{CKM} = \begin{pmatrix} 1 - \frac{1}{2}\lambda^2 & \lambda & A\lambda^3(\rho - i\eta) \\ -\lambda & 1 - \frac{1}{2}\lambda^2 & \lambda^2 A \\ A\lambda^3(1 - \rho - i\eta) & -\lambda^2 A & 1 \end{pmatrix} + o(\lambda^4). \tag{1.5}$$

parameters set in 1.4 is replaced by

$$\lambda,\ A,\ \rho,\ \eta \tag{1.6}$$

Because of the smallness of λ and the fact that for each element the expansion parameter is actually λ^2, this is a rapidly converging expansion.

The Wolfenstein parametrization is, certainly, more transparent than the standard parametrization. However, if one requires sufficient level of accuracy, the terms of $O(\lambda^4)$ and $O(\lambda^5)$ have to be included in phenomenological applications. Following this idea we introduce the modified parameters:

$$\begin{aligned} \bar{\rho} &= \rho(1-\lambda^2/2) \\ \bar{\eta} &= \eta(1-\lambda^2/2) \end{aligned} \tag{1.7}$$

using these new definition we can write down the CKM matrix with an approximation of $O(\lambda^6)$:

$$V_{CKM} = \begin{pmatrix} 1-\lambda^2/2-\lambda^4/8 & \lambda+O(\lambda^7) & A\lambda^3(\rho-i\eta) \\ -\lambda+A^2\lambda^5(1-2(\rho-i\eta))/2 & 1-\lambda^2/2-\lambda^4(1+4A^2)/8 & A\lambda^2+O(\lambda^8) \\ A\lambda^3(1-\bar{\rho}-i\bar{\eta}) & -A\lambda^2+A\lambda^4(1-2(\rho-i\eta))/2 & 1-A^2\lambda^4 \end{pmatrix} \tag{1.8}$$

The advantage of this generalization of the Wolfenstein parametrization is the absence of relevant corrections to V_{us}, V_{cd}, V_{ub} and V_{cb} and an elegant change in V_{td} which allows a simple connection to the Unitarity Triangle parameters, as discussed below.

1.1.3 Unitarity Triangle

Since CKM matrix is unitary, this implies various (12) relations between its elements:

$$\begin{aligned} |V_{ud}|^2+|V_{us}|^2+|V_{ub}|^2 &= 1 \\ |V_{cd}|^2+|V_{cs}|^2+|V_{cb}|^2 &= 1 \\ |V_{td}|^2+|V_{ts}|^2+|V_{tb}|^2 &= 1 \\ |V_{ud}|^2+|V_{cd}|^2+|V_{td}|^2 &= 1 \\ |V_{us}|^2+|V_{cs}|^2+|V_{ts}|^2 &= 1 \\ |V_{ub}|^2+|V_{cb}|^2+|V_{tb}|^2 &= 1 \end{aligned} \tag{1.9}$$

and

$$\begin{aligned} V_{ud}^*V_{cd}+V_{us}^*V_{cs}+V_{ub}^*V_{cb} &= 0 \\ V_{ud}^*V_{td}+V_{us}^*V_{ts}+V_{ub}^*V_{tb} &= 0 \\ V_{cd}^*V_{td}+V_{cs}^*V_{ts}+V_{cb}^*V_{tb} &= 0 \\ V_{ud}^*V_{us}+V_{cd}^*V_{cs}+V_{td}^*V_{ts} &= 0 \\ V_{ud}^*V_{ub}+V_{cd}^*V_{cb}+V_{td}^*V_{tb} &= 0 \\ V_{us}^*V_{ub}+V_{cs}^*V_{cb}+V_{ts}^*V_{tb} &= 0 \end{aligned} \tag{1.10}$$

In particular, we have

$$V_{ud}V_{ub}^*+V_{cd}V_{cb}^*+V_{td}V_{tb}^*=0 \tag{1.11}$$

Phenomenologically this relation is very interesting as it involves simultaneously the elements V_{ub}, V_{cb} and V_{td} which are under extensive discussion at present. The relation 1.11 can be represented as a unitarity triangle in the complex $(\bar{\rho}, \bar{\eta})$ plane. The

invariance of 1.11 under any phase-transformations implies that the corresponding triangle is rotated in the plane under such transformations. Since the angles and the sides (given by the moduli of the elements of the mixing matrix) in this triangle remain unchanged, they are phase convention independent and are physical observables. Consequently they can be measured directly in suitable experiments. One can construct five additional unitarity triangles corresponding to other orthogonality relations, like the one in 1.11. Some of them should be useful when the data on rare and CP violating decays improve.

The relation 1.11 can be represented as the triangle in the complex plane as shown in Figure 1.1, where

$$\begin{aligned} \vec{CA} &= \bar{\rho} + i\bar{\eta} = -\frac{V_{ud}V_{ub}^*}{V_{cd}V_{cb}^*} \\ \vec{AB} &= 1 - \bar{\rho} - i\bar{\eta} = -\frac{V_{td}V_{tb}^*}{V_{cd}V_{cb}^*} \\ \vec{CB} &= 1 \end{aligned} \tag{1.12}$$

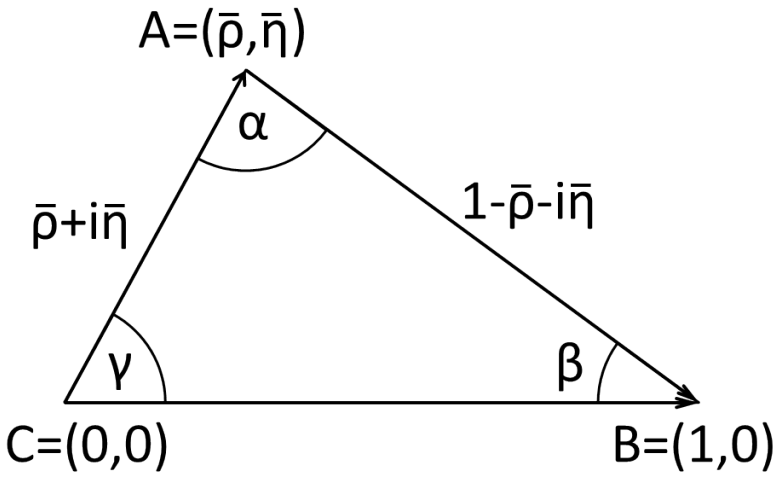

Figure 1.1: Unitarity Triangle.

The parameters $\bar{\rho}$ and $\bar{\eta}$ are the coordinates in the complex plane.

Phenomenological analyses of some processes can constrain the values of $\bar{\rho}$ and $\bar{\eta}$ of the Unitarity Triangles .

1.2 $K \to \pi\nu\bar{\nu}$ rare decays

The rare decays $K^+ \to \pi^+\nu\bar{\nu}$ and $K_L^0 \to \pi^0\nu\bar{\nu}$ are extremely attractive processes to study the physics of flavour because they both are exceptionally clean modes. These are FCNC processes and are not allowed in SM framework at tree level.

However they can proceed through second order graphs. The hard (quadratic) GIM mechanism is active; thus, these decays are dominated by short-distance dynamics, this is a crucial point, since QCD contribution can be calculated in perturbation theory. These decays are sensitive to a direct measurement of CKM element V_{td} that up to now has never been directly measured. Furthermore, they are extremely sensitive to possible new degrees of freedom beyond the Standard Model [17] [13]. At the quark level the two processes arise from the s→d$\nu\bar{\nu}$ process, which in the Standard Model originates from a combination of the Z_0 penguin and double W exchange graphs (see Figure 1.2).

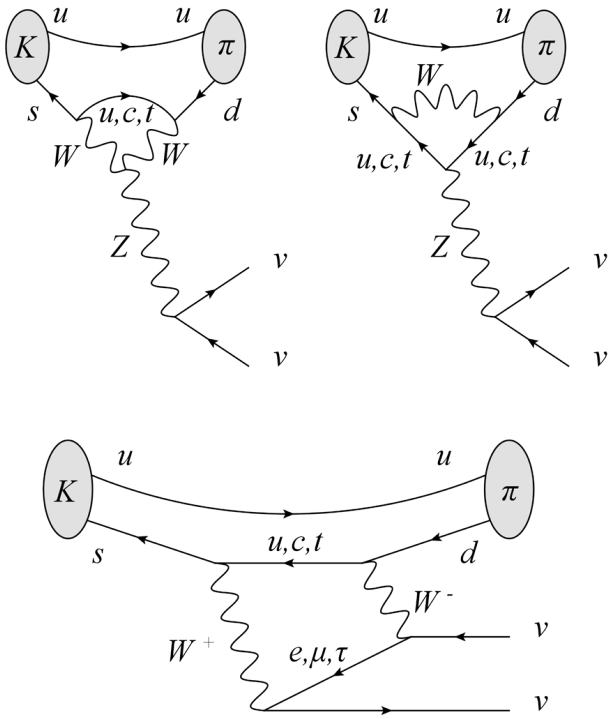

Figure 1.2: Diagrams contribution to $K \to \pi\nu\bar{\nu}$ branching fraction, on bottom double W exchange on top Z penguin.

1.2.1 B($K^+ \to \pi^+\nu\bar{\nu}$) and relative uncertainties

The branching ratio of $K^+ \to \pi^+\nu\bar{\nu}$ can be written as [16]:

$$B(K^+ \to \pi^+\nu\bar{\nu}) = \kappa \cdot \left[\left(\frac{Im\lambda_t}{\lambda^5} X(x_t) \right)^2 + \left(\frac{Re\lambda_c}{\lambda} P_0(K^+) + \frac{Re\lambda_t}{\lambda^5} X(x_t) \right)^2 \right] \tag{1.13}$$

$$\kappa = r_{K^+} \frac{3\alpha^2 B(K^+ \to \pi^0 e^+ \nu)}{2\pi^2 \sin^4 \Theta_W} \lambda^8 \tag{1.14}$$

$$X(x) = \eta_X \cdot \frac{x}{8}\left(\frac{x+2}{x-1} + \frac{3x-6}{(x-1)^2} ln\, x\right),\ \eta_X = 0.985 \tag{1.15}$$

$$P_0(K^+) = \frac{1}{\lambda^4}\left[\frac{2}{3}X^e_{NL} + \frac{1}{3}X^\tau_{NL}\right] \tag{1.16}$$

Here $x_t = \mathrm{m}_t^2/\mathrm{M}_W^2$ and $\lambda_i = \mathrm{V}_{is}\mathrm{V}_{id|}$ (i = u, c, t).

The parameter $\mathrm{r}_{K^+} = 0.901$ summarizes isospin breaking corrections in relating $K^+ \to \pi^+\nu\bar{\nu}$ to the well measured leading decay $K^+ \to \pi^0 e^+\nu$. In the standard parametrization λ_c is real to an accuracy of better than 10^{-3}.

The Function X represents the Next Leading Order correction, and finally $P_0(K^+)$ is the charm contribution. Relation 1.13 is very clean, and from it we can extract real and imaginary parts of λ_t (and so V_{td}). Moreover adding to λ_t the information from A (or V_{cb}) we have, finally, a constraint in $(\bar{\rho}, \bar{\eta})$ plane.

For what concerns the uncertainties that affect the theoretical estimation of $\mathrm{B}(K^+ \to \pi^+\nu\bar{\nu})$,could be summarize as follow:

- The contribution coming from Top quark is negligible because it is computed at high energy scale $\mathrm{O}(\mathrm{m}_t)$, and QCD perturbation calculation are a reliable tool. This is translated in an uncertainty of O(1%) for $X(x_t)$.

- For what concerns Charm contribution, perturbation theory cannot be expected as accurate as in top case. Still the reliability of the calculation can be much improved by performing a next-to-leading analysis. Also if NLO corrections are achieved the residual uncertainty on $P_0(K^+)$ is ∼10%

- Out of Top and Charm short distance contributions there are also a long distance contribution coming from up quark. This contribution is calculated using non-perturbative low energy QDC, but unfortunately this is not a reliable tool. However it is highly suppressed due to quadratic GIM mechanism. Long distance terms contribute for about ∼2% of charm amplitude and is likewise negligible.

- In order to eliminate the hadronic matrix element $< \pi|(\bar{s}d)_V|K >$, through equation 1.14 the $K^+ \to \pi^+\nu\bar{\nu}$ decay is related to $K^+ \to \pi^0 e^+\nu$ using isospin symmetry. The experimental accuracy on $\mathrm{B}(K^+ \to \pi^0 e^+\nu)$ is the main source of uncertainty and is about ∼1%.

With this in mind we can give the theoretical expectation value for $\mathrm{B}(K^+ \to \pi^+\nu\bar{\nu})$ [12]:

$$B(K^+ \to \pi^+\nu\bar{\nu}) = (8.51 \pm 0.73) \times 10^{-11} \tag{1.17}$$

1.2.2 $\mathrm{B}(K_L^0 \to \pi^0\nu\bar{\nu})$ and relative uncertainties

Due to the CP properties of K_L, π_0 and the relevant hadronic, short-distance transition current, the mode $K_L^0 \to \pi^0\nu\bar{\nu}$ proceeds in the SM almost entirely through

direct CP violation. In explicit terms the branching fraction per neutrino flavor is given by

$$B(K_L^0 \to \pi^0\nu\bar{\nu}) = \kappa_L \left(\frac{Im\lambda_t}{\lambda^5} X(x_t) \right)^2 \tag{1.18}$$

$$\kappa_L = r_{K_L} \frac{\tau_{K_L}}{\tau_{K_+}} \frac{3\alpha^2 B(K^+ \to \pi^0 e^+ \nu)}{2\pi^2 sin^4\Theta_W} \lambda^8 \tag{1.19}$$

These equations provide a very accurate relationship between the observable B($K_L^0 \to \pi^0\nu\bar{\nu}$) and fundamental SM parameters. The high precision that can be achieved in the theoretical calculation of this decay mode is rather unique among rare decay phenomena. This can be achieved because the main uncertainty, that affects the charged mode, is no longer present because $K_L^0 \to \pi^0\nu\bar{\nu}$ is a direct CP-violating process. A list of theoretical uncertainties is:

- The CP violating nature of neutral mode implies that only top contributes to branching fraction. This means that char is highly suppressed as the uncertainty that derives from it. After including NLO corrections the theoretical uncertainty on $X^2(x_t)$ is ~1%.
- The long distance contribution is still negligible as for $K^+ \to \pi^+\nu\bar{\nu}$.
- Hadronic matrix element is eliminated using the term B($K^+ \to \pi^0 e^+ \nu$)·τ_{K_L}/τ_{K_+}, the experimental error is about 1.5%.

The theoretical value [12] for B($K_L^0 \to \pi^0\nu\bar{\nu}$) is $(2.54 \pm 0.35)\times10^{-11}$.

1.2.3 Experimental status

The E787 and E949 experiments have established the feasibility of observing the decay $K^+ \to \pi^+\nu\bar{\nu}$ using a stopped Kaon beam [5]. Observation of seven candidate events by E787 and E949 yields B($K^+ \to \pi^+\nu\bar{\nu}$) = $1.73^{+1.15}_{-1.05} \times 10^{-10}$.

The experiment E391a has set a limit of B($K_L^0 \to \pi^0\nu\bar{\nu}$)<$670\times10^{-10}$ at 90% CL analyzing a sample of 5.9×10^9 K_L decays [7]. E391a is currently analyzing an additional 3.6×10^9 K_L decays and plans to implement an upgraded detector in the experiment E14 at JPARC that would have a sensitivity comparable to the expected SM $K_L^0 \to \pi^0\nu\bar{\nu}$ decay rate.

1.2.4 Sensitivity to New Physics

Rare K decays are ideally suited to search for New Physics (NP) effects. Indeed, besides the loop suppression of the underlying FCNC processes, they are significantly CKM suppressed. Compared to B sector, the amplitudes in the s→d sector scale as

$$A(s \to d) \sim |V_{td}^* V_{ts}| \sim \lambda^5, A(b \to d) \sim |V_{td}^* V_{tb}| \sim \lambda^3, A(b \to s) \sim |V_{ts}^* V_{tb}| \sim \lambda^2, \tag{1.20}$$

with λ ~0.22. If NP is generic, i.e., it does not follow the CKM scaling, it is clear that the constraints from rare K decays are typically the most stringent. Stated

differently, a measurement of $K_L^0 \to \pi^0\nu\bar{\nu}$ close to its SM prediction is the most difficult to reconcile with the existence of generic NP at a reasonably low scale around a TeV. NP models in which the CKM scalings are preserved are referred to as of MFV type [22].

Each NP model affects the basic electroweak FCNC differently. If it enters into the Z penguin, the two $K \to \pi\nu\bar{\nu}$ modes exhibit the best sensitivity. This happens for example in the Minimal Supersymmetric Standard Model extension. Combined measurements of all the rare K decay modes can serve as a powerful discriminator among models. A very fashionable picture is reported in Figure 1.3, where is reported the value of two branching ratios computed in different theories beyond SM.

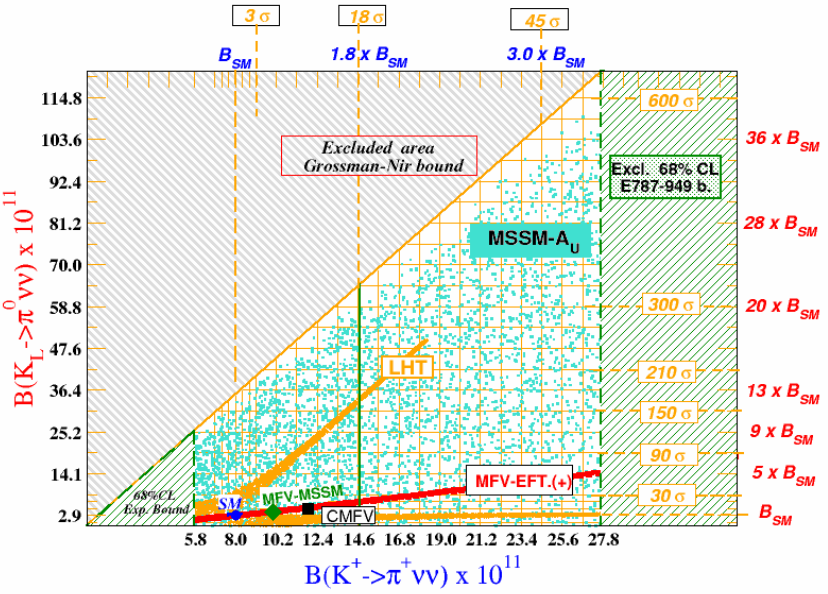

Figure 1.3: $K \to \pi\nu\bar{\nu}$ decays branching factions predicted in different theories beyond SM.

1.3 R_K in Standard Model and beyond

The R_K ratio in SM framework is a very well determined quantity [18]:

$$R_K^{SM} = \frac{m_e^2}{m_\mu^2} \cdot \frac{m_k^2 - m_e^2}{m_k^2 - m_\mu^2} \cdot (1 + \delta R_K^{Rad.Corr.}) = (2.477 \pm 0.001) \times 10^{-5} \qquad (1.21)$$

where $\delta R_K^{Rad.Corr.} = (3.79 \pm 0.04)\%$ is an electromagnetic correction due to the IB and structure dependent effects. Any significant deviation from this value could signal new physics. In Minimal Supersymmetric Standard Model (MSSM) scenario

R_K value is modified due to Lepton Flavor Violating (LFV) terms in charged Higgs exchange diagrams (Figure 1.4). Using reasonable SUSY parameters values (the mixing parameter between the superpartners of the right-handed leptons, $\Delta_{13} = 5 \times 10^{-4}$, the ratio of the two Higgs vacuum expectation values, $\tan(\beta)$, and the Higgs mass,$m_H = 500$ GeV) sizable deviations from SM value have been predicted [31]:

$$R_K^{LFV} = 2\frac{\Gamma_{SM}(K \to e\nu_e) + \Gamma_{LFV}(K \to e\nu_\tau)}{\Gamma(K \to \mu\nu_\mu)} = R_K^{SM}(1 + 0.013) \tag{1.22}$$

1.3.1 Experimental Status

R_K PDG08 value is computed using three measurements dating back to the 70s:

$$R_K^{70s} = (2.45 \pm 0.11) \times 10^{-5} \tag{1.23}$$

A recent new result from KLOE [25] experiment improved the measurement:

$$R_K^{KLOE} = (2.493 \pm 0.031) \times 10^{-5}. \tag{1.24}$$

The new world average is

$$R_K^{2009} = (2.468 \pm 0.025) \times 10^{-5} \tag{1.25}$$

with a precision of 1%.

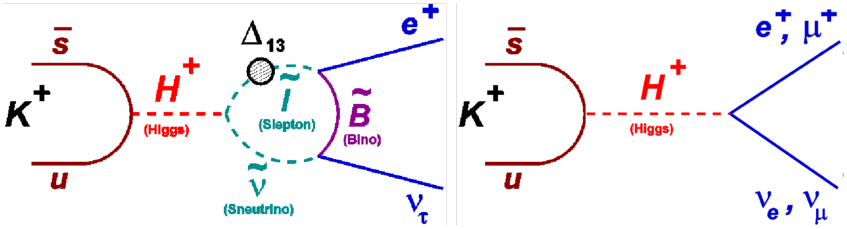

Figure 1.4: SUSY contributions to $BR(K \to l\nu_l)$.

1.4 NA62 Phase I

NA62 phase I took place in 2007 when we collected data in order to measure the ratio $R_K = K_{e2}/K_{\mu 2}$ (were $K_l 2$ means $K \to l\nu_l(\gamma)_{IB}$) at few per mill level. The photon due to internal bremsstrahlung (IB) is taken into account in the Monte Carlo simulation and in data analysis. A brief experimental layout description will be followed by analysis strategy and preliminary results [40].

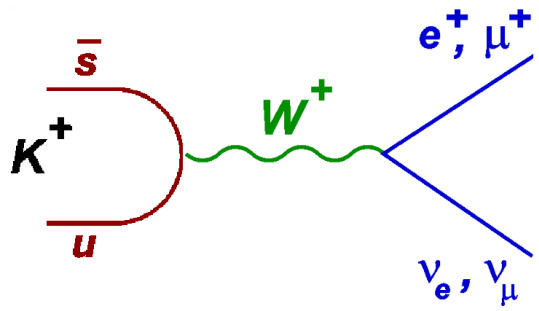

Figure 1.5: SM contributions to $BR(K \to l\nu_l)$.

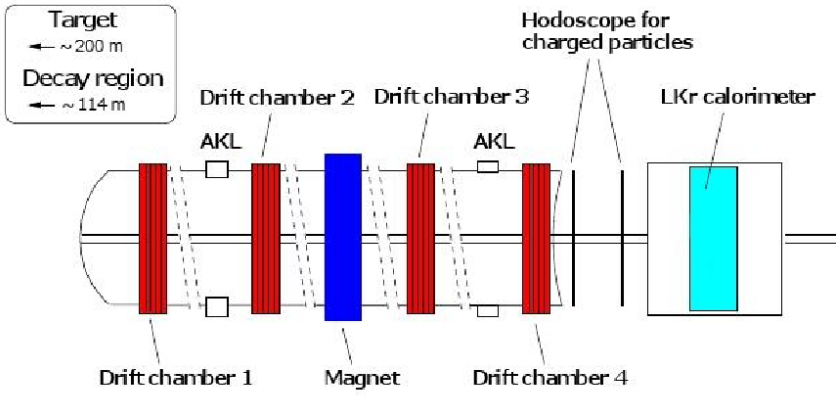

Figure 1.6: Scheme of apparatus for R_K measurement.

1.4.1 Apparatus, Trigger Logic and Measurement Strategy

Data have been taken in the June-October 2007 period. The apparatus used is reported in Figure 1.6.

It is composed by a charged Hodoscope (called HODO) used as fast trigger, a Drift CHamber (DCH) spectrometer, a photon veto (called AKL) and the NA48 Liquid Kripton (LKr) calorimeter.

We used a minimum bias hardware trigger in order to select simultaneously K_{e2} and $K_{\mu 2}$ events to minimize the systematics. The two samples only differ for energy release in LKr. Common logical conditions used are: activities in DCHs and energy release into both the hodoscope planes. K_{e2} events have to satisfy a further condition on energy released in LKr (higher than 10 GeV). The $K_{\mu 2}$ trigger is downscaled by a factor D=150. Data taking goal was to collect about 150K events of K_{e2} in order to have an accuracy better than 0.5%.

The experimental quantity to be measured is:

$$R = \frac{1}{D} \cdot \frac{N_{Ke2} - N_{Ke2}(BG)}{N_{K\mu 2} - N_{K\mu 2}(BG)} \cdot \frac{A_{K\mu 2} \times \varepsilon_{K\mu 2} \times PID_{K\mu 2}}{A_{Ke2} \times \varepsilon_{Ke2} \times PID_{Ke2}} \tag{1.26}$$

where N_{Kl2} (l=e,μ) is the number of selected events, $N_{Kl2}(BG)$ is the number of background (BG) events, A_{Kl2} the geometrical acceptance, ε_{Kl2} and PID_{Kl2} the trigger and selection efficiencies respectively. The ratio R has been evaluated in 10 momentum bins, between 13 to 65 GeV.

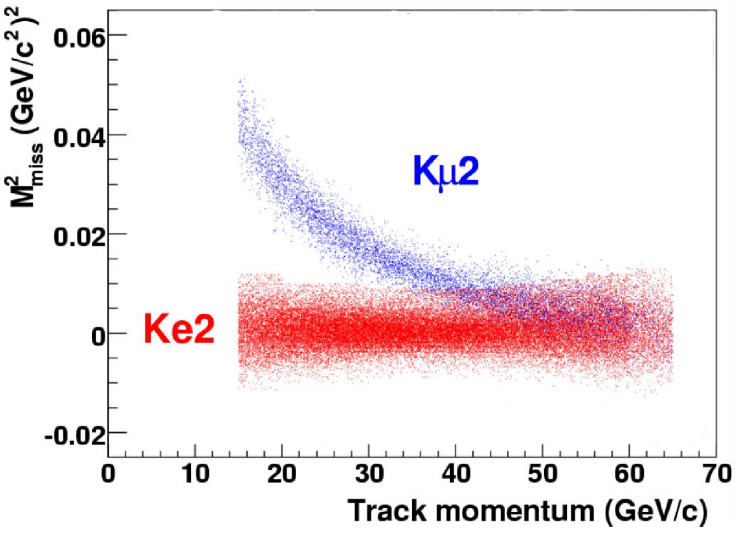

Figure 1.7: M^2_{miss} vs track momentum in electron mass hypothesis.

1.4.2 Signal Selection and Main Background

In order to separate the two samples we exploited the kinematic separation (using $M^2_{miss} = (p_K - p_l)^2$ see Figure 1.7) which is optimal for tracks with energy up to 25

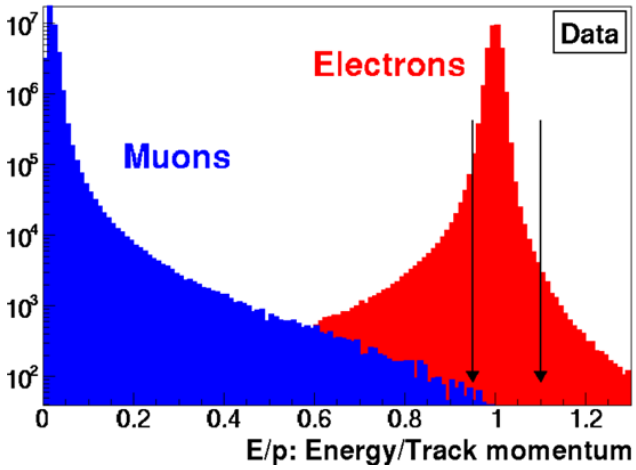

Figure 1.8: E/P distribution, the arrows define the signal cuts.

GeV and particle identification using E/p ratio (energy released in LKr/measured track momentum see Figure 1.8). The selection criteria are:

- electon: 0.95≤ E/P≤ 1.1;
- muon: E/P≤ 0.85.

The number of K_{e2} candidates in the signal region is N(K_{e2}) = 59964. The main background source for K_{e2} sample are $K_{\mu 2}$ events in which the muon loose all its energy into LKr (catastrophic bremsstrahlung) thus emulating an electron (therefore K_{e2} event). These events ere expected to contribute at O(10%) level to the final sample and we thus decided to directly measure their fraction in order to validate Monte Carlo estimates. This measurement has been done using a pure (electron contamination was evaluated to be $\sim 10^{-7}$) muon sample obtained interposing a $10X_0$ deep lead wall between the two hodoscope planes. A MC simulation was made with and without the lead wall, the first was compared with data finding a very good agreement. The second was used to evaluate the real background contamination: (6.10 ± 0.22)%, see Figure 1.9.

The number of $K_{\mu 2}$ candidate collected with a trigger chain involving downscaling by a factor of 150 is N($K\mu 2$) = 1803[7]. The main background source for $K_{\mu 2}$ sample is due to the beam halo muons. This effect has been measured directly by reconstructing the $K^+_{\mu 2}$ from a K^- data sample collected with the K+ beam (but not its halo) blocked, and a special data sample collected with both beams blocked. The real background contamination: (0.38 ± 0.01)%

1.4.3 Preliminary result

A preliminary result of R_K measurement computed on 40% of whole collected statistics is:

$$R_K = (2.486 \pm 0.011_{stat} \pm 0.007_{syst}) \times 10^{-5} =$$
$$(2.486 \pm 0.013) \times 10^{-5} \tag{1.27}$$

the precision reached is 0.52%, see Figure 1.10. This result has been obtained using only the 40% of the data set. With the whole sample we expect to reach $\sim 0.3\%$.

The main source of systematic uncertainty is due to the evaluation of the $K_{\mu 2}$

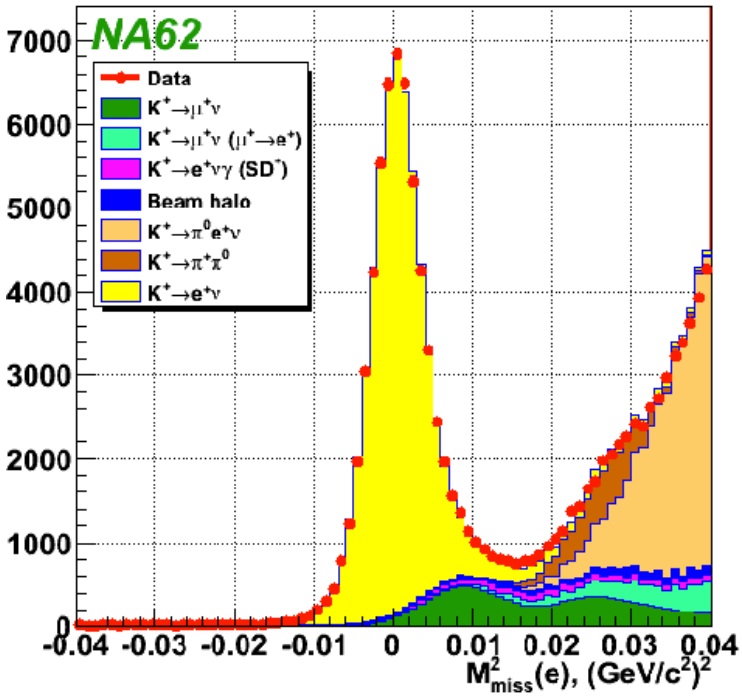

Figure 1.9: M^2_{miss} distribution in electron mass hypothesis.

background in the K_{e2} sample $\delta R_K \times 10^5 = 0.005$.

1.4.4 Future prospective

In the framework of NA62, phase II, the uncertainties on the measurement of R_K can be reduced, both the statistical one and the systematic one. During the first year of data taking more that 1200k K_{e2} candidates will be collected while the use of RICH for the electon-muon discrimination will reduce contamination to negligible level. The expected total uncertainty is below the 0.2%.

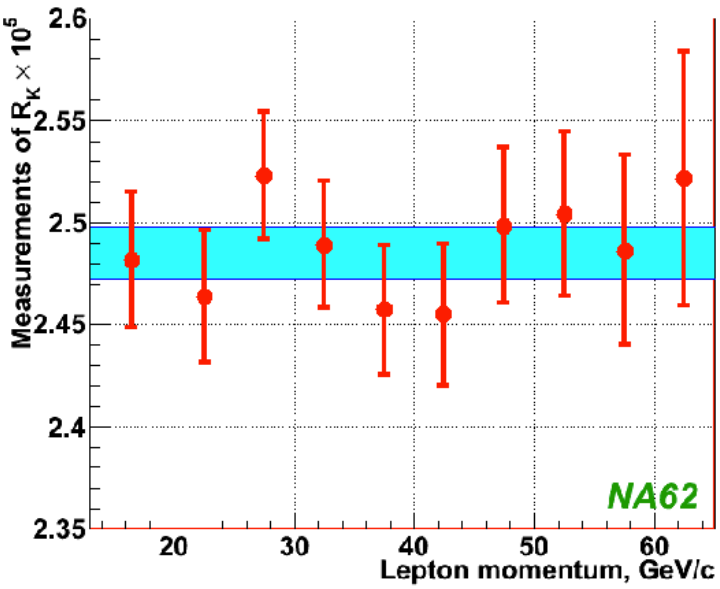

Figure 1.10: R_k evaluation for different track momentum bins.

Chapter 2

The NA62 experiment

The NA62 experiment aims to measure the Branching Ratio of $K^+ \to \pi^+ \nu\bar{\nu}$ decay with signal/background ratio of about 10. It is a fixed target experiment and is located at K12 beam line at CERN North experimental Area. An SPS extracted 400 GeV/c proton beam is the primary beam, a 40 cm long beryllium target is used to generate an unseparated 75 GeV/c positive hadrons secondary beam.

NA62 aims to collect $\sim$100 $K^+ \to \nu\bar{\nu}$ events in about two years of data taking and to keep the total systematic uncertainty small. To this purpose, at least 10^{13} K^+ decays are required, assuming a 10% signal acceptance. To keep the systematic uncertainty small requires a rejection factor for generic kaon decays of the order of 10^{12}, and the possibility to measure efficiencies and background suppression factors directly from data. Kaon intensity, signal acceptance and background suppression are, therefore, the driving criteria for the construction of the NA62 experiment [9].

In further discussion a common frame of reference is considered: Z axis is longitudinal experimental axis, X axis is the horizontal axis and Y axis is the vertical one.

2.1 General strategy

The NA62 experiment will be housed in the CERN North Area High Intensity Facility (NAHIF), where CERN-SPS extraction line, already used for the NA48 experiments, can deliver the required intensity. Protons from the SPS at 400 GeV/c impinge on a beryllium target and produce a secondary charged beam. Considerations about signal acceptance drive the choice of a secondary positive beam of 75 GeV/c with 1% momentum bite and a divergence below 100 μrad, both in the x and y projections. Only $\sim$6% of secondary particles are K^+, the others π^+ and protons. The beam has a square shape of 60×27 mm^2 area and a total flux rate of about 800 MHz at the end of the beam line. The high momentum of the secondary beam improves background rejection and sets the longitudinal scale of the experiment. The main elements for the detection of the K^+ decay products are spread along a 170 m long region starting about $\sim$100 m downstream of the beryllium target. Useful K^+ decays will be detected from a 65 m long fiducial region. The largest detectors have an approximately cylindrical shape around the beam axis. Inner diameter varies from 12 to 220 cm, in order to avoid any interaction with very intense flux of main beam. The decay region is in vacuum, this in order to suppress backgrounds due to interaction between beam particles and residual gas. Vacuum is provided by a $\sim$120 m long tank (called Blue Tube). The overall rate integrated over these detectors is

in the range of 10 MHz. A schematic layout of the experiment is shown in Figure 2.1.

To achieve the required background suppression, different techniques have to be employed in combination. This allows one to measure the rejection factors from the data by inverting the cuts one at the time.

Since the neutrino-antineutrino pair is undetectable, the signature of the signal consists of a single π^+ track reconstructed downstream of the decay volume and matched to a K^+ track upstream. Timing, spatial and angular information are needed to match these two tracks. Generic K^+ decay modes can mimic a signal when just a single track is detected and the other particles escape detection. Beam particles interacting in the last station of the beam tracking detector or in the residual gas can also contribute to backgrounds if they are accidentally matched to an incoming undecayed kaon track.

The experiment, therefore, needs tracking devices for both K^+ and π^+, and also calorimeters in order to veto photons, positrons and muons. In addition, particle identification systems to identify the incident kaons and to distinguish π^+ from μ^+ and e^+ must complement the tracking and veto detectors to reach the ultimate sensitivity and to guarantee redundancy. The guiding principles for the construction of the NA62 detectors are, therefore: accurate kinematic reconstruction, precise particle timing, efficiency of the vetoes and excellent particle identification.

2.1.1 Tracking system

The most discriminating variable to distinguish the $K^+ \to \pi^+\nu\bar{\nu}$ signal from background is the squared missing mass: $m^2_{miss} = (P_K - P_\pi)^2$. Here P_K denotes the 4-momentum of the parent particle assumed to be a kaon and P_π is the 4-momentum of the decay particle assumed to be a π^+. This variable rejects more than 90% of K^+ decays, as shown in Figure 2.2. There are two signal regions, one on each side of the $K^+ \to \pi^+\nu\bar{\nu}$ peak. One can define Region I (Region II), the signal region, in which m^2_{miss} is lower (larger) than $m^2_{\pi^0}$. Backgrounds from kaon decays ($K^+ \to \pi^+\pi^0$, $K^+ \to \mu^+\nu$ and $K^+ \to \pi^+\pi^+\pi^-$, see Figure 2.2) can enter these signal regions because of kinematic resolution effects or because of the lack of a well defined kinematical constraint (e.g. kaon semi-leptonic decays as shown in bottom of Figure 2.2).

For kinematical events suppression we need the best resolution on m^2_{miss}. As a consequence the tracking requires low mass and high-precision detectors. Simulations have shown that an overall material budget of ~2% radiation length, together with an intrinsic resolution on the track position of about 100 μm and a momentum resolution below 0.5%, correspond to a resolution on m^2_{miss} below 10^{-3} GeV^2/c^4.

The tracking system consists of a kaon and a pion spectrometer. They are made of thin detectors orthogonal to the beam axis, with one or more magnets in between for momentum analysis. The different transverse size for the upstream and downstream detectors, together with the required performances, determines the technology choice. The beam spectrometer, called Gigatracker (GTK), consists of

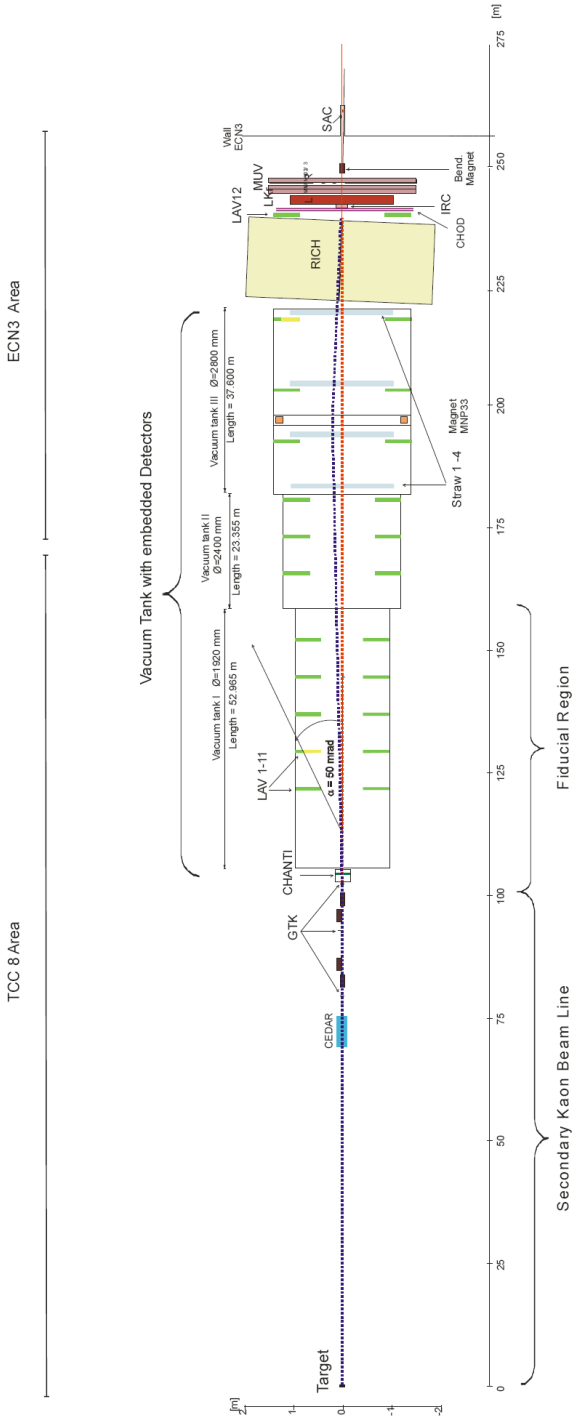

Figure 2.1: NA62 apparatus overview.

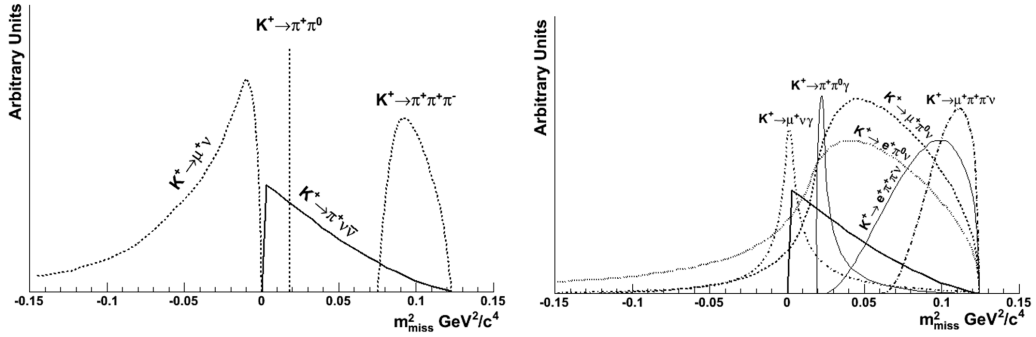

Figure 2.2: On left side constrains on kinematics, on right side not kinematically constrained decays.

three solid state micro-pixel stations matching the beam dimensions. These stations are placed in vacuum. The GTK is crossed by the full beam intensity (about 800 MHz) and must provide a time resolution of better than 200 ps in order to avoid the wrong association of a beam particle to the decay reconstructed in the downstream detectors. A wrong association might lead to the wrong calculation of the missing mass which in turn would decrease the kinematical discrimination against, most notably, the $K^+ \to \pi^+\pi^0$ decays. Four dipole magnets provide an achromatic (no net bending) spectrometer for particles of any momentum. The GTK provides a 0.2% RMS momentum resolution and an angular resolution of $\sim$15 μrad on an event-by-event basis. A pion spectrometer consisting of four straw tube chambers (STRAW) operated directly in the vacuum tank. The first chamber is placed about 80 m downstream of the last station of the GTK. The choice to operate the STRAW chambers in vacuum minimizes the multiple scattering by avoiding the use of a window to separate the decay from the tracking volume and the helium which would be otherwise required in between the chambers to operate them near atmospheric pressure. A careful technological choice for the straws can reduce the material budget down to 0.5% radiation length per chamber. The same magnet employed in the NA48 experiment will be used: it is located after the second STRAW chamber and provides a 256 MeV/c momentum kick in the horizontal (x-z) plane. This bending provides a sufficient pion momentum resolution. A region free of tubes, 12 cm wide, in the middle of the chambers forms a passage where the beam passes through undisturbed. The x-position of the beam hole in the chambers follows the 75 GeV/c beam path. The spatial matching between the K^+ track, extrapolated into the decay region, and the pion track, extrapolated backward, largely protects against a mis-measurement of the pion direction due to a possible large angle scattering in the first chamber.

The tracking systems are also crucial against a more subtle, but equally important source of background. Beam hadronic interactions in the last station of the GTK material may cause the emission of a leading π^+ which enters the pion

acceptance, while the associated multiplicity of soft particles can escape from the detector. A suitable cut on the reconstructed vertex position is crucial for the suppression of this accidental background. The limitation comes from a possible large scattering of the pion in the first plane of the straw spectrometer, which creates non-Gaussian tails and might shift the reconstructed vertex in the decay region.

2.1.2 Timing

The need to match the incoming K^+ and the π^+, and the high rate of particles (800 MHz) crossing the GTK detector set the timing performance of the experiment. Without precise timing, an accidental beam particle can be mistaken for the decaying kaon and be associated to the π^+. This association can spoil the kinematic resolution because the beam divergence is non-negligible. As a consequence, the kinematic rejection of the two body decays is weakened and more background enters the signal regions. With a 100 ps time resolution on the π^+ track and 150 ps time resolution for the beam tracks, the fraction of events with a wrong association can be kept to below 1% once appropriate spatial cuts (e.g. cuts based on the closest distance of approach between the pion and kaon track candidates) are applied. Precise timing for the π^+ is provided by the RICH counter. As mentioned, the timing of K^+ requires a fast detector exposed to the full beam intensity (GTK).

2.1.3 Veto system

The kinematic rejection alone cannot provide the requested level of background suppression. An additional factor must come from vetoing photons and muons. The suppression of possible background from $K^+ \to \pi^+\pi^0$ decays determines the design of the photon veto system. One requires an overall inefficiency of about 10^{-8} for the π^0 detection. It is crucial that the veto system covers an acceptance from 0 to 50 mrad from the K^+ decay vertex with respect to the beam line. The NA62 design insists on the very high detection efficiency for high energy photons rather than attempting to capture photons of small energy going sideways. The reason for this approach is that in order to consistently detect photons at angles larger than 50 mrad one would need to install photon detectors along the entire length of the vacuum tank without gaps, which would be a massive construction task. In addition, photons from kaon decays with angles in the laboratory larger than 50 mrad are characterized by low energies that would make their detection difficult and dependent on low energy thresholds.

The photon veto detectors are: a system of 12 Large Angle Veto (LAV) calorimeters covering an angle interval from 8.5 to 50 mrad, an electromagnetic calorimeter for the detection of photons between 1 and 8.5 mrad (LKR), and small angle calorimeters covering the region below 1 mrad (Intermediate Ring Calorimeter and Small Angle Calorimeter). In the analysis, the π^+ momentum will be required to be less than 35 GeV/c. In this way, the momentum of the π^0 amounts to at least 40 GeV/c. Such a large energy deposit can hardly be missed in the calorimeters.

The photon detection inefficiency has to be below 10^{-5} for photons in the 1-10 mrad region above 10 GeV, and less than 10^{-3} for photons above 1 GeV. These inefficiency requirements are a consequence of the angle-energy correlation of the photons from π^0 decays.

We reuse the liquid Krypton (LKR) electromagnetic calorimeter of NA48 [44] as a veto for photons in the 1-10 mrad region.

Measurements based on NA48 data have demonstrated the capability of the LKR to reach the required veto performance. Since the LKR is equipped with a beam-pipe to accommodate the passage of the charged beam, an additional photon detector must cover the small angle region. For this reason, a rectangular calorimeter (SAC), built with "Shashlik" technology, is located at the end of the beam line just after a sweeping magnet that deflects the high intensity charged beam. The SAC inefficiency should be less than 10^{-5}, which is not a problem given the high energy of the photons in this region. An Intermediate Ring Calorimeter (IRC), located just in front of the LKR, complements the acceptance for photon detection in the interface region between the coverage of the SAC and the LKR.

The 12 LAV calorimeters are operated (with the exception of the last one) in the vacuum tank. The positions of the LAVs along the experiment are chosen to satisfy the required angular coverage. This configuration is the best compromise between acceptance and detector complexity, driven by the whole geometry of the experiment and the high energy of the beam.

Since the largest fraction of K^+ decays contains muons in the final state, a muon veto system is mandatory both on-line and off-line. Because of the high rates, a muon veto in the earliest stage of the trigger is crucial to reduce the data rate below 1 MHz, the maximum rate that can be handled by the readout system. Further muon suppression is required off-line. The muon veto system (MUon Veto system, MUV) consists of two iron-scintillator hadronic calorimeter (MUV1 and MUV2). These detectors are located after the LKR. An iron wall separates this calorimeter from a plane of fast scintillators (MUV3) which provides both the trigger information and additional power in vetoing muons. Monte Carlo simulations predict an overall inefficiency for muon detection of about 10^{-5}, achievable by exploiting the electromagnetic and hadronic shower separation capability of the hadronic and LKR calorimeters together. Further muon rejection is provided by the Ring Imaging Cherenkov counter (RICH) described in the next section. Finally a veto for charged particles placed just downstream of the last GTK station, provides additional rejection of the accidental background coming from hadronic interactions of the beam particles in the last GTK station, as previously discussed. This detector, called CHANTI, consists of scintillators assembled in a rectangular shape surrounding the beam.

2.1.4 Particle Identification

To provide an additional 10^2 suppression of backgrounds originating from the $K^+ \to \mu^+\nu(\gamma)$ decays, a Ring Imaging Cherenkov (RICH) detector is used. The 17 m long

RICH is filled with Ne at atmospheric pressure. It is placed after the last straw chamber and equipped with 2000 PMTs. Results based on a full length prototype [30] indicate that, for π^+/μ^+ separation, a mis-identification probability smaller than 1% can be achieved in the relevant momentum range. A 17 cm diameter beam tube passes through the whole RICH volume to avoid the interaction of the beam with the Ne gas. The RICH also distinguishes positrons from π^+, allowing the suppression of backgrounds with positrons in the final state, such as $K^+ \to \pi^0 e^+ \nu$, or channels with a π^0 Dalitz decay ($\pi^0 \to \gamma e^+ e^-$). The pion Cherenkov threshold of the Ne is around 13 GeV/c. Therefore, to insure full efficiency, a cut on the minimum π^+ momentum of about 15 GeV/c is required. The RICH has also remarkable timing properties: its time resolution, which is better than 100 ps, makes this detector ideal to measure the arrival time of the π^+ and to match it to the parent particle measured by the GTK. Thanks to the long lever arm between the STRAW chambers which follow the spectrometer magnet, the RICH is also able to provide full acceptance for high momentum tracks from kaon decays with more than one charged particle. Finally, the RICH can also provide a cross-check to the π^+ momentum measured by the straw spectrometer when the particle is assumed to be a pion. Although the RICH momentum resolution is a factor of four poorer than the one obtained from the magnetic spectrometer, this redundant measurement is useful to reject events in the tails in the m^2_{miss}. The material of the RICH may complicate the detection of photons because of conversions or photo nuclear interactions. To mitigate this inefficiency, a charged hodoscope (CHOD) placed downstream of the RICH and before the LKR is envisaged. Simulations showed that the RICH itself, the CHOD, the IRC and the last ring of the LAV together, keep this source of inefficiency at a negligible level.

The LKR is a powerful particle identifier, not only for muons, as stated before, but also for positrons and electrons, as demonstrated by the past experience of NA48. It is, therefore, a viable option to complement the RICH in the suppression of final states with $e^{\pm}$.

In NA62 the positive identification of the K^+ is also important because about 93% of the beam particles are π^+ or protons. They can interact in the residual gas contained in the vacuum tank and produce a signature that can mimic the signal. These backgrounds cannot be rejected simply applying a cut on the reconstructed longitudinal vertex position because they can occur anywhere in the fiducial volume. The K^+ identification is achieved by a Cerenkov differential detector, (CEDAR) operated to be blind to all particles but kaons of appropriate momentum. It is located upstream of the GTK. With a CEDAR time resolution of about 100 ps, the residual gas pressure in the decay region should not exceed 10^{-6} mbar. The CEDAR will also improve the rejection of candidates originating from pion and proton interactions on the last GTK station and can also serve to further improve the time association between the K^+ and the π^+ tracks.

2.1.5 Summary of Detectors Layout

For simplicity, a short summary of the NA62 layout is summarized here. A secondary kaon beam line, ∼100 m long, leads to a ∼65 m long fiducial region, followed by a further length, over which the kaon decay products fly apart with respect to the beam line, so that they can be recorded in a series of detectors surrounding the beam. The following detectors and features are incorporated in the NA62 layout (see Figure 2.1):

1. The CEDAR identifies the K^+ component in the beam with respect to the other beam particles by employing an upgraded differential Cerenkov (CEDAR) counter.

2. The Gigatracker (GTK) is composed of three Silicon micro-pixel stations measuring, time, direction and momentum of the beam particles before entering the decay region.

3. The STRAW chamber measures the coordinates and momentum of secondary charged particles originating from the decay region. To minimize multiple scattering the Chambers are built of ultra-light material and are installed inside the vacuum tank. The four Straw Chambers are intercepted in the middle by a large aperture dipole magnet (MNP33), providing a vertical B-field of 0.36 T.

4. The RICH detector is situated downstream of the last Straw chamber. It consists of a 17 m long radiator filled with Neon Gas at 1 atm allowing the separation of pions and muons between 15 and 35 GeV/c.

5. Photon-Veto detectors provide hermetic coverage from zero out to large (∼50 mrad) angles from the decay region. This is assured by:

   - the, existing, high-resolution Liquid Krypton electro-magnetic calorimeter (LKR),
   - supplemented, at small and forward angles, by an Intermediate Ring (IRC) and Small-Angle (SAC) Calorimeters and,
   - at large angles, by a series of 12 annular photon-veto (LAV) detectors (LAV).

6. The MUon-Veto Detectors (MUV) are composed of a two-part hadron calorimeter followed by additional iron and a transversally-segmented hodoscope. This system supplements and provides redundancy with respect to the RICH in the detection and rejection of muons.

7. These detectors are complemented by guard-ring counters (called CHANTI, CHarged ANTIcounter) surrounding the last GTK station, and the charged-particle hodoscope (CHOD), covering the acceptance and located between the RICH and the LKR calorimeter.

8. All these detector are operated and inter-connected with a high-performance trigger and data-acquisition (TDAQ) system.

2.2 Beam Line

The secondary hadron beam, called K12HIKA+, is designed to be derived from a high, but attainable, flux of 400 GeV/c protons in the underground North Area High Intensity Facility. The target/beam tunnel and the cavern (ECN3) where the detectors of experiment NA48 have been installed, have a combined length of 270 m. The primary protons, are focused and directed at zero angle onto a 400 mm long, 2 mm diameter beryllium target (T10). This is suspended between thin aluminium foils and is cooled by forced convection of air in the T10 target station. The target is followed by a 950 mm long, water-cooled, copper collimator, offering a choice of bores of different apertures. The largest, 15 mm in diameter, is generally selected to transmit the wanted secondary particles as well as the remaining primary proton beam.

The decay fiducial region is contained in the first 60 m of a large, ∼117 m long, evacuated tank (that begins at ∼100 m from target), which is closed off by a thin (∼0.045 X_0) aluminium window, separating it from the neon gas of the following RICH counter. This window is off-set horizontally and its centre is traversed by a thin-walled aluminium beam tube (of inside diameter 155 mm), which follows the trajectory of the beam, which is thus transported in vacuum through the downstream detectors (Figure 2.3).

The beam is then deflected to the side through a further angle of -13.6 mrad by a 2 m long, 200 mm gap, tapered-pole magnet (MBPL-TP) to reach a point ∼12 m further downstream, where it clears a small-angle, photon-veto calorimeter (SAC). This is inserted by ∼6 m on rails into the beam vacuum tube, of 600 mm inner diameter. This tube is itself installed in a larger (800 mm diameter) tube, which extends ∼10 m into the ground beyond the end of the cavern, ECN3. The beam is finally absorbed in a beam dump composed of iron surrounded by concrete at the downstream end of this tube, at a distance behind the detector, which allows space to shield against back-splash.

2.3 CEDAR

The disadvantage of high energy protons used by NA62 and, consequently, of a high energy secondary beam, is that the kaons cannot be efficiently separated from pions and protons at the beam level. The consequence is that the upstream detectors which measure the momentum and the direction of the kaons are exposed to a particle flux about 17 times larger than the useful (kaon) one. A critical aspect is therefore to positively identify the minority particles of interest, kaons, in a high rate environment before their decay. This will be achieved by placing in the incoming beam a differential Cerenkov counter, CEDAR, filled with hydrogen gas (to reduce

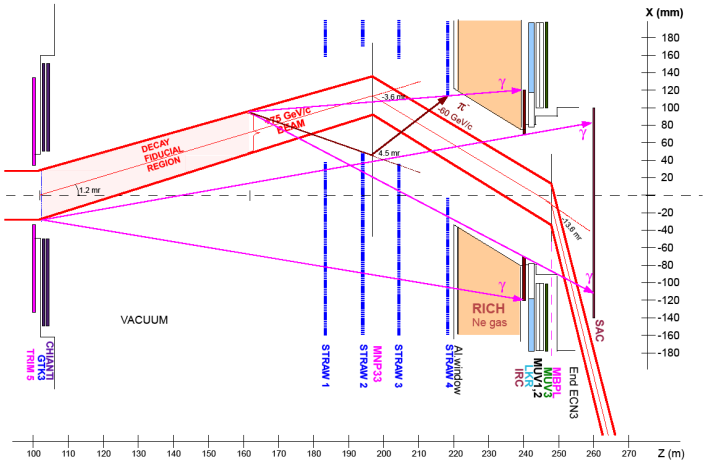

Figure 2.3: Schematic layout of the downstream part of the beam. Shown is the angular deviation of the charged kaon beam and the 1σ width of the beam profile.

beam multiple scattering).

A FLUKA simulation was used to study the interactions of pions, kaons and protons with the residual gas in the vacuum decay tank and the probability that such an interaction can cause fake triggers was computed. The conclusion is that (in the absence of kaon tagging) the vacuum should be better than 6×10^{-8} mbar to keep the background to less than one fake event per year. This very challenging requirement can be relaxed by at least an order of magnitude by positively tagging the kaons by means of a CEDAR Cerenkov counter in the beam line, filled with hydrogen gas at an absolute pressure just below 4 bar. A necessary part of this kaon identification is the precise timing of the different components in order to guarantee a good rejection of the background due to the accidental overlap of events in the detector. An upgraded form of the CEDAR built for the SPS secondary beams (CERN Report CERN-82-13) will be used, and will be insensitive to pions and protons with minimal accidental mis-tagging. The choice of the Hydrogen gas is dictated by the need to minimize material on the beam line, and hence reduce multiple Coulomb scattering. The window thickness will be of the order of 150+200 μm, and it is being evaluated.

The CERN CEDAR counter (see Figure 2.4) has been designed to identify particles of a specific mass by making the detector blind to the Cerenkov light produced by particles of different mass. For a given beam momentum, the Cerenkov angle of the light emitted by a particle traversing a gas of a given pressure is a unique function of the mass of the particle and the wavelength of the emitted light. The Cerenkov light emitted by particles of different mass is then not transported by the CEDAR optics through the diaphragm slit onto the light detectors but absorbed on its way. The rate from the kaon component in the high-intensity beam for NA62 is

50 MHz. The CEDAR detector is required to achieve a kaon tagging efficiency of at least 95%, with a time resolution of 100 ps. CEDAR optics produce 8 light spots of eight 30×8 mm^2 rectangular areas (see Figure 2.5). Photodetectors installed on CEDAR are Hamamatsu R7400U-03. The photon rate must be limit at 3 kHz/mm^2 (∼50 MHz per PM) in order to avoid system paralysis.

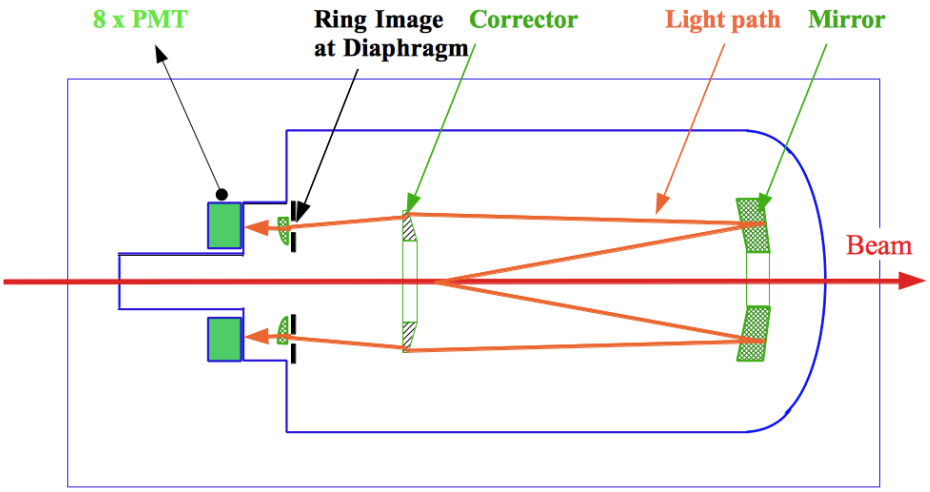

Figure 2.4: CEDAR conceptual scheme layout.

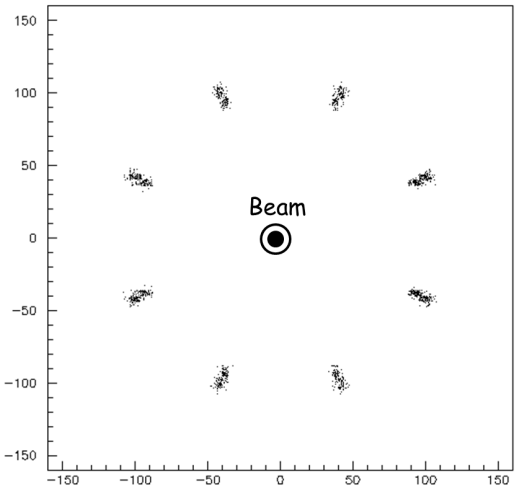

Figure 2.5: Light spots produced by CEDAR optics.

2.4 Gigatracker

The Gigatracker is composed of three stations (GTK1, GTK2 and GTK3) mounted between four achromat magnets as shown in Figure 2.6. This setup is placed along the beam line inside the vacuum tank, just before the fiducial region in the decay vacuum pipe. It has to sustain a high and non-uniform beam rate and has to survive in high radiation environment.

The overall simulation of the kaon decays in the detector has determined the beam track momentum and direction resolution requirements. From this study and taking into account the expected STRAW resolution, it has been derived that the Gigatracker has to measure the momentum with a relative resolution of $\sigma(P_K)/P_K \sim 0.2\%$ and the direction with a resolution of the order of 16 μrad. A pixel size of 300×300 μm^2 is sufficient to achieve the required resolution. Finally the beam spectrometer has to sustain a high and non-uniform beam rate of 0.75 GHz in total, hence the name Gigatracker, with a peak of 1.3 MHz/mm^2 around the center. Required time resolution on every single track using all three stations is 150 ps.

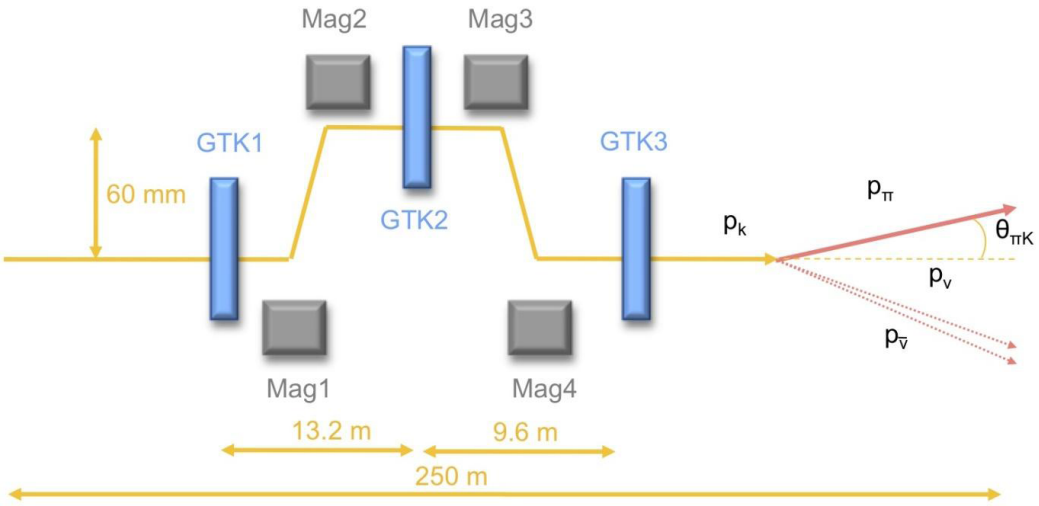

Figure 2.6: GigaTracKer conceptual scheme layout.

The spectrometer is composed of three hybrid silicon pixel stations. Each station is made of one hybrid silicon pixel detector with a total size of 63.1×29.3 mm^2 containing 18000 300×300 μm^2 pixels arranged in a matrix of 90×200 elements (Figure 2.7). With this configuration the detector matches the expected beam dimensions of ∼60×27 mm^2. The pixel dimensions and the distances between stations are adapted to deliver the required momentum and direction resolution. The amount of material crossed by the beam at each station influences the angle measurement. The chosen sensor thickness of 200 μm corresponds to 0.22% of a radiation length (X_0). The design efforts take into account to minimize the material as much as possible as the physics performance strongly depends on a low material budget. Giving an equiv-

alent budget to the read-out and to the cooling the total amount of material per station has been required not to exceed 0.5% X_0.

Hybrid pixel detector modules establish electrical connections between the silicon sensor and the read-out chips using Sn-Pb solder bumps. For the GTK, the sensor thickness is 200 μm and the thickness of the read-out chips is 100 μm. In order to minimize material and maximize geometric efficiency in the active beam area any connections to the read-out chip are outside the beam area. The beam profile has been adapted in such a manner that two adjacent rows of read-out chips cover the beam area (see Figure 2.8).

GTK will provided by a cooling system that will keep the operational temperature at 5 C° In Figure 2.9 is reported the first realized vessel that will provide support and cooling using a nitrogen flux at 100 K.

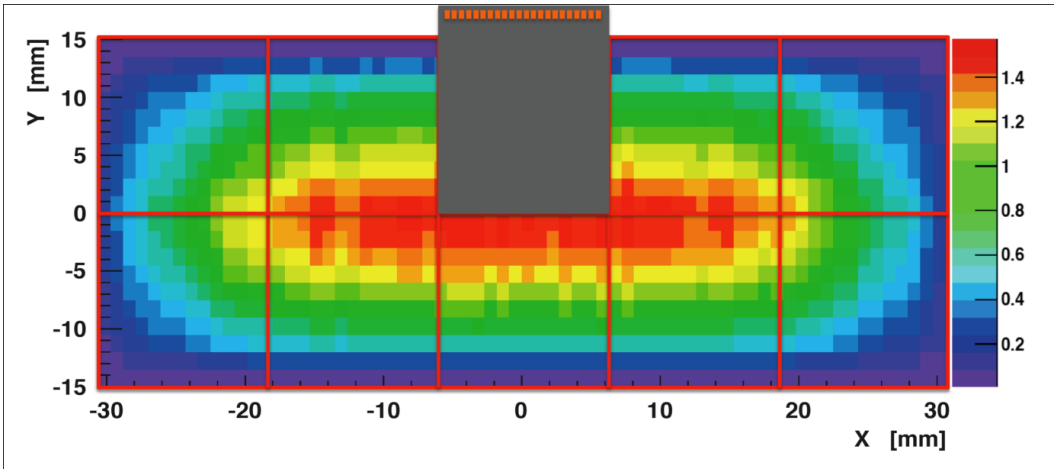

Figure 2.7: The beam intensity in rainbow scale and one readout chip scratch.

2.5 STRAW chamber

The spectrometer (see Figure 2.10) consists of four chambers intercepted in the middle by a high aperture dipole magnet providing a vertical B-field of 0.36 T.

Each chamber is equipped with 1792 straw tubes, which are positioned in four "Views" providing measurements of four coordinates (see Figure 2.11). The main building block of the detector is an ultra-light straw tube which is 2.1 m long and 9.8 mm in diameter (see Figure 2.12). The tubes are manufactured from 36 μm thin PET (PolyEthylene Terephthalate) foils, coated -on the inside of the tube- with two thin metal layers (0.05 μm of Cu and 0.02 μm of Au) to provide electrical conductance on the cathode. The anode wire (diameter 30 μm) is gold-plated tungsten. Staws are arranged as reported in Figure 2.13.

Kinematical separation requires a $\sigma(P_K)/P_K \leq 1\%$ and $\Delta_{K\pi} \leq 60$ μrad.

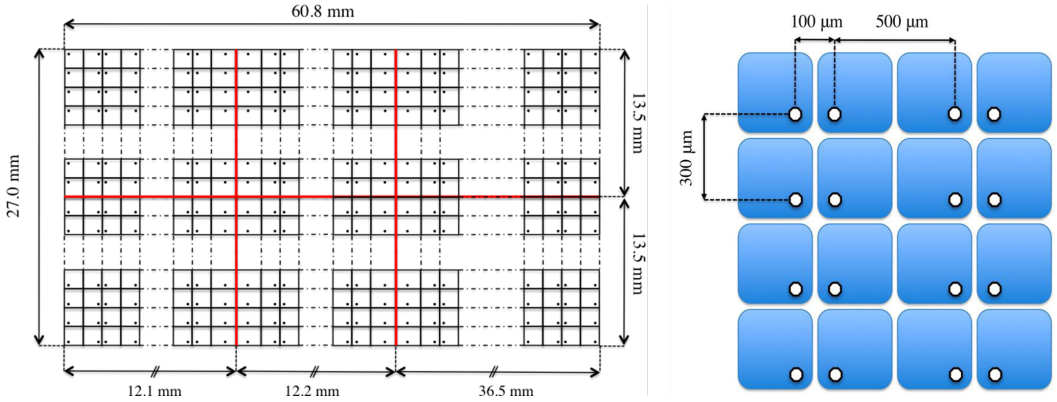

Figure 2.8: On left side we can observe the final GTK overall structure, on right side a magnification on few pixel has been reported; circles represents the bump bonding.

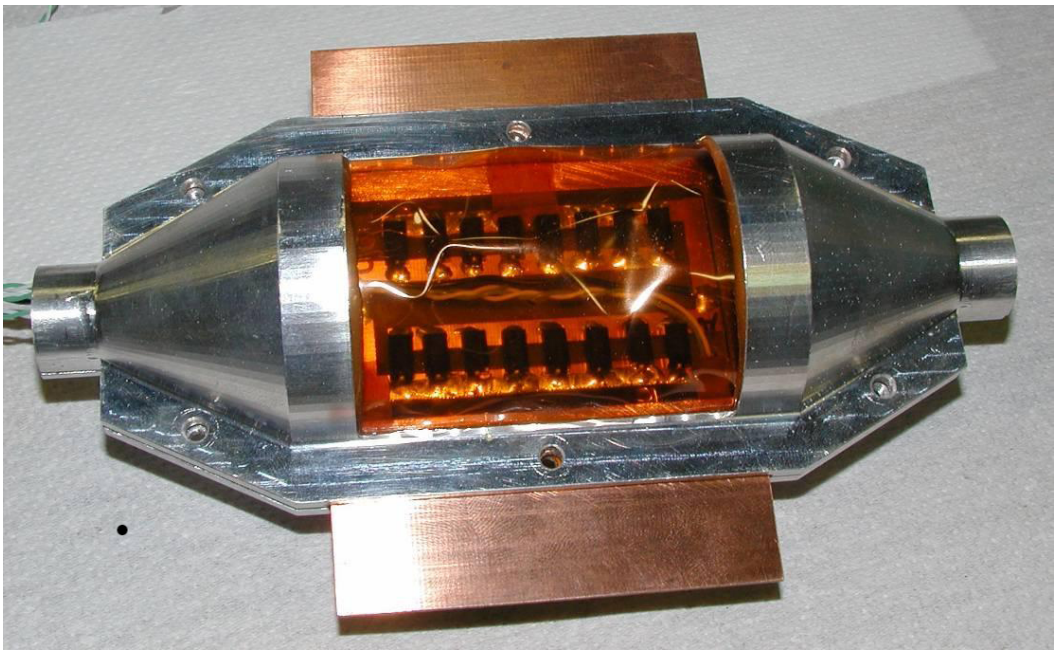

Figure 2.9: First GTK station support and cooling facility.

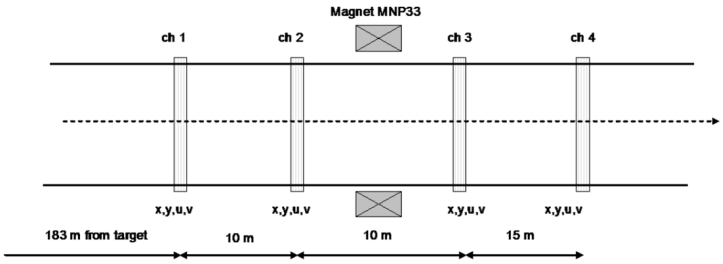

Figure 2.10: STRAW spectrometer conceptual scheme.

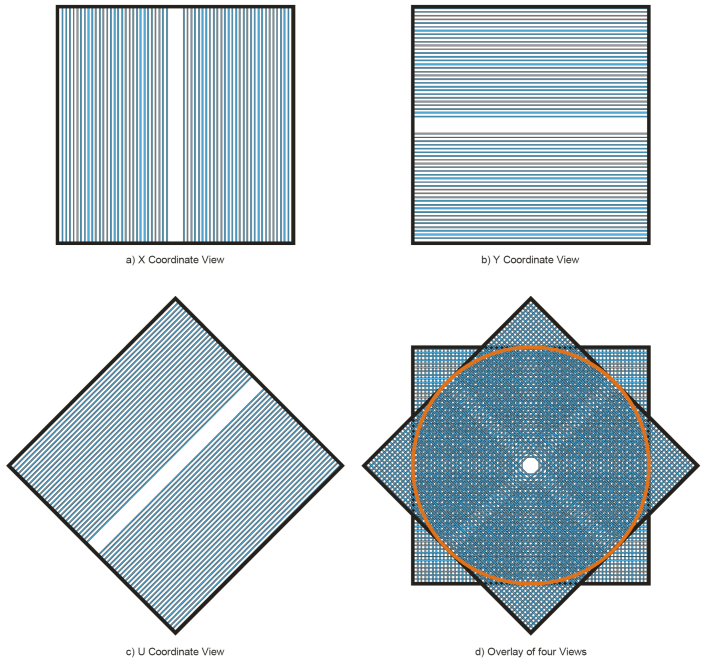

Figure 2.11: Schematics of four STRAW views. a) the x-coordinate view with vertical straws, b) Y-coordinate View with horizontal straws, c) the U-coordinate view (the V-coordinate view is rotate by 90 degrees compared U-Coordinate), d) A full chambers consisting of the X,Y,U and V Views; the active area of the chamber covers a diameter of 2.1m. The gap near the middle of each layer is kept free for the beam passage..

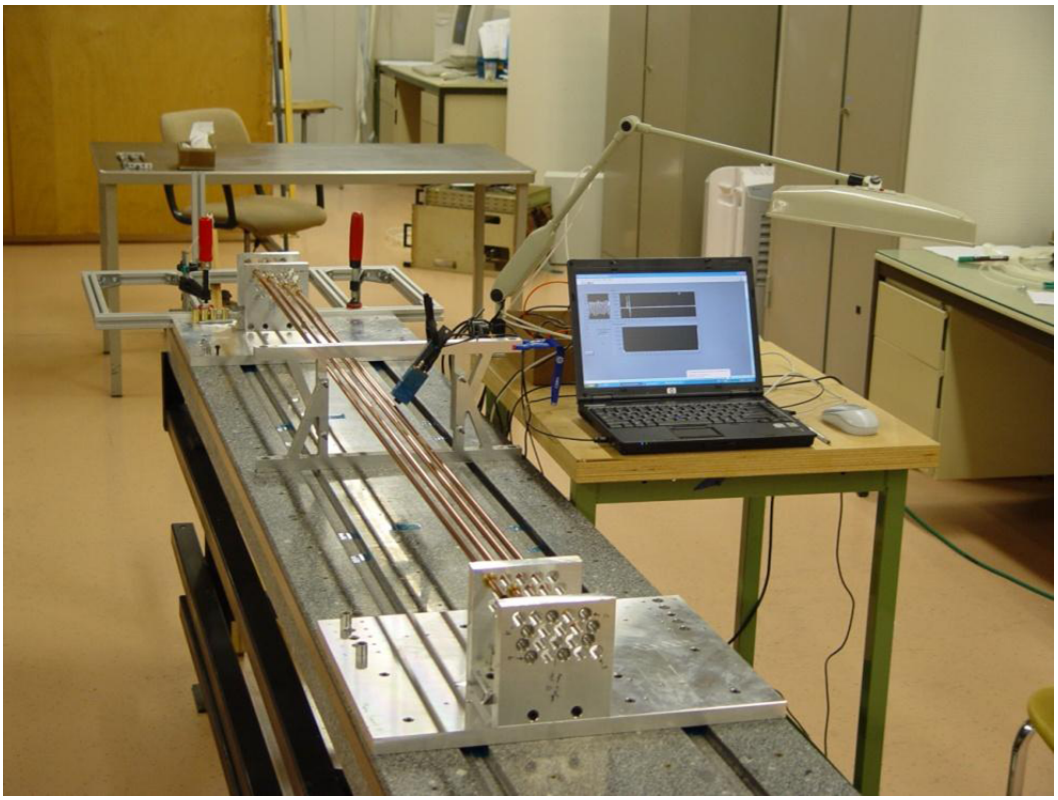

Figure 2.12: Some examples of STRAW tubes.

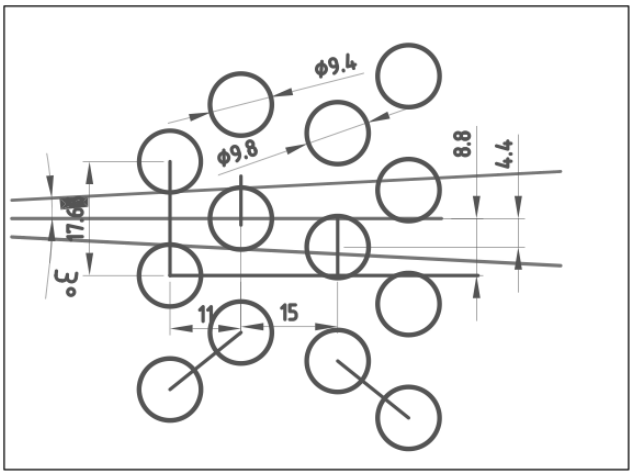

Figure 2.13: STRAW tube orthogonal beam arrangement.

2.6 RICH

The RIng imaging CHerenkov (RICH) aims to separate pions and muons into energy range 15-35 GeV/c (providing a muon suppression factor of at least 10^{-2}) and to measure the pion crossing time with a resolution of 100 ps.

The first requirement leads to the choice of Neon gas at about atmospheric pressure as the Cherenkov radiating medium; a reasonable compromise between the number of produced photoelectrons [9] (linear with the radiating medium length) and the available space in the NA62 layout between the last straw chamber and the LKR calorimeter is achieved with a gas container not longer than 18 m in the beam direction. The second requirement leads to the choice of fast single anode photomultipliers, while the first one would point to PM as small as possible and packed as close as possible.

During RICH tank design, we needed to be driven by some basic criteria (Figure 2.14):

- Develop a rational installation strategy with in-situ part assembly and alignment possibilities for this large size vessel.
- Provide a tight, clean and non-reflective containment to the radiator gas. Provide a stiff gas containment, keeping in mind possible pressure variations, between 0 and 150 mbar overpressure.
- Hold the mirror support panel at the downstream end; provide possibilities for fine-adjustment.
- Support a beam pipe.
- Provide minimal-material budget, in the form of "entrance window" and "exit window" respectively, of the frontal surfaces at the upstream and downstream vessel ends. The minimal-material outer diameters are dictated by criteria of downstream photon acceptance. Furthermore, minimal material near the beam axis is especially important.
- Provide as rational as possible an interface between the decay vacuum volume and the radiator gas volume.

Cherenkov cone is imaged in a ring using a mosaic of 20 spherical mirrors (see Figure 2.15), the segmentation was suggested by large reflective area needed (6 m^2). To avoid absorption of reflected light on the beam pipe the mirrors are divided into two spherical surfaces: one with the centre of curvature to the left and one to the right of the beam pipe. The mirror is placed at down stream edge of the tank. In front of it, in focal plane is present the PMT matrix (see Figure 2.16) that will detect the optical photons reflected by mirror mosaic. PMT used are Hamamatsu R7400 series.

A RICH prototype was built to demonstrate the feasibility of the RICH project. The radiator was cylindrical, 17 m long and 60 cm diameter, filled with Neon gas

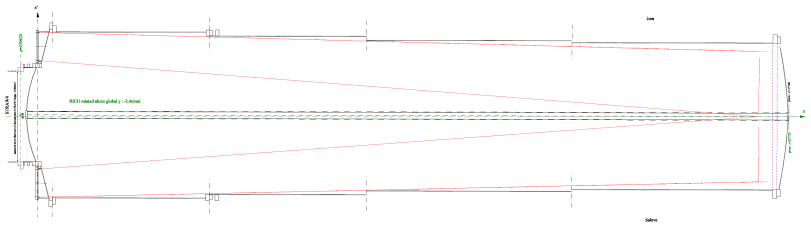

Figure 2.14: RICH overview.

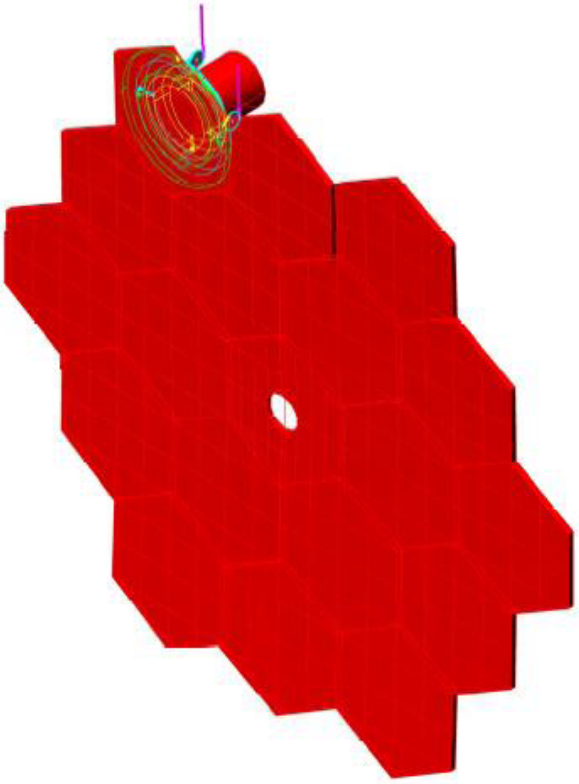

Figure 2.15: RICH mirror as mosaic of hexagonal sub-mirrors.

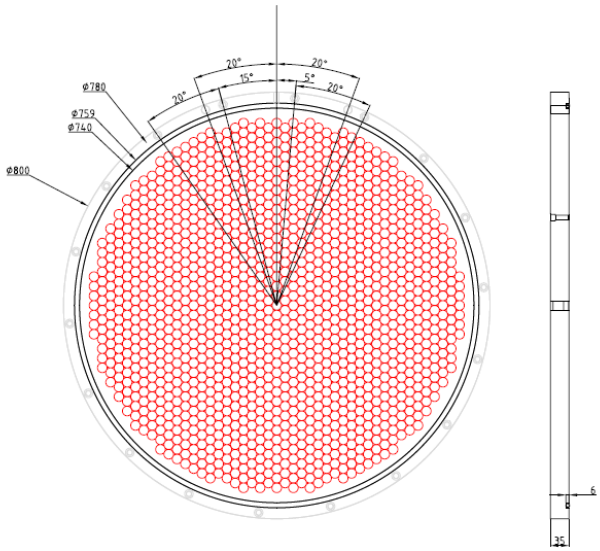

Figure 2.16: RICH photomultipliers arrangement with rings produced by incoming particles.

at atmospheric pressure. A spherical mirror with 17 m focal length was used with PMTs placed in the mirror focal plane. In spring 2009 the RICH prototype was equipped with 414 PMTs of Hamamatsu R7400U-03 type to validate the $\mu - \pi$ separation and measure the time resolution [11] . In Figure 2.17 are reported the μ/π separation at 15 GeV/c and the time resolution as momentum function.

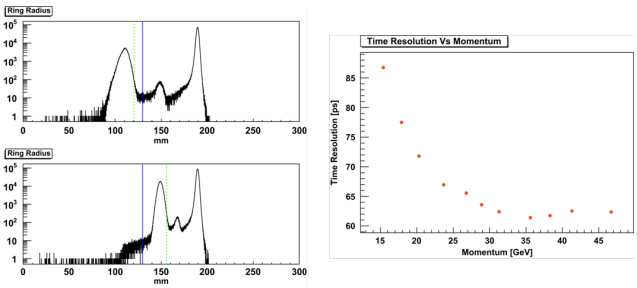

Figure 2.17: Data at 15 GeV/c for π (top plot) and μ (bottom plot) are reported on left side; leftmost peak represents the signal (respectively μ from π); the smallest peak is given by true μ from π decays before the beam momentum selection magnets. The rightmost peak is due to positrons contamination. Time resolution as a momentum beam function is reported on right side.

2.7 Photon Veto system

Photon vetoes are required to suppress the dominant background originating from the decay $K^+ \to \pi^+ \pi^0$ (BR=20.7%) to the specified level. The average inefficiency for π^0 rejection should be smaller than 10^{-8}. The photon vetoes need to have hermetic geometrical coverage up to 50 mrad for the photons originating from the kaon decays occurring in the decay fiducial region. With such a configuration, only about 0.2% of the $K^+ \to \pi^+ \pi^0$ events have one photon from the π^0 left undetected.

The geometry of the experiment suggests partitioning of the detector into three different angular regions, each instrumented by three different detector technologies:

1. Large Angle Vetoes (LAV), covering the angular region between 8.5 mrad and 50 mrad, distributed along the decay volume and spaced by 6 m in the upstream region and by 12 m downstream

2. the NA48 Liquid krypton calorimeter (LKR), covering angles between 1 and 8.5 mrad

3. small angle vetoes covering the region down to zero degrees (SAC) and the zone around the inner radius of the LKR (IRC) calorimeter. These will have suitable overlap in the angular acceptance to cover the beam pipe and an inner radius smaller than that of the beam pipe.

The kinematics of $K^+ \to \pi^+ \pi^0$ decay in the NA62 decay volume is such that, with a cut on the momentum of the charged pion, only three possible configurations are present:

- both photons from the π^0 hitting the forward calorimeters with a total energy larger than 20 GeV;

- one photon in the forward calorimeters and the other one in the Large Angle Vetoes;

- one photon in the forward calorimeters and the other one lost at angles larger than 50 mr.

This last combination occurs only in 0.2% of the decays. In order to achieve the required π^0 rejection, all photon veto detectors must have an inefficiency lower than 10^-4. With this requirement, the major contribution to the global inefficiency comes from the 0.2% of events where only one photon is detected.

2.7.1 Large Angle Veto

The Large Angle Veto is to be composed of 12 stations situated between 120 and 240 m along Z. The first eleven stations are part of the vacuum decay tube, while the last one is located outside the vacuum tank. The basic building blocks of these detectors are lead glass crystals with attached photomultipliers (PMT) from the former OPAL electromagnetic calorimeter. Four crystal detectors (lead glass crystals + PMTs) are

mounted on a common support structure forming an azimuthal segment. Inside the vacuum tube the azimuthal segments are assembled to form a complete ring of lead glass blocks. Each LAV stations is made up of 4 or 5 rings, which are staggered in azimuth providing complete hermeticity of at least three blocks in the longitudinal direction. All the counters in a complete ring of lead glass lie in one plane that is perpendicular to the beam line, with all the PMTs on the outside of the ring.

LAV is described in details in Chapter 3.

2.7.2 Liquid Krypton electro-magnetic calorimeter

The NA48 Liquid Krypton calorimeter is used to cover the angle between 1 and 15 mrad.

It is quasi-homogeneous detector that use Liquid Krypton as medium (see Figure 2.18). Kripton was chose because it was the best compromise between costs and characteristics. In particular Krypton has a radiation length of 47 mm and a Moliére radius of 61 mm.

LKr transverse shape is octagonal with a central hole radius of 8 cm that allows non decayed particles to pass-through without interferences.

Each cell is designed with two cathodes and one anode. Thin Cu-Be ribbons were chosen to construct the electrodes in the form of longitudinal towers of about 2×2 cm^2 cross-section (see Figure 2.19). The operational supply is about 3000 V and is able to drift charged particles. At the downstream end, the anodes were directly connected to preamplifiers via low inductance decoupling capacitors and, through high impedance resistors, to the high voltage (3000 V) which produced the drift field.

The overall LKr longitudinal length is 27 X_0.

A very detailed LKr description can be found in reference [21].

Inefficiency of LKr must not exceed 10^{-5} for photons with energies above 10 GeV and less than 10^{-3} for photons above 1 GeV. Data of NA48/2 experiment have been used in order to measure the LKr inefficiency at accuracy level we need in the energy range above 10 GeV. The result is $(2.8\pm1.1_{stat}\pm2.31_{syst})\times10^{-5}$ in accordance with requirements [27]. A dedicated run was developed in order to measure LKr inefficiency into photon energy range 3-10 GeV. Preliminary analysis results are in accordance with requirements.

2.7.3 IRC and SAC Calorimeters

Hermeticity for photons flying at angles near to zero with respect to the kaon flight direction, is provided by two photon veto detectors are necessary. One of them is supposed to be placed in front of the LKR, the Inner Ring Calorimeter (IRC), and the other at the end of the experimental setup, the Small Angle Calorimeter (SAC).

Both SAC and IRC are exposed to photons with energies higher than 5 GeV. In order to achieve the necessary suppression of the background from $K^+ \to \pi^+ \pi^0$ decays, SAC and IRC have to provide detection inefficiency better than 10^{-4}. The

Figure 2.18: LKr installed into ECN3 cavern.

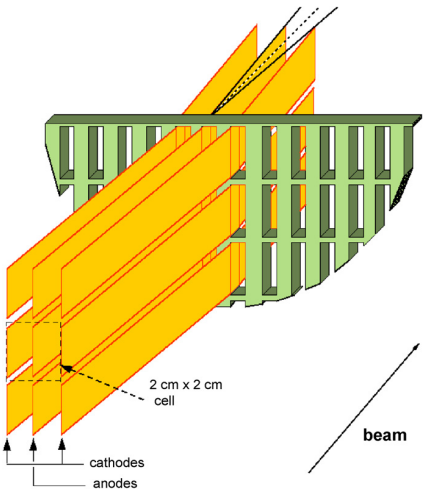

Figure 2.19: Basic LKr cell.

IRC detector will be situated around the beam pipe and its active volume should start as close as possible around the non-decayed kaon beam from one side and far enough so that the beam halo does not generate extremely high rate. Since the SAC is the last downstream detector the only geometrical requirement is to cover the region not covered by IRC and LKR and to have dimensions small enough not to enter the deflected undecayed beam.

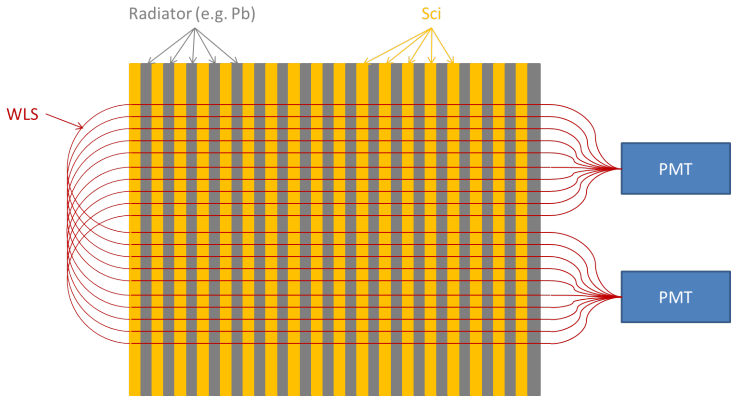

Figure 2.20: Conceptual scheme of a generic shashlyk detector, all elements are drawed with different colors: radiator medium (gray), scintillator (orange), WLS (ref); the choice if PMT as redout photodetector is arbitrary but of common use.

Both IRC and SAC will be implemented using "shashlyk" technology (see Figure 2.20). This kind of detectors are based on consequent lead and plastic scintillator plates. The incoming electron or photon interacts with the lead and develops an electromagnetic shower. The charged products of the shower produce scintillation light inside the plastic material which afterwards could be absorbed and re-emitted to longer wavelengths by fluorescenting additions. This allows to diminish the total attenuation length. The light is taken out by wavelengths shifting fibers to a photodetector. The fibers pass through the plastic scintillator and lead plates via holes in the plates.

A single module of shashlyk type calorimeter is also a single channel detector. The attenuation length of the emitted scintillation light in the plastic scintillator is much bigger than the actual transverse size of the module which leads to light in all the fibers. It is important to note that splitting of the total number of fibers into bunches to be readout by different photodetectors does not reduce the single channel rate but only matches the geometry and the surface of the active photocathode area to the total surface of WLS fibers.

SAC will operate in vacuum and will be placed on a rail in an approximately 7 m long 100 cm diameter vacuum tube at the very end of experiment (just before the beam back-splash). The detector itself will stay on a table which will be supported from bellow on two rails which will be statically attached to the vacuum tube (welded). The table will have ability for hight adjustment (Y axis) and rotation in

the XZ plane (along Y axis). A total amount of 80 square plates will be produced with dimensions 260×260 mm^2 and thickness 1.5 mm. Symmetrically with respect to the center of the plates 784 holes with diameter 1.5 mm will be made in 28 columns each with 28 holes. Between the scintillator and lead plates Tyvek© paper will be put. Also the whole detector will be wrapped in Tyvek©. Read out will be provided by WLS fibers grouped in order to match with PMT cathodes.

First prototype was constructed in 2007, it is pictured in Figure 2.21

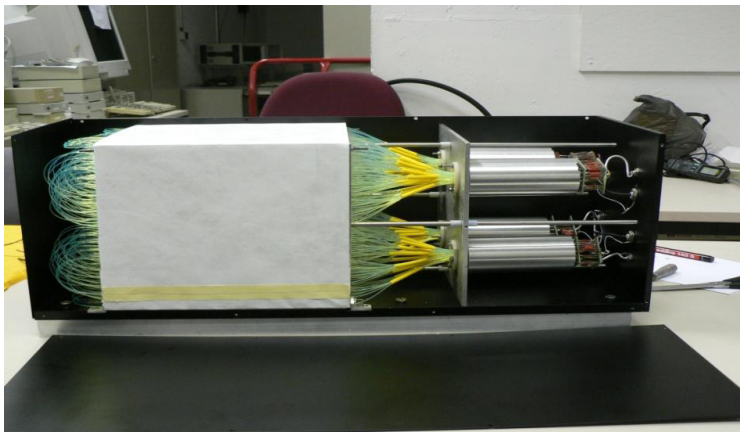

Figure 2.21: SAC prototype.

IRC detector will be made as a cylindrical tube with active region with front inner radius of 70 mm and outer radius 145 mm. In order to prevent inefficiency for photons flying along the WLS fibers the detector will be made in the form of two parts, each of 35 layers of lead and scintillator plates, with WLS fibers common for both halves (see Figure 2.22). The second half of the detector will be with inner radius of 71 mm in order to prevent photons hitting the edges of the detector too far downstream and escaping detection. It will be rotated at 40 mrad with respect to the first half along Z axis leading to approximately 2.9 mm distance between the holes in the XY direction of the two halves at 72 mm radius and 5.8 mm distance at 145 mm radius (3.7 mm closest distance between the holes). The small rotation angle in the XY plane of the experiment will provide the necessary coverage for the whole geometrical region. The lead plates will be made as a single ring converter. The same identical matrix as for the SAC with an additional tool to fix the ring lead plate at the center of it for the holes drilling will be used. The inner ring calorimeter will be segmented into four parts, each representing 90 degrees sector. The segmentation will be achieved by dividing the scintillating tiles into four sectors. Each tile will have its edges aluminized in order to avoid cross talk between the four channels. The IRC will be equipped with four photomultipliers with additional high voltage stabilizer in order to assure stable operation in high rate regime.

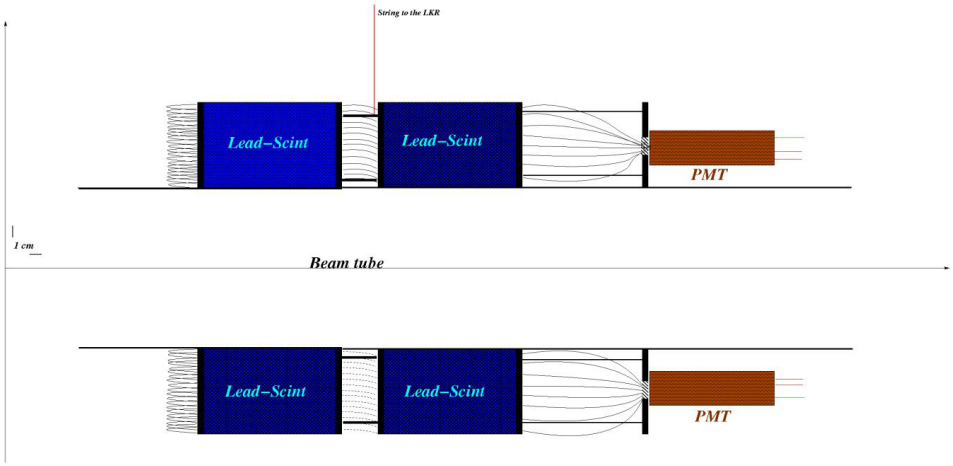

Figure 2.22: IRC conceptual design.

2.8 MUon Veto

In addition to the straw chambers and the RICH detector, further muon reduction of the order of 10^{-5} with respect to pions is required and has to be fulfilled by the calorimetric and muon veto systems. The major part of the rejection is achieved by just requiring charged particles not to deposit significant energy in the calorimeters and to traverse a sufficiently thick layer of iron. However, in order to obtain the necessary total rejection power, muons that undergo catastrophic bremsstrahlung or direct pair production and deposit a major fraction of their energy in the calorimeters also have to be suppressed. To reject these rare events, electromagnetic muon showers must be distinguished from hadronic pion showers by measurements of the shower shape, therefore requiring a sufficient segmentation of the calorimetric system.

In order to suppress muon events already at the first trigger level by a factor of at least 10, a fast muon veto detector is needed. This sub-detector should have a time resolution of less than 1 ns to reject events with coincident signals in the GTK and the CEDAR.

The MUV consists of three distinct parts, called MUV1, MUV2, and MUV3 according to their longitudinal position along the beam axis. The first two modules, MUV1 and MUV2, follow directly the LKR calorimeter and work as hadronic calorimeters for the measurement of deposited energies and shower shapes of incident particles.

Both modules are classic iron-scintillator sandwich calorimeters with 24 (MUV1) and 22 (MUV2) layers of scintillator strips. In both modules, the scintillator strips are alternatively oriented in the horizontal and vertical directions. In the MUV1 module, light is collected by wavelength shifting (WLS) fibers, while the MUV2 module routes the scintillator light by light guides directly to photo multiplier tubes (PMTs).

After MUV1 and MUV2 and an 80 cm thick iron wall, the MUV3 module, or Fast Muon Veto, has the aim of detecting non-showering muons and acts as muon veto detector at trigger level. To achieve the required time resolution of less than 1 ns at each transversal position, a design is chosen, which employs scintillator tiles arranged to minimize differences in the light path trajectories. Figure 208 Right: Three-dimensional view of the MUV1 module. Left: View of MUV1 (grey) and MUV2 (blue). The beam is coming from the left.

The MUV1 module consists of 25 layers of steel. The inner 23 layers have dimensions of $2700\times2600\times25$ mm^3, while the first and the last layer have the same thickness, but outer dimensions of 3200×3200 mm^2. These larger layers serve as support for the whole structure and for the WLS fibers, the photo detectors, and the read-out (see Figure 2.23). The whole iron layer structure is held together by 5 cm diameter steel rods in each corner of the module, maintaining a spacing of 12 mm between the plates. In this way, no welding is necessary, and the MUV1 is constructed by simply stacking alternating iron and scintillator layers onto each other. Each iron plate contains a central hole of 212 mm diameter for the beam pipe. For additional stabilization during movements and tilts of the MUV1 module, a steel tube of the same diameter can be inserted and fixed inside the central hole.

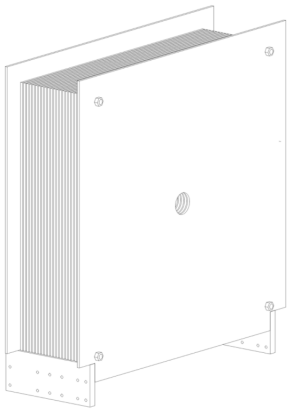

Figure 2.23: MUV1 and MUV2 draft design.

The MUV2 module is the old NA48 HAC front module. The welded iron structure consists of 23 steel layers of $2600\times2600\times25$ mm^3 dimension with 12 mm space between two consecutive iron layers, where a scintillator layer is housed. Each iron plate contains a central hole of 212 mm diameter (see Figure 2.23).

The MUV3 module is located behind an 80 cm thick iron wall filter and serves as a fast muon veto in the lowest trigger level. As a good time resolution is essential, no WLS fibers are used, but instead there are direct optical connections between scintillators and PMTs. The MUV3 will consist of an array of 5 cm thick scintillator tiles. The light produced by traversing charged particles is collected by PMTs positioned about 20 cm down-stream.

2.9 CHarged ANTIcounter

CHANTI is intended to prevent false signal event due to mis-reconstructed pion coming from inelastic events of primary beam, onto third GTK station (GTK3). It is designed as a series of guard rings, as close as possible to GTK3, with the idea to indirectly veto such kind of events.

CHANTI is described in details in Chapter 4.

2.10 CHarged hODoscope

CHOD will be used to detect possible photo-nuclear reaction in the RICH mirror plane and to back-up the RICH in the L0 trigger for charged tracks. CHOD will be provided by the existing NA48 charged hodoscope, that is a system of scintillation counters with high granularity and excellent time resolution (200ps) [21].

The detector consists of 128 detection channels which are arranged in two planes of 64 horizontal and vertical scintillators. Each plane is divided in four quadrants with 16 counters (see Figure 2.24), so that the acceptance in the X-Y plane covers a radius of 121 cm. The counters are made with BC408 plastic scintillators which have fast light output and good attenuation properties. The scintillation light from each counter is collected via a short fishtail (made of Plexiglas) light guide, followed by a Photonis XP2262B photomultiplier.

CHOD will provide an extra veto factor for π^0 decays. In fact the RICH mirror system amounts to about 20% of radiation length and photons from π^0 decays can convert or, even more critical, undergo photonuclear interactions producing low energy hadrons. The Liquid Krypton Calorimeter (LKR) -as subsequent photon detector- has to veto these photons with an inefficiency that is better than 10^{-5}. MC simulations show that photons - which experience photo-nuclear reactions in the RICH - can weaken the photon-veto function of the LKR. In order to re-establish the veto sensitivity to the required level a detector for low momentum charged track after the RICH is needed. This function can be fulfilled by the CHOD.

Another motivation for keeping the present CHOD detector is its timing capabilities, which can be useful in complementing the RICH detector in the L0 trigger selecting charged tracks. The time resolution of an individual plane remains, however, limited by the size and the age of the counters to a level between 3 and 5 ns. This resolution can be improved (drastically) if the two planes are used simultaneously to correct the timing with respect to the crossing point of the track.

The frontend and readout electronics of the CHOD detector have to be entirely re-done in order to cope with the particle flux rate in the CHOD, which is estimated to be around 11 MHz.

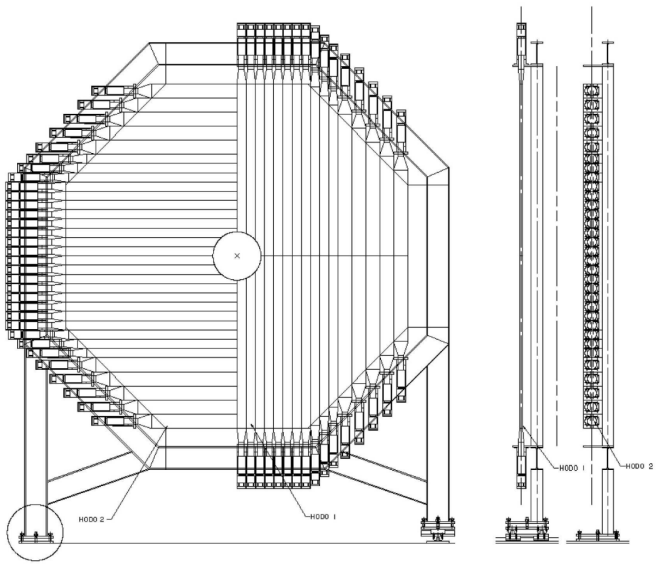

Figure 2.24: CHarged hODoscope design.

2.11 Trigger and Data AcQuisition

The intense flux of a rare decay experiment, such as NA62, necessitates high-performance triggering and data acquisition. These systems must minimize dead time while maximizing data collection reliability. A unified Trigger and Data AcQuisition (TDAQ) system, which, as much as possible, assembles trigger information from readout-ready digitized data, addresses these requirements in a simple cost-effective manner. The NA62 experiment consist of 12 sub-detector systems and several trigger and control systems, for a total channel count of ∼100 thousand. The GTK has the most channels (54,000), and the Liquid Krypton (LKR) calorimeter shares with it the highest raw data rate (19 GB/s).

A common coherent clock, with a frequency of approximately 40 MHz, generated centrally by a single free-running high-stability oscillator, will be distributed optically to all systems through the Timing, Trigger and Control (TTC) system designed and used for LHC experiments [1]. This "TTC clock" will be the common reference for time measurements.

A common time scale is defined by a 32-bit time-stamp word, with 25 ns LSB and covering the full duration of the interval between two consecutive SPS spills, plus an 8-bit fine time word, with 100 ps LSB. While the time tamp will be defined in each system by the phase-coherent distributed clock, each sub-system will locally generate by multiplication a properly locked reference for the fine time. All clock counters should simultaneously reset at the start of each burst, using an appropriate synchronous command sent to all sub-systems through the TTC link before the actual arrival of the first beam particles. This will also define the origin of the time

measurements for the burst. An end-of-burst signal should be sent in the same way some time after the end of the spill, defining the largest time tamp for the current spill. Its value should be recorded by each system and sent to the readout for logging, allowing (online and offline) a consistency check of the number of clock cycles counted by each system during each spill.

The trigger hierarchy is made of three logical levels:

- a hardware L0 trigger, based on the input from a few sub-detectors; after a positive L0 is issued, data is readout from front-end electronics buffers to dedicated PCs;
- a software L1 trigger, based on information computed independently by each complete sub-detector system, using data stored on dedicated PCs;
- a software L2 trigger, based on assembled and (partially) reconstructed events, in which complex correlations between information from different sub-detectors is possible, using data stored on the event building PC farm.

The hardware L0 trigger will be mainly based on input from the CHOD, the MUV, and the LKR, and optionally the RICH, the LAV, and the STRAW. The default (primary trigger) algorithm will be implemented to collect events with a single track in the CHOD, nothing in the MUV, and no more than one cluster in the LKR. The inclusion of other sub-detector information is possible, both to refine the primary trigger and to implement secondary triggers for control samples and different physics goals: for the main trigger, a multiplicity cut in the RICH and STRAW can augment the positive CHOD indicator, while the LAV might enhance photon and muon vetoing.

The third plane of the MUV (MUV3) will veto muon events, i.e. the major background from $K_{\mu 2}$ decays and the muon halo components from decays upstream of the CHANTI. This rejection is the single largest rate reduction factor at the trigger level. We fixed the maximum L0 rate at 1MHz.

After a positive L0 trigger, all sub-detectors data (with the exception of the LKR) associated with the L0 trigger timestamp, are moved to PCs for initial processing, which includes quality checks and reconstruction, as well as rudimentary pattern recognition.

Most detectors are expected to actively provide L1 Trigger primitives. One PC associated with each sub-detector will be responsible for dispatching asynchronously the L1 trigger primitives for that sub-detector for each L0-triggered event to a central L1 Trigger Processor PC, based on complete sub-detector event data. The L1 Trigger Processor will match these primitives and asynchronously issue a L1 decision, at which time the data will be transferred to the event-building farm or discarded (in the case of a negative L1 verdict). All L0-triggered events will get a L1 decision, and no data should be discarded until that decision has been received. The rate of the L1 trigger is not fixed, and there is no strict maximum latency for it, but L1 trigger evaluations are expected to terminate shortly after the end of each spill.

A L2 trigger will be based on correlations between different sub-detectors. The information upon which these correlations are determined will be provided by event-building PC farms. Most sub-detector activity within an event time window will be at least partially reconstructed in the farm and made available for the L2 trigger decision. All data associated with events satisfying the L2 trigger conditions will be logged to tape. In case L2 trigger conditions are not satisfied for an event, the data will be deleted (a fraction of failed events will be passed for purposes of monitoring and efficiency determination). The rate of the L2 trigger is not fixed a priori, but will be determined by data logging capability.

Chapter 3

Large Angle photon Veto system

As described in Chapter 2 Large Angle photon Veto is part of a larger system called photon veto system which aims to make the apparatus hermetic for photons up to 50 mrad in angle with respect to the beam axis.

LAV will be composed of 12 stations situated between 120 and 240 m along Z (distances are from target; see Figure 3.1). The first eleven stations are part of the vacuum decay tube, while the last one is located outside the vacuum tank.

Main requirements are:

1. Time resolution better than 1 ns (in order to keep an acceptable fake veto)
2. Inefficiency of 10^{-4} for energy over 50 MeV (in order to reach an inefficiency of 10^{-8} on veto π^0 events).

Energy resolution has a lower requirement of $10\%/\sqrt{E(\mathrm{GeV})}$. The choice of technology to use to implement this apparatus needed a 3 years long R&D program. During this period three possible solution were investigated and compared.

In this chapter we will discuss briefly the three possible solutions comparison and the motivation of our final choice. In the second part we will focus on describing the construction and test of first prototype of our final solution.

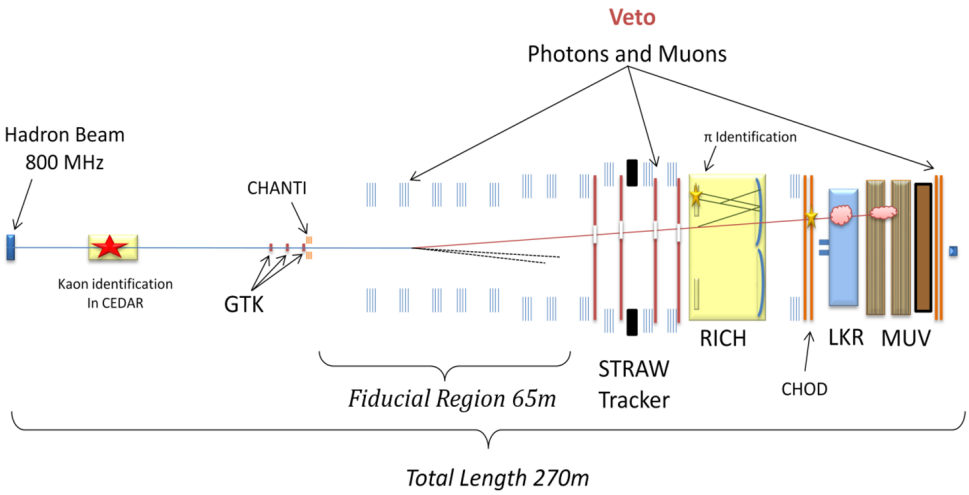

Figure 3.1: General NA62 layout.

3.1 Technology choice

As anticipated above we tested three different technologies during a three years long R&D program. In particular our solutions were:

1. Scintillating-Pb tile sandwich from CKM experiment

2. A self made solution based on KLOE electromagnetic calorimeter

3. An original arrangement of exOPAL electromagnetic calorimeter blocks.

The three solutions and the associate prototype we used for tests are scratched in Figure 3.2 .

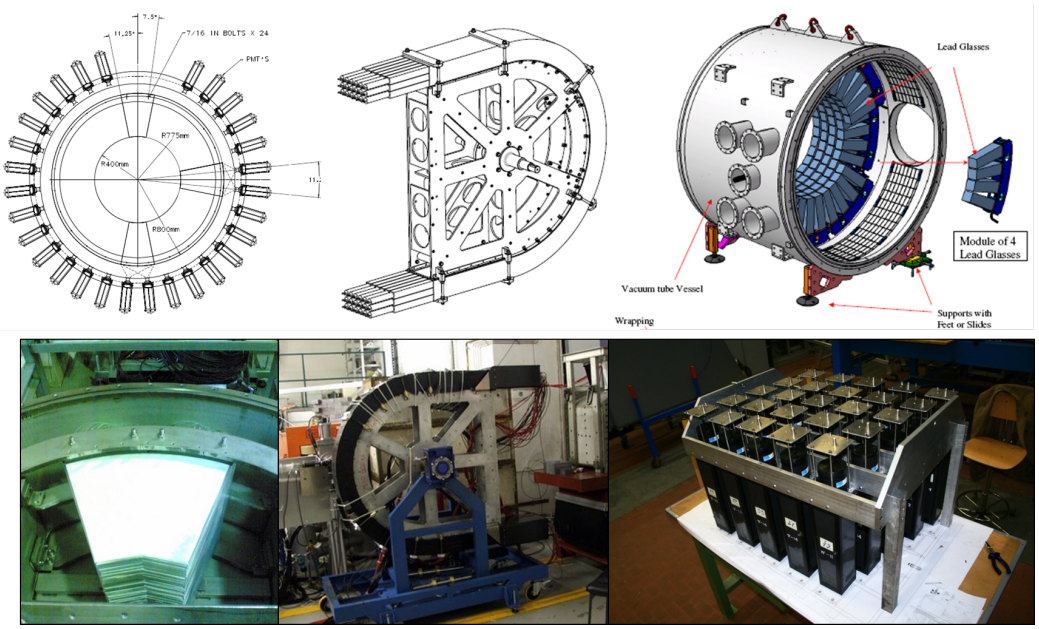

Figure 3.2: Comparison between three LAV constructive solutions (from left): a) CKM tile, b) KLOE like and c) exOPAL blocks; on bottom there are the corresponding prototype we used for comparative tests.

CKM solution

This solution consists of a sandwich of lead sheets and scintillating tiles with WLS-fiber readout. A ring is realized using wedge-shaped modules. An example of such a detector, using 80 layers of 1 mm thick lead sheets and 5 mm thick scintillating tiles, was designed for the (now canceled) CKM experiment at Fermilab [26] . We obtained this prototype on loan from Fermilab for further testing and comparison.

KLOE-like solution

This alternative solution is based on the design of the KLOE calorimeter [24], and consists of 1 mm diameter scintillating fibers sandwiched between 0.5 mm thick lead foils. The fibers are arranged orthogonal to the direction of particle incidence and are read out at both ends by a PMTs matrix. Two U-shaped modules form a veto station. This solution offers advantages in terms of hermeticity, position resolution, and time resolution. A reduced transverse dimension prototype has been constructed at Laboratori Nazionali di Frascati.

exOPAL blocks solution

This is last solution we investigated. A station is an original arrangement of lead glass blocks of the former OPAL electromagnetic calorimeter. Each ring is made of 4 or 5 layers assembled using blocks. This solution could be competitive because a large number of blocks is available. Staggering insures that at least three blocks are involved into particle detection if particle comes orthogonally to the detector front surface. A small prototype was realized at INFN Napoli. It consists of a planar ensemble of 25 blocks that reproduce the real staggering.

3.2 Prototypes test and results comparison

We make a comparative test among the three possible solution. Our figures of merit were essentially the time resolution and efficiency.

We tested these prototypes at Frascati Beam Test Facility [35]. Were an electron beam from DAΦNE linac is available. The linac accelerates e^+'s and e^-'s to maximum energies of 550 and 800 MeV, respectively, producing 10 ns pulses with a repetition rate of 50 Hz. Momentum selection magnets, attenuating targets, and collimation slits upstream of the experimental area can be used to produce test beams in the BTF hall with energies from 100 to 750 MeV with a 1% energy-selection resolution and mean multiplicities from <1 to 10^9 per pulse. The last magnet on the BTF line is a 45° dipole with a hole in the yoke allowing extraction of a photon beam through an uncurved extension of the vacuum chamber.

We have had two different test periods. KLOE like and CKM prototype were tested in June-July 2007, exOPAL block solution was tested in February 2008.

3.2.1 Readout and data acquisition

All prototypes were read out using the BTF front-end electronics and DAQ system. For the fiber and tile prototypes, the PMT anode signals were passively split to obtain both charge and time measurements. CAEN V792 charge-to-digital converters (QDCs) were used for the charge measurements, it is a 12 bit QDC and operated with a 400 pC full scale. CAEN V814 low-threshold discriminators and V775 time-to-digital converters (TDCs) were used for the time measurements. A signal from the linac provided QDC gates and TDC starts, as well as the DAQ trigger.

3.2.2 Beam Tagging System

The telescope of scintillation counters used to tag single electron events is schematically illustrated in Figure 3.4. From upstream to downstream, the following trigger counters, all made of 10 mm thick plastic scintillator, were used:

1. $F1$ a paddle of area 60×85 mm^2, positioned a few centimeters downstream of the beamline exit window;

2. $H1$ a paddle of area 200×130 mm^2 with a 14 mm diameter hole in the center, positioned 10 mm downstream of $F1$;

3. $H2$ a paddle of area 330×100 mm^2 with a 14 mm diameter hole in the center, positioned 90 cm downstream of $H1$.

4. $F2$ a paddle of area 60 × 85 mm^2, positioned 10 mm downstream of $H2$ and as little as 10 mm upstream of the prototype to be tested.

The tagging criterion for single-electron events used in the efficiency studies was $F1 \cdot \bar{H}1 \cdot \bar{H}2 \cdot F2$, where $F1$ and $F2$ refer to charge signals on the paddle counters consistent with passage of a single electron, and $H1$ and $H2$ refer to null signals on the hole counters (see Figure 3.3). Acceptable beam trajectories were thus defined by the two 14 mm diameter holes separate by 90 cm. The use of paddle/hole combinations rather than horizontal/vertical fingers was intended to reduce the amount of material in the beam. The fact that no material occupied the space between the hole counters was intended to facilitate alignment. The thickness of the paddles was chosen to allow efficient identification of events with exactly one electron in the paddles within the 10-ns linac pulse. The large dimensions of the hole counters served to help reject events with stray beam particles present. The use of a paddle (rather than a hole) as the last counter was intended to reduce mistags by providing a positive signal for beam particles just before entry into the prototype. The mistag probability was monitored by taking occasional runs with the last dipole in the BTF beamline switched off, so that the beam was not directed towards the tagger or the prototypes. We did not find any tags in more than 1 million events collected in this configuration, corresponding to a false-tag rate of $<2\times10^{-6}$ at 90% CL. Based on our evaluation of the efficiencies for the $F1$ and $F2$ counters, we expect the contribution from false tags to be insignificant for the purposes of the efficiency measurements. In all cases, we quote efficiencies assuming no contribution from false tags. This assumption is conservative; if there are false tags, they artificially increase the inefficiency.

The tagging system was mounted on a rigid support structure allowing fine and reproducible positioning of all counters in the horizontal and vertical coordinates. To facilitate alignment, the beam position in the bend plane was measured using the BTF beam-profile meters, which were mounted just upstream and downstream of the tagger ($P1$ and $P2$ in Figure 3.4). Each profile meter is a one-dimensional, 16-channel close-packed array of 1-mm scintillating fibers read out by a multianode PMT, with each channel consisting of a group of fibers three across by four deep.

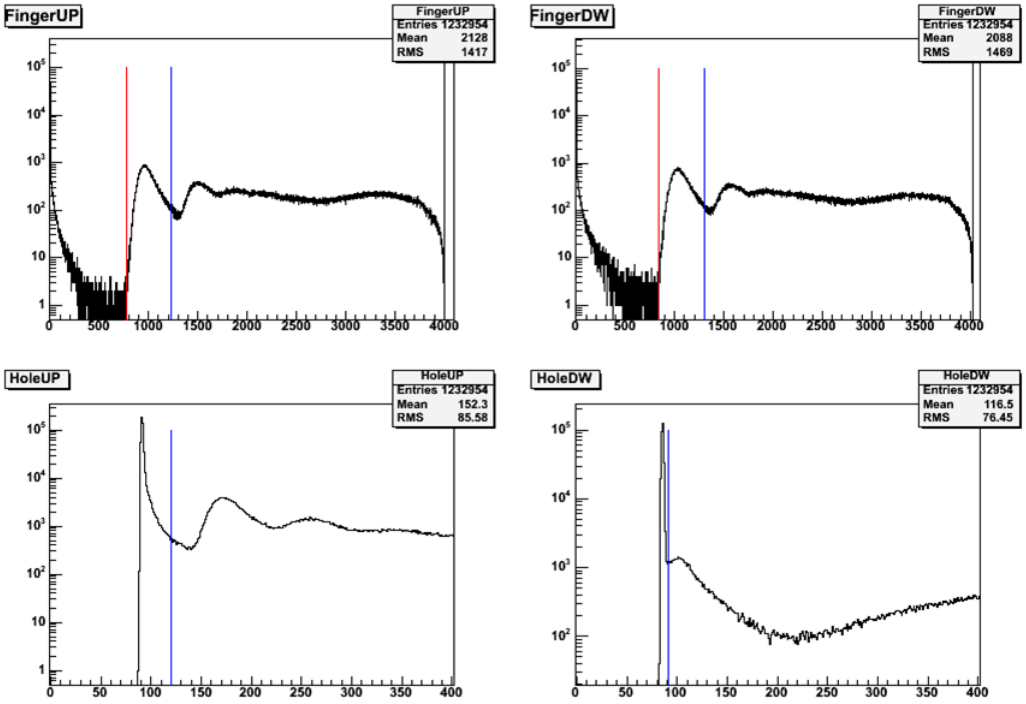

Figure 3.3: Signals from all 4 scintillators of tagging system, on top $F1$ and $F2$ are reported and on bottom $H1$ and $H2$ signals are reported; vertical lines are an example of cuts used into analysis, red line refers to lower bound and blue one refers to upper bound.

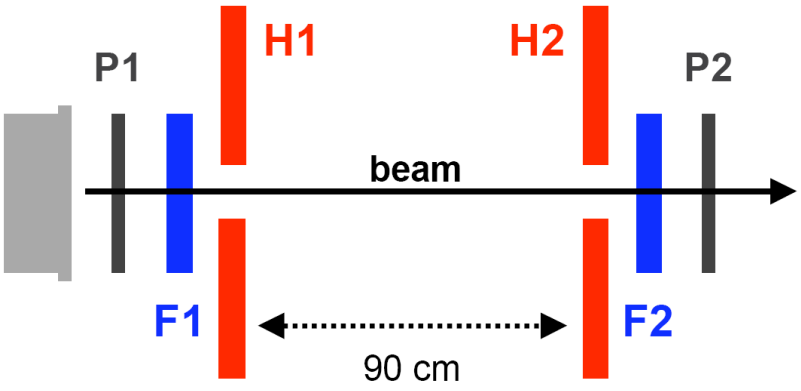

Figure 3.4: Tagging system provide by BTF facility in order to select single electron events.

3.2.3 KLOE like and CKM prototype tests

Prototypes results are almost complete for what concerns the KLOE solution. Moreover some problems due, mainly, to channels cross talk and energy calibration suggested that CKM prototype is not a competitive solution for our purposes. Anyway we have a draft of inefficiency of this module. Following paragraphs are intended to explain energy reconstruction, energy resolution and inefficiency of KLOE solution, a very short table concerning CKM inefficiency has been presented.

3.2.3.1 Energy Reconstruction

We obtain separate energy measurements from the set of PMTs on each side of the prototype (sides A and B). We first subtract the mean noise level from the QDC measurements for each cell. The noise arises from diffuse background in the BTF hall; its mean level is determined from events with no activity in the tagger, and is typically larger than the sum of the hardware pedestals by an amount corresponding to a few MeV integrated on whole detector.

For each side, we take the energy measurement to be the gain-calibrated sum of the signals from all cells for which the uncalibrated QDC measurements are greater than the hardware pedestal by more than 3σ (typically less than 10 counts, or $\sim$1.5 MeV). For the combined energy measurement from both sides, if there are signals above the 3σ threshold from both PMTs, the energy measurement for the cell is the average of the measurements from each side. If instead one PMT gives a signal above threshold and the other does not, the energy measurement for the cell is equal to the measurement from the side above threshold.

3.2.3.2 Linearity and Energy Resolution

Although seemingly a basic test of the prototype performance, the linearity of response is difficult to measure precisely with our setup. This is mainly because run-to-run fluctuations in the energy scale are observed at the $\sim$5% level. Several factors may contribute to such drifts, including limited reproducibility of the beam energy due to hysteresis in the BTF dipoles and possible time (or temperature) dependent drifts in HV power supply voltages or QDC gains. With additional effort during data taking, it should be possible to maintain better stability of the energy scale. In any event, for the energy resolution and efficiency measurements, we calibrate to a reference value of the energy for the single-electron peak, so these small drifts do not pose a problem. When testing the linearity, however, this calibration procedure cannot be applied at more than one energy point. In Figure 3.5, we plot the measured mean value of the energy of the single-electron peak, E_{meas}, as a function of the beam energy, E_{beam}, where the energy scale has been fixed using the point at E_{beam} = 203 MeV. E_{meas} is obtained from Gaussian fits to the single-electron peak over an interval of about $\pm 1.5\sigma$ about the peak. The lower panel of the figure shows the fractional deviation of E_{meas} from E_{beam}. Such deviations are present at the level of $\sim$5%, i.e., at the level of precision with which the energy scale is known.

(The errors on the plotted points include only the statistical measurement errors, plus a 1% systematic error corresponding to the BTF energy-selection resolution.)

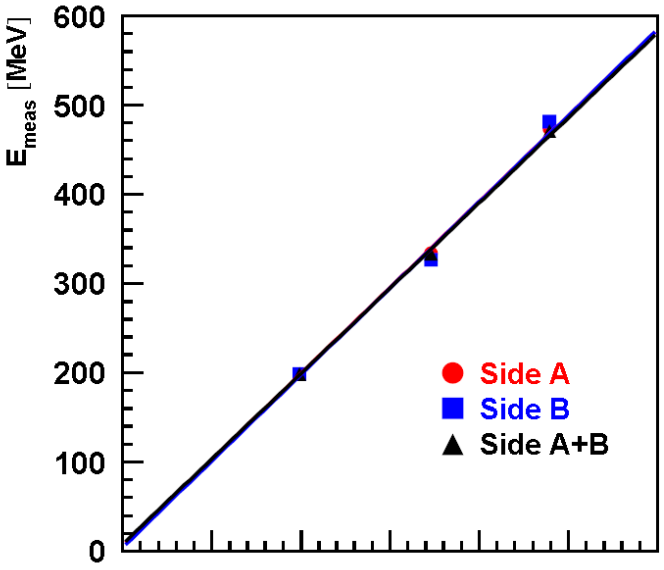

Figure 3.5: On top the measured energy linearity .

We conclude that the response linearity is basically satisfactory. To obtain the energy resolution, the Gaussian fits to the single-electron peak are performed again after the run-by-run energy scale calibration is applied. In Figure 3.5, we plot the relative energy resolution, $\sigma E/\mathrm{E}_{meas}$, as a function of E_{beam}, for the measurements from each side of the prototype and for the combined measurement. The best performance is obtained by combining information from both sides. The curves in Figure 3.6 show the results of fits to the form:

$$\frac{\sigma_E}{E} = \frac{p_1}{\sqrt{E(\mathrm{GeV})}} \oplus p_2 \tag{3.1}$$

Using the information from both sides of the prototype, we find $p_1 = 5.1\%$ and $p_2 = 4.4\%$.

3.2.3.3 Time resolution

In principle, the arrival time of a particle and its impact position along the length of the fibers would be obtained from the sum (average) and difference of the time measurements from the two sides of a cell. However, for the tests described here, the beam was incident at the midpoint of the fibers length; we therefore have independent time measurements from each side of each cell. The time measurements for sides A and B, t_A and t_B, and the combined time measurement t_{A+B}, are taken to be the energy-weighted averages of the time measurements for the corresponding group of cells.

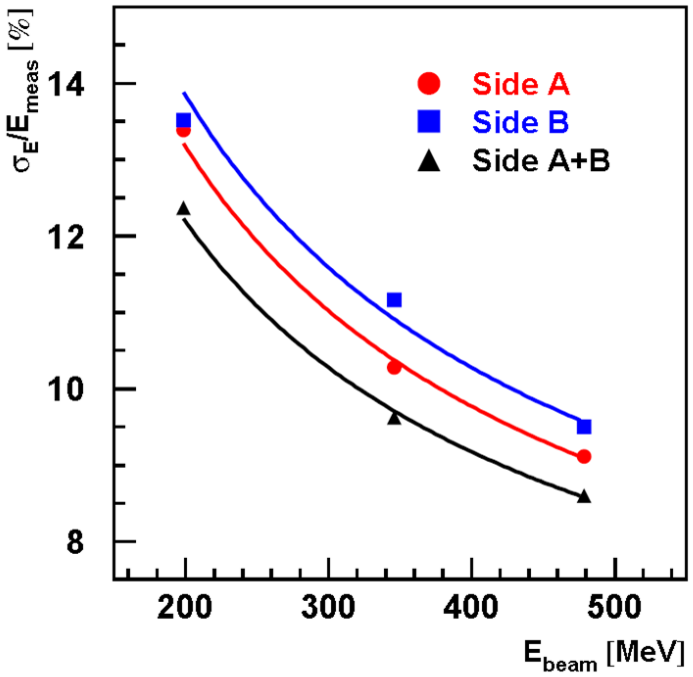

Figure 3.6: Energy resolution for KLOE like prototype.

The event time reference is provided by the tagging system: $t_0 = (t_{F1} + t_{F2})/2$, where $F1$ and $F2$ are the trigger paddles described in Section 3.2.2. Slewing corrections and time offsets for each cell are obtained by fitting the time vs QDC distributions with the form $t\text{-}t_0 \propto (\ln Q_0/Q)^{\alpha} + t_{offset}$, where Q and t are the QDC and time measurements, t_{offset} is the time offset for the cell, and α is positive. Slewing corrections are also necessary for t_{F1} and t_{F2}, so an iterative procedure is applied. Once all slewing corrections have been obtained, we form the distributions of the differences t_A-t_0, t_B-t_0, t_A-t_B, and t_{F1}-t_{F2}; fit with Gaussians; and from the four widths obtain σ_A, σ_B, σ_{t_0}, and σ_{AB}, where this latter quantity accounts for common-mode fluctuations in the time measurements from the two sides ($\sigma^2_{AB} = 2$ cov(t_A, t_B)). The time resolution of the tagging system is found to be t_0 =147 ps and stable for points with different E_{beam}. We obtain the resolution on the combined time measurement for the two sides from the width of the distribution t_{A+B} - t_0, with t_0 subtracted in quadrature. Our results on the time resolution are plotted in Figure 3.7 as a function of E_{beam}. Again, the resolution is better on side A than it is on side B. For the point at 483 MeV, the resolution for the combined measurement is σ_{A+B} = 172 ps, of which 158 ps is due to the common-mode fluctuation in the time measurements from each side. We do not fully understand the origin of this large contribution.

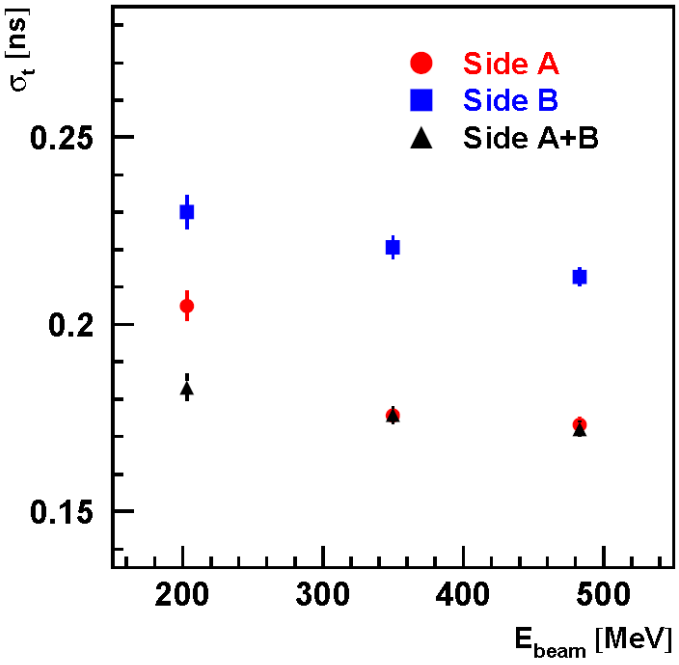

Figure 3.7: Time resolution for KLOE like prototype.

3.2.3.4 Efficiency

Our measurements of the detection efficiency are summarized in Figure 3.8. For each beam energy, the panel on the left shows the energy distribution for all collected events (open histogram) and for fully-tagged events (shaded) histogram. The one and two electron peaks are clearly visible in the distribution for all events; application of the tagging criterion reduces the contribution from multiple-electron events to a negligible level for our purposes. We consider a fully-tagged single-electron event to be undetected if the measured energy is below a threshold value of E_{th} = 50 MeV. At E_{beam} = 203 MeV, we find five such events out of 68 829 total tagged events; at E_{beam} = 350 MeV, we find three out of 207 385; and at 483 MeV, we find one out of 371 633.

We thus quote inefficiencies:

Energy	*Inefficiency*
203	$7.3^{+4.1}_{-3.3}\times10^{-5}$
350	$1.4^{+1.1}_{-0.9}\times10^{-5}$
483	$2.7^{+4.7}_{-1.7}\times10^{-6}$

where the asymmetric uncertainties represent 68.27% unified confidence intervals. We assume that no undetected events are due to false tags. The choice of threshold E_{th} = 50 MeV is reasonable but arbitrary.

A preliminary result concerning the CKM prototype is reported in following table:

Energy	*Inefficiency*
203	$3.1^{+3.5}_{-1.9}\times10^{-5}$
350	$1.4^{+1.0}_{-0.9}\times10^{-5}$
483	$5.2^{+9.1}_{-3.3}\times10^{-6}$

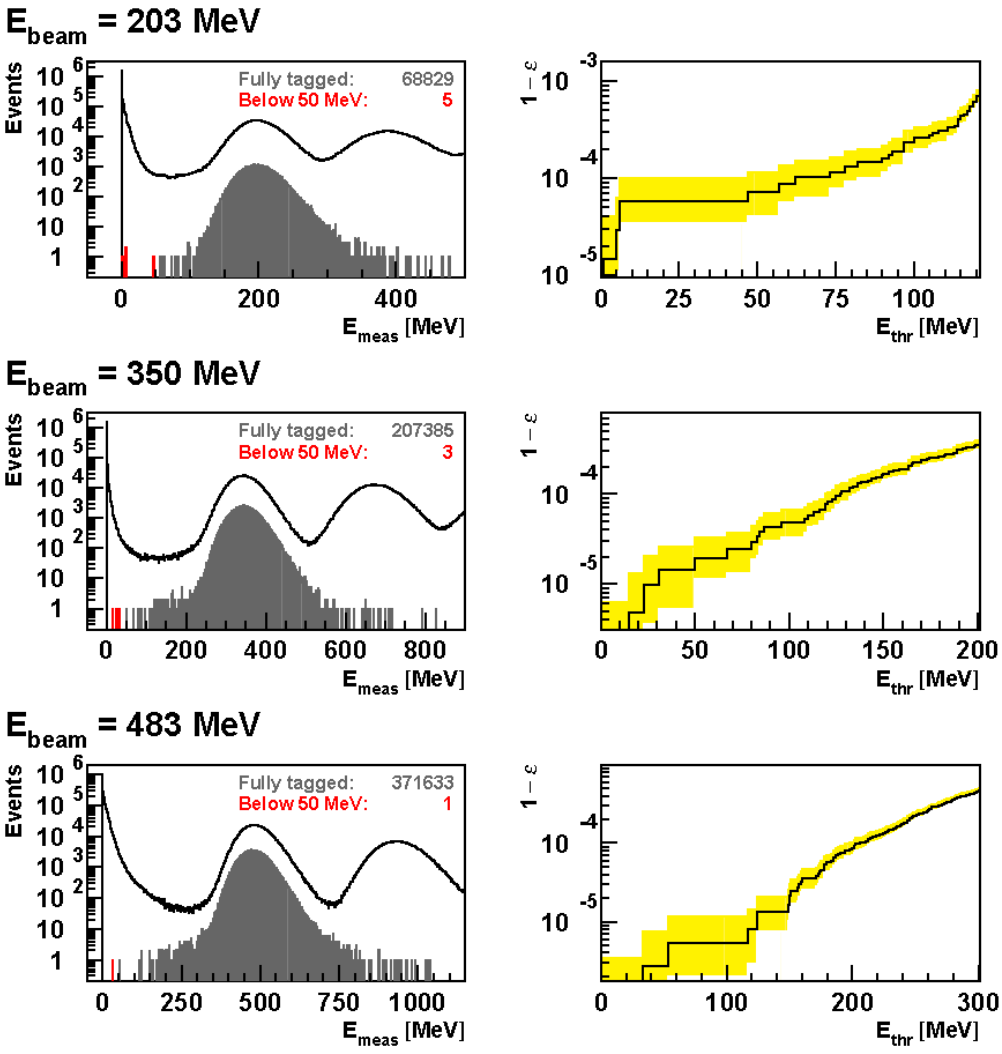

Figure 3.8: KLOE like prototype inefficiency estimation.

3.2.4 exOPAL prototype test

"exOPAL" prototype test was performed in February 2008. Data are available for only one energy value E_{beam} = 471 MeV. This means that no energy resolution

behavior and linearity could be measured. All blocks were equalized at a gain of 10^6. Response equalization was done off-line using Photoelectron Yield (PeY; see Section 3.5.1.3) previously measured. PeY allows us to inter-calibrate all blocks.

3.2.4.1 Data sets

Different datasets were collected. They differs for beam impact point on first layer blocks (see Figure 3.9). These sets were chosen in order to study possible edge effects.

Time information were available only for a subsample of Set 4.

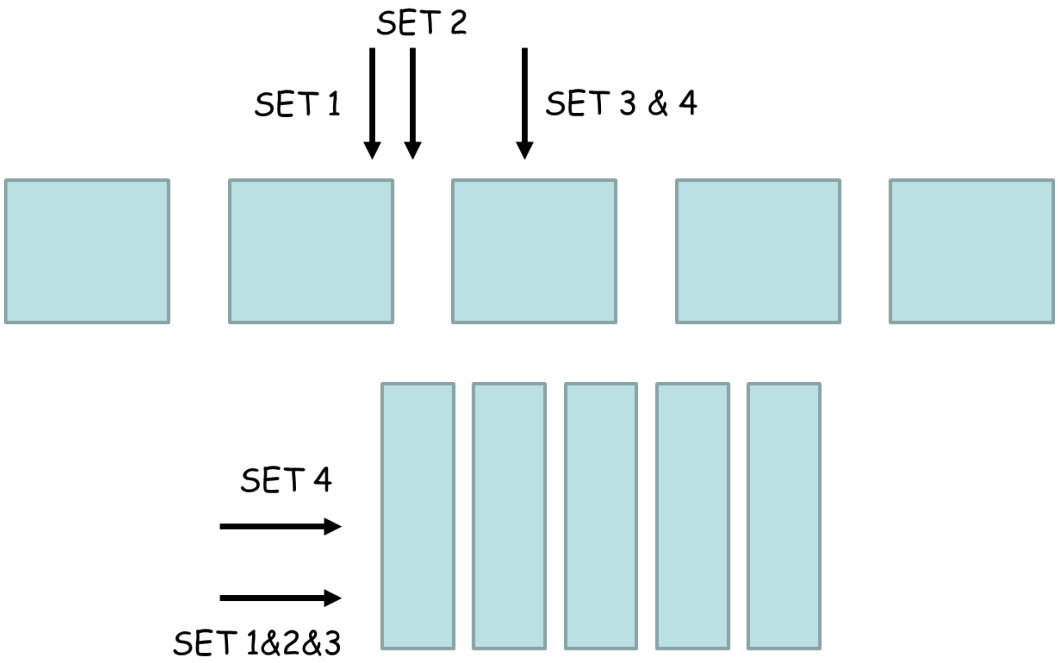

Figure 3.9: Different impact points of different data collections, on top side there is the first layer top-view, bottom side is a scrach of lateral view (PMs on top of blocks).

3.2.4.2 Energy Reconstruction

First of all we needed to subtract background (BKG); as for the KLOE like prototype, it was measured using a events subsample where tag system has no activity. Energy cuts were individualized for each block. In fact external detectors behaved as shielding of environmental diffuse BKG for inner blocks, this means that internal blocks needed cuts less stringent than external ones. The integrated BKG on whole detector is $\sim$7 MeV, in Figure 3.10 there are reported the backgrounds for all 25 channels (the beam comes from top).

Energy calibration was done using set 4 events where only first block is over threshold (electromagnetic shower totally contained into the block). If Q_e is the total charge collected in such kind of events and E_{beam} the nominal beam energy, we can conclude that Q_e/E_{beam} is the relation between energy released and PMT response (linearity in PMT response is implied). Finally using relative PeY ratios we can calibrate all detectors.

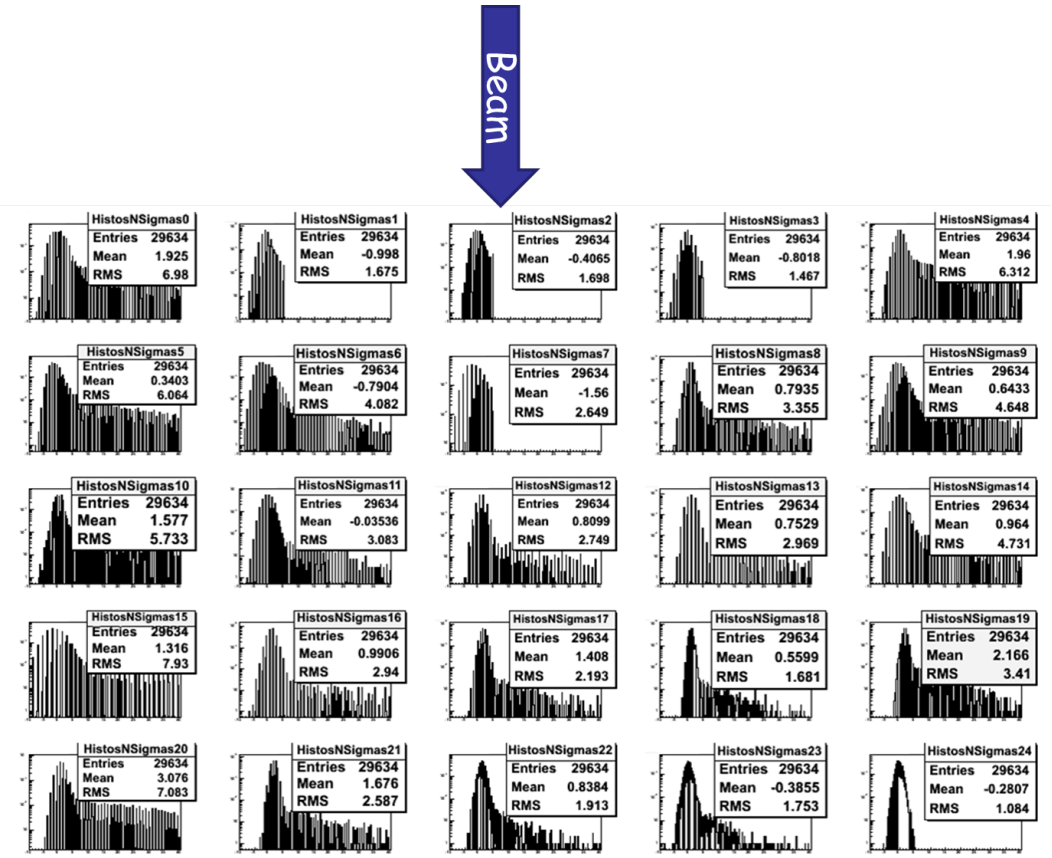

Figure 3.10: Effects on 5×5 exOPAL prototype, these are events with no tagged electron.

3.2.4.3 Energy Resolution

Once detector was calibrated we could reconstruct the energy released in whole detector. Of course we needed a clustering algorithm. We implemented a very simple one, that can be summarized in few steps:

- Define as seed the most energetic block.
- Found neighbour blocks over their own threshold, add them to the cluster.

- Iterate step 2 for new added blocks until no other over-threshold-detectors are found.

Energy resolution was evaluated for only one E_{beam} value. If $\sigma_{E_{meas}}$ is the standard deviation of measured energy, and E_{meas} is its mean value (i.e. see Figure 3.11), energy resolution is $\sigma_{E_{meas}}/E_{meas}$. Our results are:

- Set 1 and Set 2: ∼11%
- Set 3 and Set 4: ∼9.5%

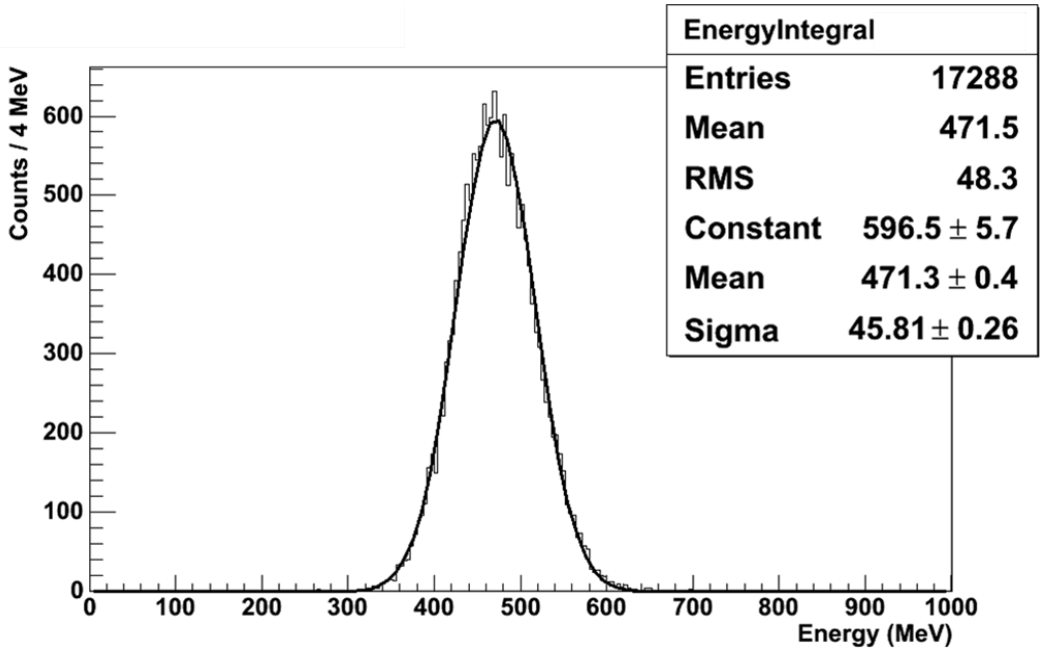

Figure 3.11: OPAL lead glass prototype energy resolution (E = 471 MeV).

3.2.4.4 Time resolution

Time resolution measurements follow the logic already adopted in Section 3.2.3.3. Corrections due to signals amplitude (time slewing) were applied to all channels (but not to tagging detectors). Also time offset was subtracted channel by channel.

Only part of Set 4 had time information.

We defined a cluster time as the weighted average of time with energy released, this in order to take into account transit time spread into PMT.

Finally what we obtained is reported in Figure 3.12. We can see that a residual ∼200 ps offset is still present. This does not affect time resolution, and we measure $\sigma_t = 591$ ps. Taking into account also the tagging system time resolution (previously measured, without slewing corrections: $\sigma_{t_{tag}} = 174$ ps) we have $\sigma_t = 565$ ps.

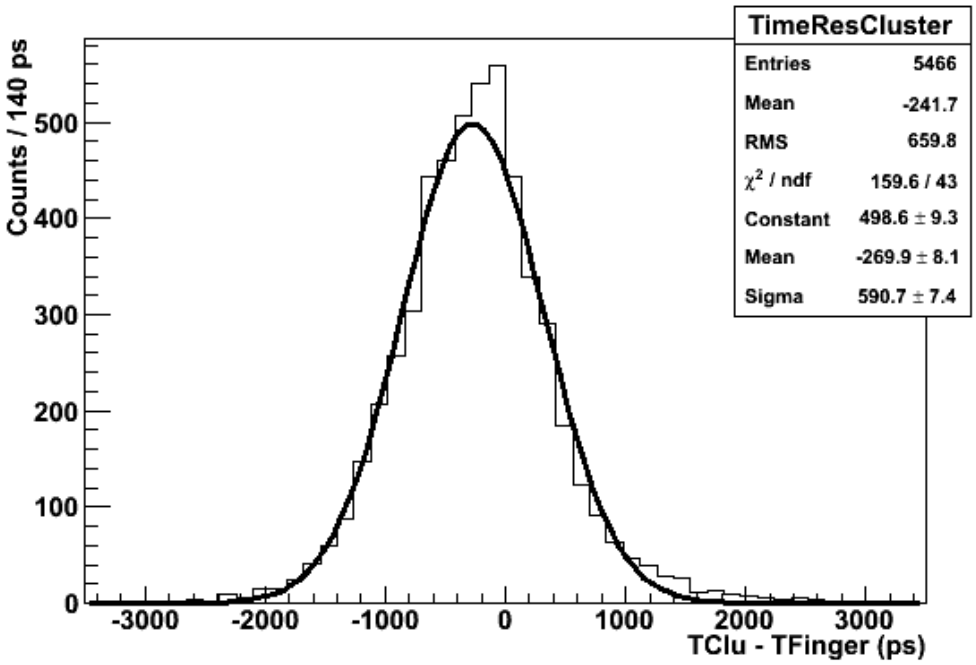

Figure 3.12: Time resolution for exOPAL solution.

3.2.4.5 Efficiency

Measurement of efficiency still follows the ideas explained in Section 3.2.3.4. Same 50 MeV cut on reconstructed energy subtracted by background was applied.

Inefficiency for both MC and data is reported in the following table:

Dataset	*Inefficiency (data)*
1	$1.0^{+1.8}_{-0.7}\times10^{-4}$
2	$<1.5\times10^{-5}$ 90% CL
3	$4.1^{+7.1}_{-2.6}\times10^{-5}$
4	$4.4^{+7.6}_{-2.8}\times10^{-5}$

A Monte Carlo simulation (Figure 3.14) was developed and in Figure 3.13 results are compared with measurements.

3.2.5 Conclusions

All prototype we tested fulfill the experiment requirements. The KLOE like prototype has shown the best performances. ButFor what concerns CKM solution data analysis was limited to efficiency measurement.

Having a large amount of exOPAL blocks available we chose this as our baseline solution.

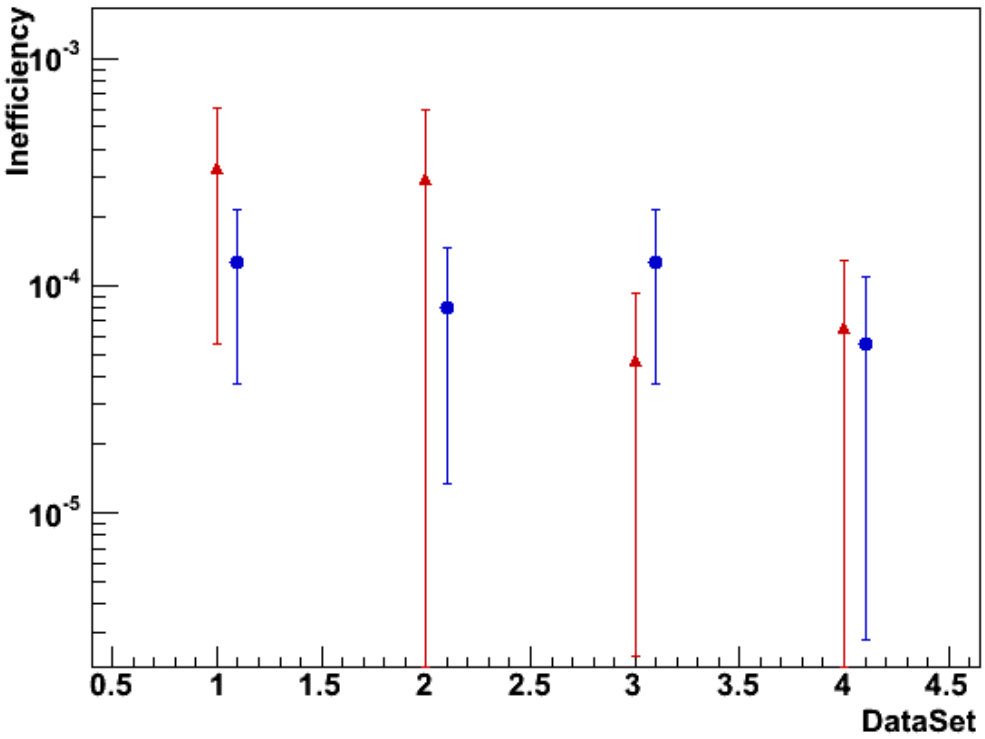

Figure 3.13: Comparison between data (in red) and Monte Carlo (in blue) for inefficiency of 5×5 OPAL prototype, different data sets are compared.

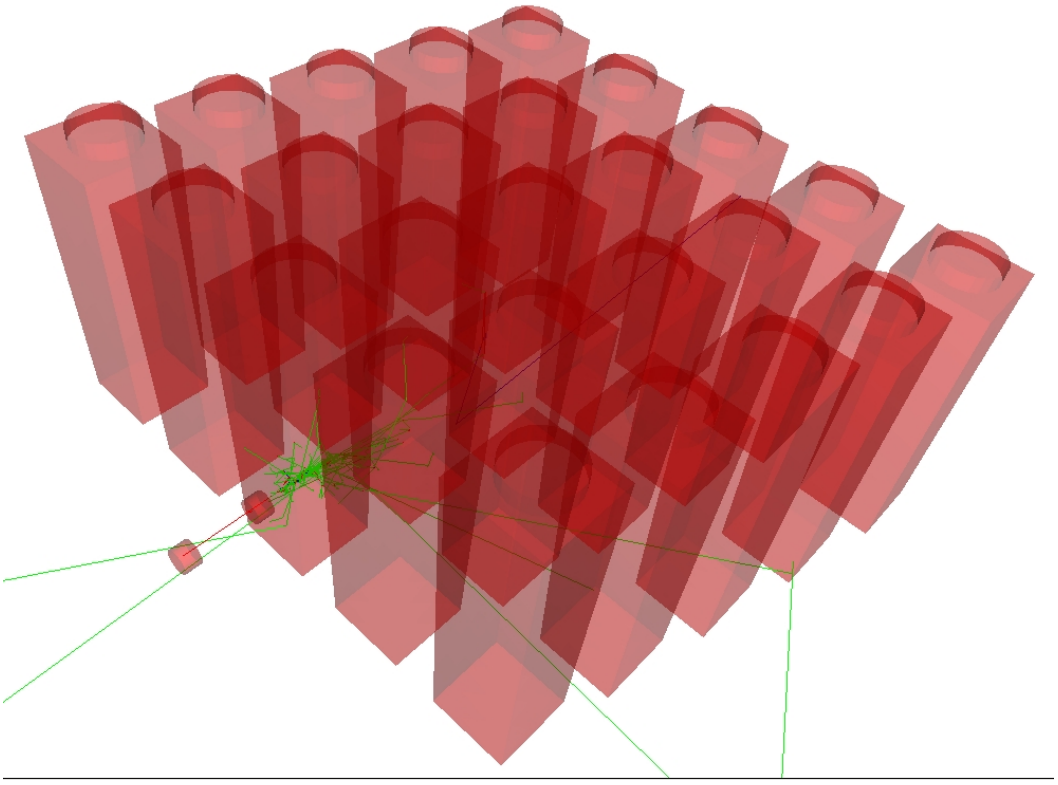

Figure 3.14: An electron event of prototype simulation.

3.3 General layout

There are three different station sizes (see Section 3.6). However basic design is always the same. The basic building blocks of these detectors are lead glass crystals with attached PMTs from the former OPAL electromagnetic calorimeter. Basic structure is made by four crystal detectors mounted on a common support structure forming an azimuthal segment (Figure 3.23). Inside the vacuum tube the azimuthal segments are assembled to form a complete ring of lead glass blocks. Each LAV station is made up of 4 or 5 rings (depends on its Z position), which are staggered in azimuth providing complete hermeticity of at least three blocks in the longitudinal direction. All the counters in a complete ring of lead glass lie in one plane that is perpendicular to the beam line, with all the PMTs on the outside of the ring.

To construct all LAV stations we need ∼2500 blocks.

3.3.1 Basic block

Each lead glass block, from the former OPAL experiment, has the shape of a truncated prism of Schott SF57 lead glass [6]. The blocks are available with different shapes and dimensions (with minimal variations between different types). The block length is always 370 mm. One of the (almost) square faces of the lead glass has a 1 cm-thick steel flange glued to it (Figure 3.15). This flange has four threaded holes for fixing the counter to the support bracket, one for the connection of a calibration optical fiber, and a central large hole for the passage of a cylindrical light guide for light collection. The light guide is a cylinder of SF57 lead glass with a diameter of 73 mm and a height of 60 mm. It is glued to the lead glass block and, at the other end, to a Hamamatsu R2238 photomultiplier. An external mu-metal shield, enclosing the guide and the PM, is glued to the steel flange.

Figure 3.15: Steel flange with support bracket.

The photomultiplier pins are directly soldered to the standard Hamamatsu divider for the R2238 tube mounted on a round printed circuit board. HV and signal cables are made of Teflon insulated RG316 cable, with a length varying from 4.5 to 6.2 m (depending on the ring to be built). The HV ground connection on the

divider is decoupled from the signal ground by a 10 KΩ resistor in series. On the side opposite to the PMT, the signal cable has a mini coax connector (SOURIAU type RMDXK10D28), while the HV cable has a Burndy pin (type RM24M-9K) on the voltage wire and a faston connection on the ground.

3.3.1.1 Block preliminary commissioning

In the chosen design partial dismount of our apparatus is a very time-consuming operation, and a single block cannot be dismounted without dismounting all former layers. This means that a meticulous block commissioning was needed. Moreover in February 2008 there was a flood event that compromised the blocks usefulness itself. We needed to recover these blocks. BELFOR was chosen as the firm responsible for recovering.

Before flood event blocks were arranged into the boxes in two layers, Top (TL) and Bottom (BL). The water level was such to touch directly only the BL.

In the following we will first describe the recovery procedure implemented and the tests used for checking the procedure itself; then we will focus on the problems found during the work, and at last, we shall describe and analyze these problems.

3.4 Cleaning and test procedures

As already discussed the flood interested only the BL. So we begin recovering this block sample.

The recovery procedure was fixed in agreement with BELFOR technicians.

3.4.1 Clean Procedure

Cleaning procedure:

1. the HV divider is removed from PM and the two parts are treated separately,
   (a) the block is unwrapped and the glue (used to fix the wrapping on the block) removed using n-propanolol, after that the block is re wrapped with the same cover; in some cases we observed a chemical reaction between glass and wrapping; after an optical cleaning with Opaline the wrapping was changed,
   (b) divider cleaning procedure:
      i. bathe the divider in n-propanol for $1-2$ days in order to dissolve the protective layer, that avoid accidental discharges or direct contact with operators,
      ii. remove mechanically, with a paintbrush, the protective layer residuals,

iii. if after the bath the divider still shows traces of dust on the electronics, a special electronic cleaner (EC12[1]) is used and the dust is removed by a paintbrush,

iv. the divider is dried using an oven at 50°C for 2 days,

2. the last operation is the divider welding and the cabling.

3.4.2 Test Procedure

Our test was developed in order to verify the integrity and the quality of each block after cleaning.

Electrical and optical tests were done using a black box (see Figure 3.16). The box could receive four blocks. One of these blocks was permanently into the box in order to provide reference measurements.

Each block was tested using the following procedure:

1. impedances measurement: HV ground-data ground (requirement: 1 kΩ), HV-HV ground (requirement: 3.5 MΩ) and data-data ground (requirement: 50 kΩ),

2. blocks are put into the box;

3. 1.5 kV test: check the block stability at its maximum allowed voltage, the current (requirement: 444±1 μA), the rate (requirement: less than 4 kHz) and checks at scope are done,

4. 0.9 kV test: the noise level is measured using two quality check: the peak to peak value with 0 threshold trigger level (requirement: less than 2 mV) and the minimum value triggered (requirement: less than -2.5 mV) by noise,

5. 1.2 kV test: this HV value is, almost, the HV value that we'll use during the normal operational life, we did several tests:

   (a) response to cosmic rays is registered using signal fall and rise time,

   (b) the rate is measured with a discriminator threshold of -7 mV,

3.4.3 Problems Found

Two main problems have been found:

1. Broken and damaged blocks,

2. Discharging blocks.

These two categories were carefully studied in order to clarify the source of the problems.

[1]Composition: Water, Surfactant, Aliphatic Amine, Glycoether, Complexing Agent, Antioxidation Protection Inhibitor, Lime Essence, coloring.

Figure 3.16: Black box used to test lead glass blocks.

3.4.3.1 Broken and Damaged Glasses

Broken glasses were not a negligible percentage (∼15%). The damage is localized near the contact surface between the glass and the iron flange (glued together).

Two different kind of damages were found:

- **Broken:** the glass shows an evident fracture near the flange, the structural efficiency is seriously compromised,
- **Damaged:** the glass is not clearly broken but the surface between flange and glass shows a thin crack.

for an example of both see Figure 3.17.

All the categories are the consequence of a mechanical stress, this kind of stress may derive from a thermal shock or a not suitable handling during OPAL dismounting.

Up to now all the blocks from BL have been checked and we can give an almost definitive statistic. Moreover in order to understand the source of these problems, we inspect also a sample of TL blocks in two different periods. From data is clear that we can exclude as cause of damages the *direct contact with water*. Moreover we cannot exclude that the accident itself is the cause of damages, in fact we have no samples of blocks that were not in the hall during the flood (in reality we have

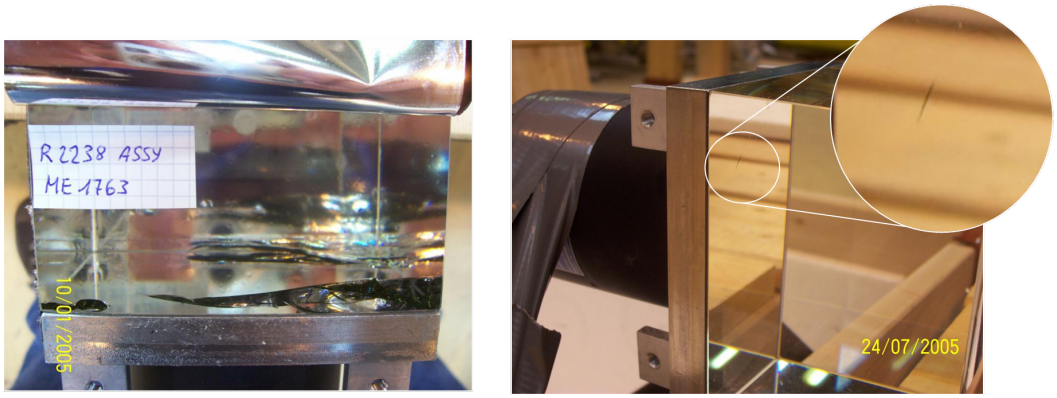

Figure 3.17: Examples of Broken (left) and Damaged blocks (right).

such sample of 40 blocks but it was damaged during a different event). Therefore no comparison is available.

Another hypothesis is that damages were caused during the OPAL dismounting operations. The summary of these tests is reported in table below; percentage are given only for BL because, up to now, is the only exhausted sample.

Sample	*Passed*	*On Hold*	*Broken+Damaged Blocks*	*Total processed*
BL	1358 (83.8%*)	262(16.2%*)	163 (9.1%**)	1783
TL	302	48	62	412

* out of [Passed + On Hold].
** out of Total processed.

3.4.3.2 Discharges

Out of broken glasses we found also a more serious problem that involve a large amount of blocks ($\sim 15\%$): *discharges*.

As described in Section 3.4 the first step during the test was to supply PMs with 1.5 kV (maximum high voltage value allowed by Hamamatsu). During this operation the operator checks the current absorbed, the signal rate (with a threshold of -7 mV) and give a signal visual evaluation at scope, moreover the rate at 1.2 kV has been measured (with same threshold of 1.5 kV).

We found blocks with:

1. a very high rate (5 kHz) at 1.5 kV,
2. and/or an abnormal current (444±1 A) at 1.5 kV,
3. a high rate also at 1.2 kV (50Hz).

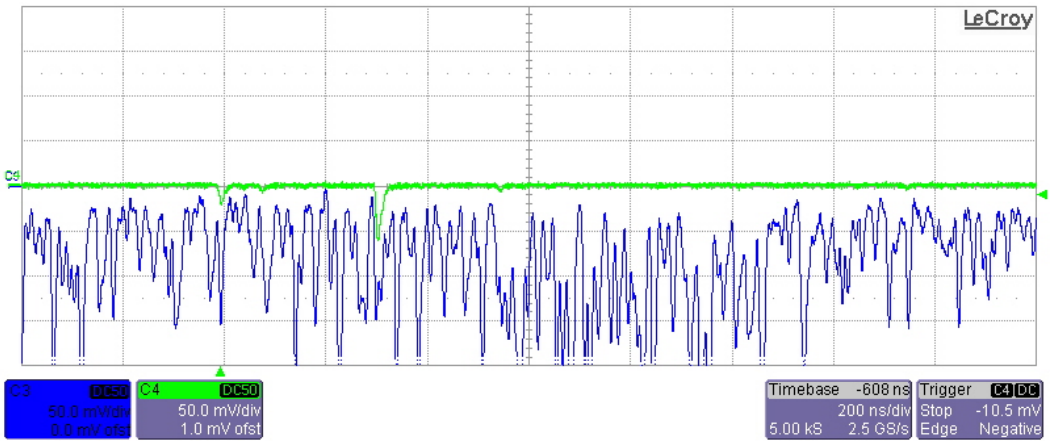

Figure 3.18: Example of normal (green) and discharging blocks (blue).

Examples of normal and discharging blocks signals are reported in Figure 3.18.

This thorny argument was treated in a very careful way. It opened many questions, and a lot of tests have been developed in order to understand the problem source.

The blocks showing that kind of behavior were called On Hold, because we are not able to say if they could be usable in the experiment.

For further discussion is important to say that a relatively small sample of blocks (40) was sent in Naples before the flood and none of them show any kind of discharge problem.

Here are presented all tests done and relative conclusions:

1. In order to understand the origin of discharges we chose a problematic block and developed some tests involving the divider:

   - all the capacitors were changed with new ones,
   - the divider was replaced with one coming from a normal block.

   The result was that the blocks under study still continued to show discharges.

2. In order to be sure that the source of discharges was not the cleaning procedure, we chose a sample of 72 top layer blocks (3 boxes) that were tested 2 times:

   - the first test was developed using a temporary cabling without cleaning the divider,
   - in a second time all the blocks were cleaned with the standard procedure and tested again.

   The result was:

	Broken	*Passed*	*On Hold*
Before	8	52	12
After	8	54	10

it shows that the cleaning procedure is not a possible discharge cause. Moreover we can say that the 2 blocks that move from Passed to OnHold were on the acceptance value edges.

3. Also a sample of PMs never used alone (not glued to the glass) has been tested. The result shows again the same percentage of discharges.

4. Now is clear that the discharge source is the PM and not the divider. A possible cause of this discharges is the humidity that penetrate the plastic PM protection. A first attempt was to study the water residuals that could be a cause of some short circuit between pins. The test was done by BELFOR putting 3 PMTs, one at time, inside a vacuum chamber and measuring the out gassing. This gave us the certainty that no more water was inside. The result was that no PM was recovered by this procedure.

3.4.3.3 Conclusions

Unfortunately we still have no explanations about discharges. Any cause or possible solution were found.

However we trust that the problem was due to flood. This assertion can be motivated as follow. We pointed our attention on the 40 blocks sent in Naples before flood happens (as already said we a different accident was the cause of mechanical damages but electronics and PMT was not involved). This means that these are the only sample that was not flooded. We tested, with the usual procedure, also these blocks and none was found discharging.

Now known the percentage of discharging blocks (16.2%) we can conclude that the probability to observe 0 discharging blocks on a sample of 40 blocks is $\sim 8.5 \times 10^{-4}$. This very small probability suggests that the two samples are not statistically compatible. The only major event that distinguish the samples is the flood and the following handling, thus we can conclude that it was, in a way we do not know, the cause of discharges.

3.5 LAV Station realization

The assembling of LAV stations started in March 2009. Our first module is called ANTI-A1 is shown in Figure 3.19, it is intended as a prototype to study. We would like to test the read-out electronics, mechanical structure and assembling procedure. However it will be used (after some modifications) also as one LAV station.

Into the following subsections we describe briefly the construction procedure, from blocks characterization to final assembly.

Figure 3.19: First LAV station called ANTI-A1.

3.5.1 Gain curve measurement and equalization

All block are tested before mounting. An automatic measurement system was developed. For each block the gain curve and the Photoelectron Yield (PeY[2]) are measured . There are several benefits from the knowledge of these two quantities. First of all we can define selection criteria to discard blocks with a low gain or low PeY. Moreover we can define "a priori" the working voltage supply for all the blocks in order to have a response equalization (same response for same energy deposit). Operational voltage supply can be adjusted it in order to correct possible variations of block response that could occur during the running period.

3.5.1.1 Setup and test procedure

A light tight box was designed and build at INFN Napoli, and used for the test (see Figure 3.20). The box houses 20 blocks in 4 columns and 5 raws. First and last blocks of each column are fixed are used to define the trigger for cosmic rays. The remaining 12 crystals are the sample to be characterized. Each block is inserted from the front side using drawers. The light from a LED is distributed to all the blocks using a 14 optical fiber bundle. Each fiber can inject light pulses to the PMT using the small "inspection" window of the wrapping on opposite PMT side (see Section 3.3.1). The LED temperature is stabilized at $\sim$0.1°C level by a Peltier cell,

[2]PeY is defined as the number of photoelectrons per MeV released by a MIP.

and can spread in a range of ±5°C around the room temperature. The light pulses amplitude can be modified. The ratio between the maximum and least amount of light is about 25.

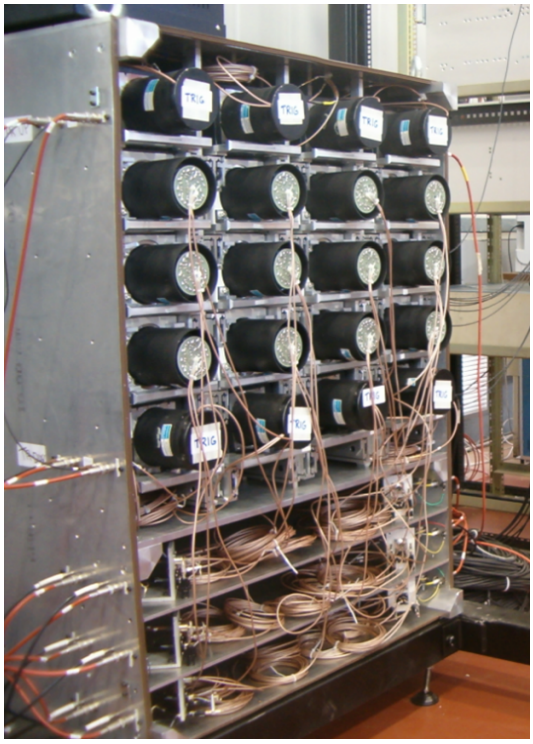

Figure 3.20: Blocks test station.

The system is controlled via PC using LabView. The HV for each LG is supplied by a SY127 CAEN HV crate, controlled by a VME module (A200). Signals are acquired by a charge integrating ADC (CAEN V792). The light pulser is controlled by a serial line.

The procedure can be summarized in three steps:

1. *Gain curve measurement*: for different HV the gain is measured using the LED. A gain curve G vs V is fitted.

2. *PeY measurement*: each block is set to a fixed gain using the G vs V relation. A cosmic run is performed and the mean value of the response is measured, that corresponds to a known mean energy release of ∼77 MeV. A first estimation of the PeY is then available. As further check a second PeY measurement is made with a new run at a different gain value.

3. *Equalization runs*: from the G vs V relation and the two PeY estimations we can calculate the HV for each block in order to obtain an equal response from each detector. Defined the response R_{eq}, a cosmic run is performed to measure

the actual response R_1. To correct for the small (2%) systematic discrepancy observed by measurement, a correction to the bias voltage is evaluated starting from the difference R_{eq} - R_1 and the G vs V relation. A second cosmic run is then performed to measure the response.

Let now describe with more details the gain and PeY measurements.

3.5.1.2 Gain curve measurement

The gain G of a PMT can be measured using a sample of light pulses with the same amplitude [14].

If R is the measured response, and $< R >$ is its mean value, and σ_R its standard deviation, we can relate all these quantities with the gain G:

$$\sigma_R^2 =< R > \cdot G \cdot (1 + \delta_{SER}^2) \tag{3.2}$$

where the δ_{SER}^2 term is the Single Electron Response (SER) fluctuation contribution, defined as:

$$\delta_{SER} = \left.\frac{\sigma_R}{< R >}\right|_{n_{pe}=1} \tag{3.3}$$

This term is gain and PMT structure dependent.

The δ_{SER}^2 contribution is not negligible, it can be of the order of 10%, and must be taken in account. With good approximation, δ_{SER} is:

$$\delta_{SER} = G^{\frac{-1}{N}} \left[\frac{(\prod k_i)^{\frac{1}{N}}}{k_1}\right]^{\alpha} \tag{3.4}$$

where N is the number of dynodes in the PMT, K_i is the fraction of the voltage applied on the i^{th} dynode, and α is a parameter, usually between 0.6 and 0.7, that we fixed at 0.6.

For each voltage we measure R and σ_R for a sample of N_P (typically $N_P = 10^4$) light pulses with the same amplitude. We repeat the procedure for different light amplitudes. Than we perform a minimum square fit using the relation 3.2.

The gain measure is performed for different HV values, typically from 1150 V and 1350 V with steps of 50 V. Once obtained the gain measure for different voltages supply values a G vs V ($G(V)$) curve can be fitted. The function $G(V)$ we use to fit is:

$$G = aV^{(b+cV)} \tag{3.5}$$

instead of the "standard" relation $G(V) = aV^b$. As a matter of fact the first relation gives better chi square probability with respect to the second one. An example output from acquisition calibration system is reported in Figure 3.21.

3.5.1.3 PeY measurement

The PeY is defined as the number of photoelectrons per MeV of energy released by a MIP crossing the device, this means that we have to know the amount of energy

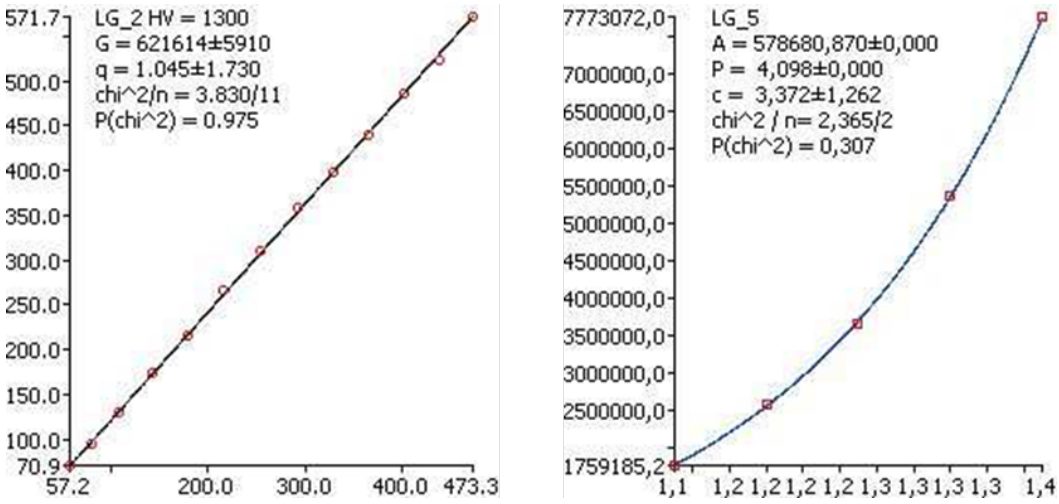

Figure 3.21: Output from calibration procedure. Signal variance versus signal mean value (left side). Gain versus voltage (right side).

released. It depends mainly o the photon yield of the crystal, the photon collection efficiency and the photocathode quantum efficiency. Previous measurements have shown that block response does not depend by the distance of the track from the PMT. This allows us to use the simple trigger configuration previously described, where all tracks are collected, independently from the impact point position. We evaluated the PeY in the following way: the total charge Q measured when a MIP crosses the detector is:

$$Q = G \times N_{pe} \times q_e = G \times E \times PeY \times q_e \tag{3.6}$$

where G is the PMT gain, q_e is the electron charge in Coulomb and E is the mean energy released by the MIP, that is of the order of 77 MeV for a particle impinging orthogonally the crystal.

For each crystal we evaluated, from the previously measured gain function (see Section 3.5.1.2), the voltage V corresponding to a gain of 10^6. Then a so called "cosmic run" is performed: 10^4 crossing MIPs are collected for each detector. For a typical trigger rate of 0.5 Hz, this means ∼6h of run. An automatic procedure performs a gaussian fit to the central zone of the MIP peak and the Q value is estimated. A second cosmic run, with a working point corresponding to 0.9×10^6 gain, is then performed. This allows the determination of a second independent PeY measurement, that is compared to the first as cross-check.

3.5.1.4 Equalization run

From $G(V)$ function and the PeY value we can estimate the working point V_{eq} for each LG in order to obtain the same response Q for the same energy released. Fixing an arbitrary value of $Q_R = 4.5$ pC we set the block voltage to V_{eq1} and we perform

a first cosmic run collecting $N_E = 10^4$ events. The response Q_{eq1} is than computed by a gaussian fit. To obtain a better result (see next chapter) a second cosmic run is performed. A new bias voltage V_{eq2} is evaluated in the following way. The difference between the expected and the measured response $\Delta Q = Q_R$ - Q_{eq1} corresponds to a gain variation Δ G = Δ Q $\times$ E $\times$ PeY $\times$ q_e. From the $G(V)$ relation the ΔV correction to apply to the first voltage can be computed.

Of course more accurate equalization could be reached continuing this iterative procedure but we observe no significant improvements.

In Figure 3.22 are reported the equalization for a sample of blocks. We can observe the improvement passing from fist to second equalization run. Neglecting the two blocks for which the procedure, clearly, fails we have an equalization better than 2%.

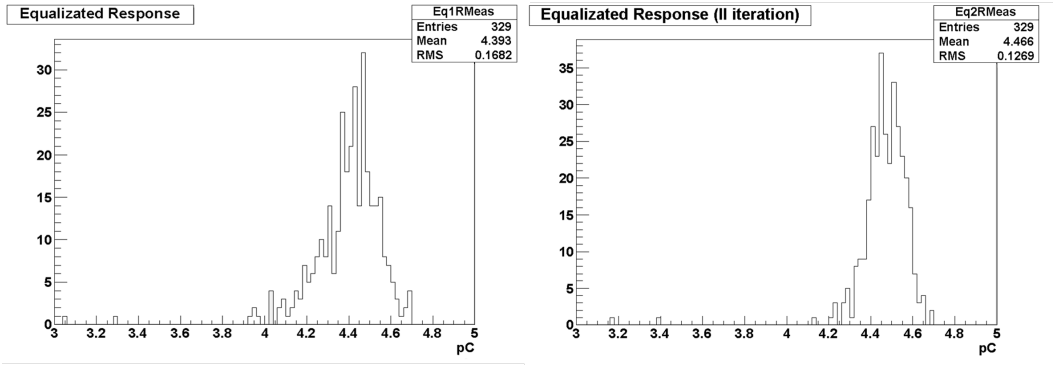

Figure 3.22: Iterative procedure for blocks equalization (2 steps).

3.6 Module construction

All modules will be built at Laboratori Nazionali di Frascati (LNF). In following discussion we will refer to the cylindrical shaped vessel will contain the blocks simply as "cylinder". The assembly operations can be grouped into three phases:

1. Preparation and installation of detectors into the cylinder
2. Rotation and electrical and vacuum testing
3. Packing for shipping

The number of blocks needed by each stations, and outer radius, are reported into following table:

Station	*Number of blocks*	Outer radius (mm)
1→5	160	1064
6→8	240	1544
9→11	240	1944
12	256	2144

3.7 Preparation and installation of the blocks into the cylinder

To avoid accidentals detach of glass from their steel flange, reinforcement plates are glued across the junction between the glass and the steel flange on the four crystal sides. The glue used is DB490 by 3M, a two-component epoxy resin. This gluing procedure have been proved to sustain stresses as high as 40 times the crystal weight in the vertical direction.

After reinforcement, the detectors are wrapped to increase light collection. Wrapping is not required to be light-tight, since detectors will work in complete darkness. The wrapping material consists of laser-precut sheets of DuPont 4173D-Tyvek©, chosen because of its high load resistance and its optical properties. The Tyvek© is folded over a block mock-up and the folded ends soldered together to give it the correct shape. The formed wrapping has holes used to be anchored by screws to the holes on the flange at the top.

In groups of four, the detectors are then mounted in the support brackets (denoted as "bananas"), mainly made by two aluminum plates connected to each other by cylindrical and square spacers. The plates have two circular and one square holes per side, guaranteeing access for tightening the support screws to the vessel and for mounting a suitable lifting tool. Crystals are connected to a banana by stainless steel screws. For each lead glass block the high voltage, the signal cable are routed and fixed into the mechanical structure. A completed banana is shown in Figure 3.23. The assembly is then moved using a cart and a special lifting tool which uses the central hole of the banana for the connection and has a plate underneath the crystals as a protection to avoid damage during handling.

Figure 3.23: A complete banana.

Since the entire detector structure must operate in vacuum, all the screws used in the mounting and installation either are traversed by an axial hole to avoid virtual leaks during pumping; moreover all the screws and the banana components are cleaned in an ultrasound bath.

Bananas are mounted into cylinder that will assure the vacuum tightness of the experiment. During the installation the cylinder is placed with its axis in the vertical direction. Now banana installation can start (see Figure 3.24). The banana is lowered into the cylinder. Immediately afterwards, the HV and data cables are fixed to a grid and routed towards the portholes for cable exit. One day is needed to mount and cable one layer of "bananas". Before mounting the subsequent layer, the cosmic ray signal of each lead glass at a voltage of 1.2 KV is checked using an oscilloscope.

The previous operations are repeated for each layer; once the mounting and cabling is completed.

The final module is shown in Figure 3.25.

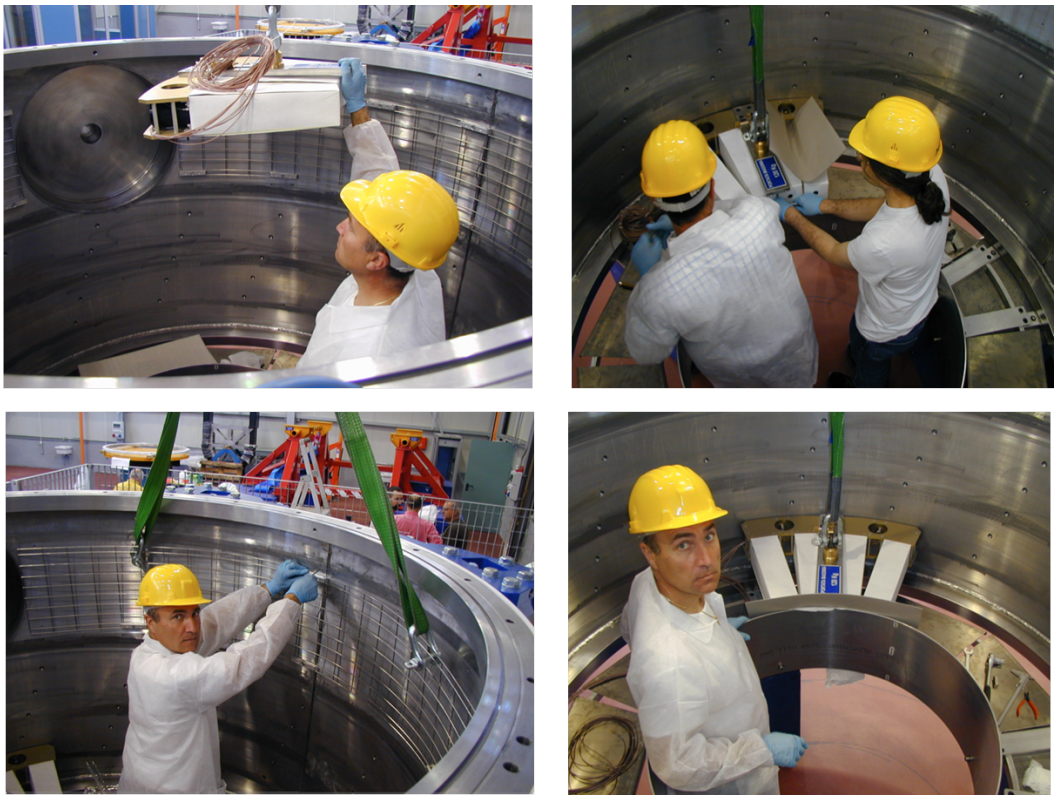

Figure 3.24: Installation phases: 1) a banana is lowering into cylinder, 2) mounting banana on cylinder, 3) routing cables on grid, 4) first banana correctly installed.

Figure 3.25: First LAV station.

3.7.1 Readout electronics

Due to relatively mild requests on energy measurements and in order to reduce costs we decided to implement a Front End Electronics (FEE) based on Time over Threshold (ToT) technique.

ToT means to measure the time that a signal is over a given threshold. We developed a custom project designed to convert analogue signals from PMT into standard LVDS digital signals.

A basic scheme for one channel is reported in Figure 3.26. The analog signal is amplified, clamped, split and send to two separated comparators; clamping stage was necessary in order to protect the amplification circuitry by large signals, given the large dynamical range of the expected signals in one block. In fact signals can vary from tens of mV for a MIP to few V for high energy releases from electromagnetic showers. Each comparator compares the analog signal with a programmable threshold and produce an LVDS output signal whose width is equal to the time the analog signal is above threshold. The LVDS signal is then transmitted to a TDC to measure its width that is related to the deposited charge. The functional relation between ToT and charge is logarithmic and therefore saturates for high charge values decreasing the sensitivity of the reconstruction algorithm. The use of a second threshold crossing the top part of the PMT signal, where the slope is steeper, allows to extend the range of sensitivity.

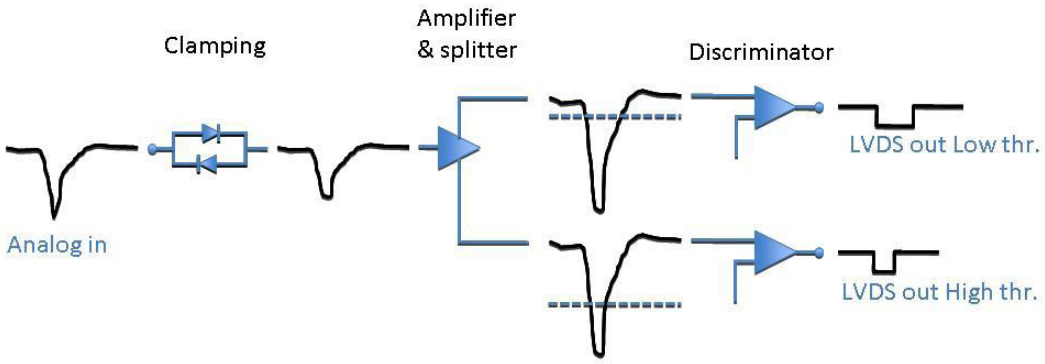

Figure 3.26: Basic scheme of one FEE channel.

3.8 ANTI-A1 test beam

ANTI-A1 prototype has been tested at CERN in October 2009.

All 160 channels were provided of HV but only half were instrumented with readout prototype electronics (see Figure 3.28).

This test was developed in order to validate ToT as readout method. In particular, using a muon beam, we wanted to validate the calibration method implemented during module construction, and compare QDC and TDC techniques.

We installed the ANTI-A1 in K12 north area beam line (Figure 3.27).

Trigger is provided by OR of first crystals layer.

In Figure 3.28 a detector front view is reported. The two spots indicate the impact position of the muon beam.

An on line monitor (OnM) was developed for this test. The on line monitor provided us some useful information like, beam position on detector and channels response. An simplified image representing the instrumented half detector in a plain-top view was used . Event by event each block change color (red intensity scale) proportionally to TDC or QDC counts. An example of on line monitor is reported in Figure 3.29, these two screen shots show the detector response to a muon beam interacting with detectors on points reported in Figure 3.28. In one case an ADC channel inversion has been found.

3.8.1 Results

3.8.1.1 Calibration validation and TDC vs QDC response

We used dedicated muon run in order to validate the off line calibration obtained using cosmic rays. A block traversed by a MIP incident orthogonally to the rectangular face have a mean response of 4.5 pC (that correspond to 45 ADC counts).

In Figure 3.30 we report results from test beam of all blocks (remember that first layer is used as trigger, this imply that for these blocks the measurement is biased).

Figure 3.27: ANTI-A1 installed on K12 beam line.

Figure 3.28: ANTI-A1 front view, the two dots represent the interaction point of muon beam.

Figure 3.29: Examples of on line monitoring, color red intensity is proportional to QDC or TDC counts. On top we report detector response to a muon beam interacting on green dot of Figure 3.28, and on bottom the same but on blue dot: we can observe how in bottom figure there is an evident channel inversion.

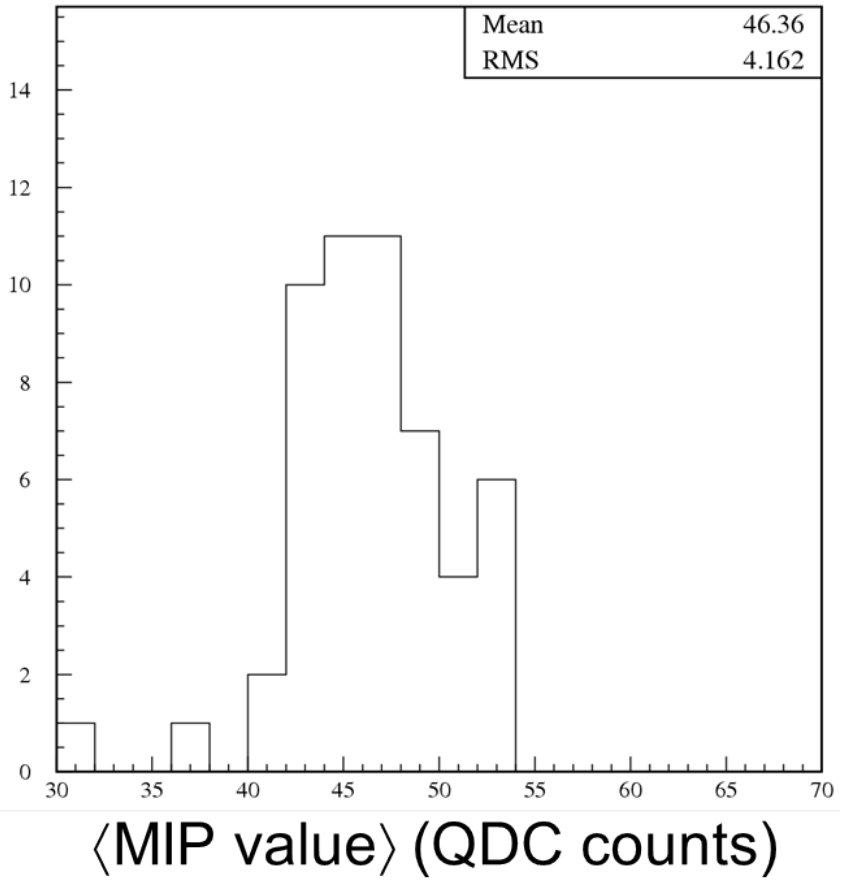

Figure 3.30: Blocks response to muons.

An other important results is the ToT validation. In order to do that we compared ToT with QDC results. In Figure 3.31 are reported the results. We can conclude that for a MIP QCD and ToT give comparable results.

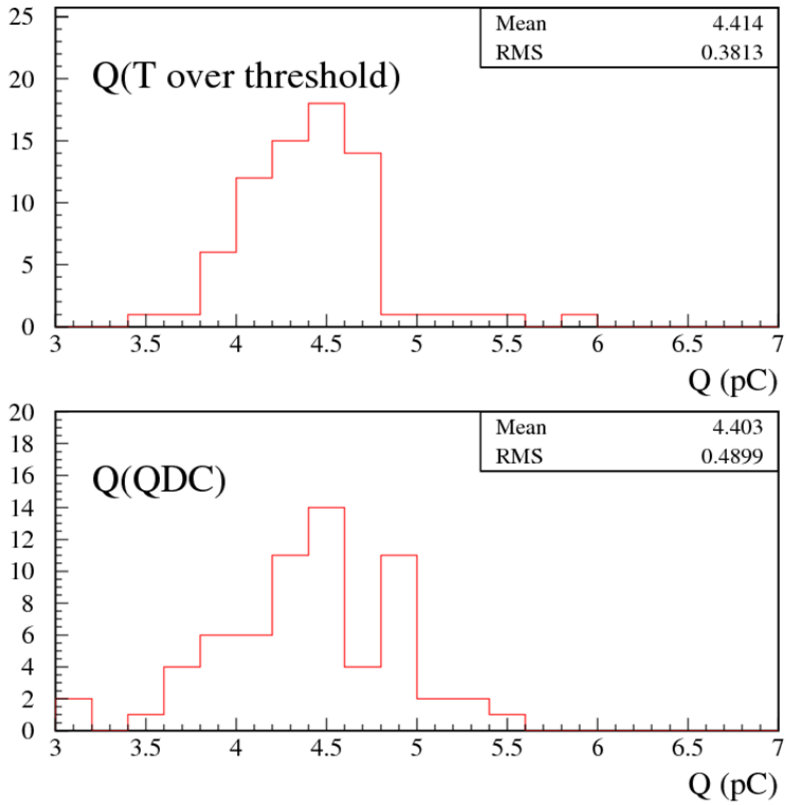

Figure 3.31: QDC (bottom) compared with ToT (top) response.

Unfortunately we found a problem due to ToT technique. Plotting QDC versus ToT (see Figure 3.32) we can observe a multivalued curve.

We explained this deviation observing plot on bottom of Figure 3.32. We have to remember that ToT technique provide logical signals proportional to the time over threshold of a given signal shape. Unfortunately ToT circuit we have, is not able to distinguish signal threshold crossing that differ by less than 5 ns. This means that ripple at the end of the signals (that are characteristic of readout divider) have the effect of artificially increase the ToT.

3.8.1.2 Time Resolution

Using a run of 2 GeV electrons we estimated time resolution using ToT. We used time differences of subsequent blocks. Slewing corrections were applied. Data before and after corrections are reported in Figure 3.33.

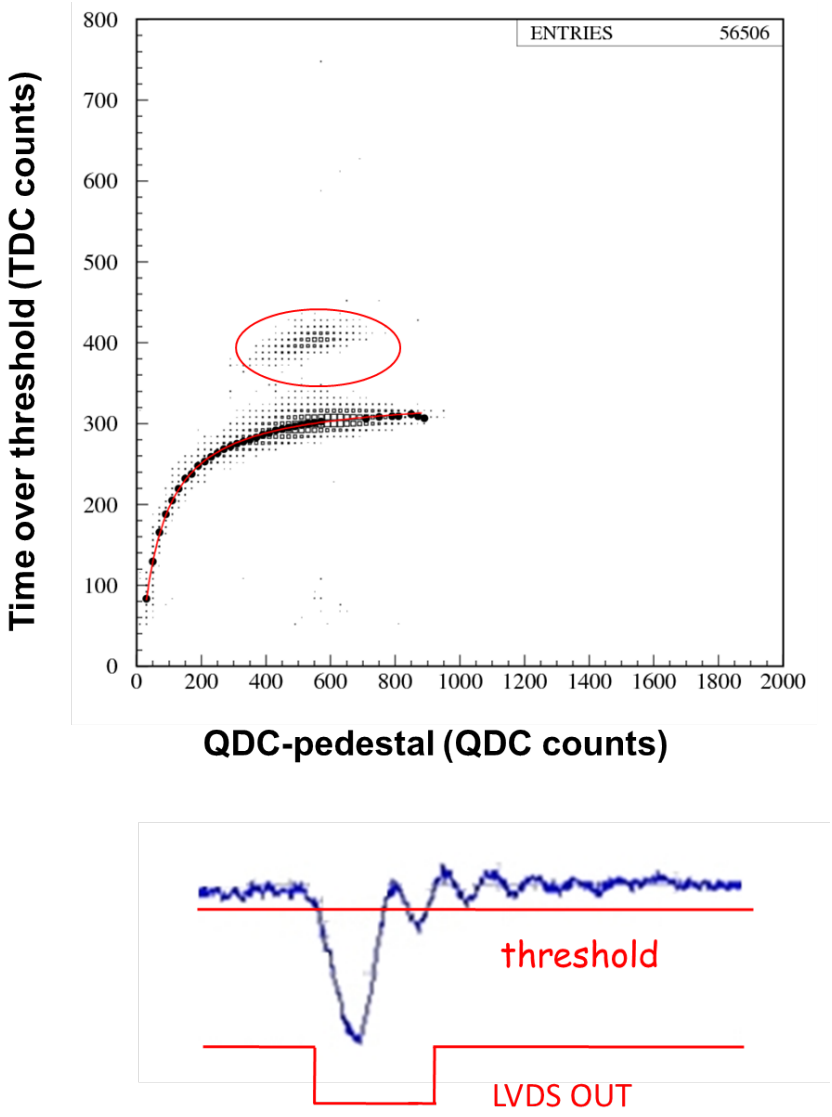

Figure 3.32: QDC versus ToT (top), we can observe a multivalued curve (red circle) due to signal ripple (bottom).

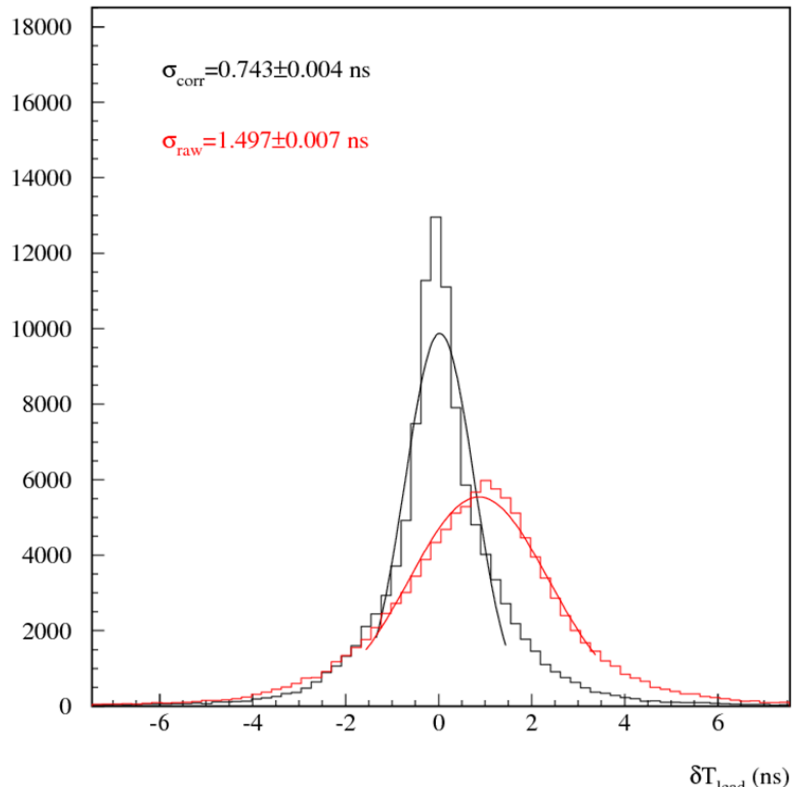

Figure 3.33: Time resolution with (black) and without (red) slewing corrections.

3.8.2 Conclusions

Results about TDC vs QDC response show how we need to find a solution in order to extend the useful signal amplitude region. Once the cause was found (see Section 3.8.1.1), the possible solutions were to increase electronics performances of reduce signal ripples. Our solution was to change dividers of all blocks. Difference between signals generated by the old and new dividers are reported in Figure 3.34

Our test was limited by this unexpected inconvenient and neither energy resolution nor linearity were measured. A new test has been performed in August 2010 using the second station constructed using upgraded hardware. Preliminary results show that problem with signal ripple seems be solved (Figure 3.35).

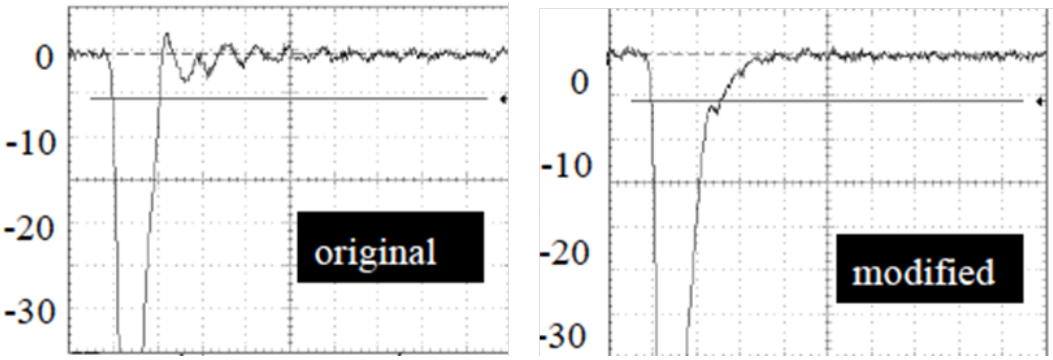

Figure 3.34: Signals from old and new divider are compared, we can stress how new solution (on the right) doesn't show no more ripple.

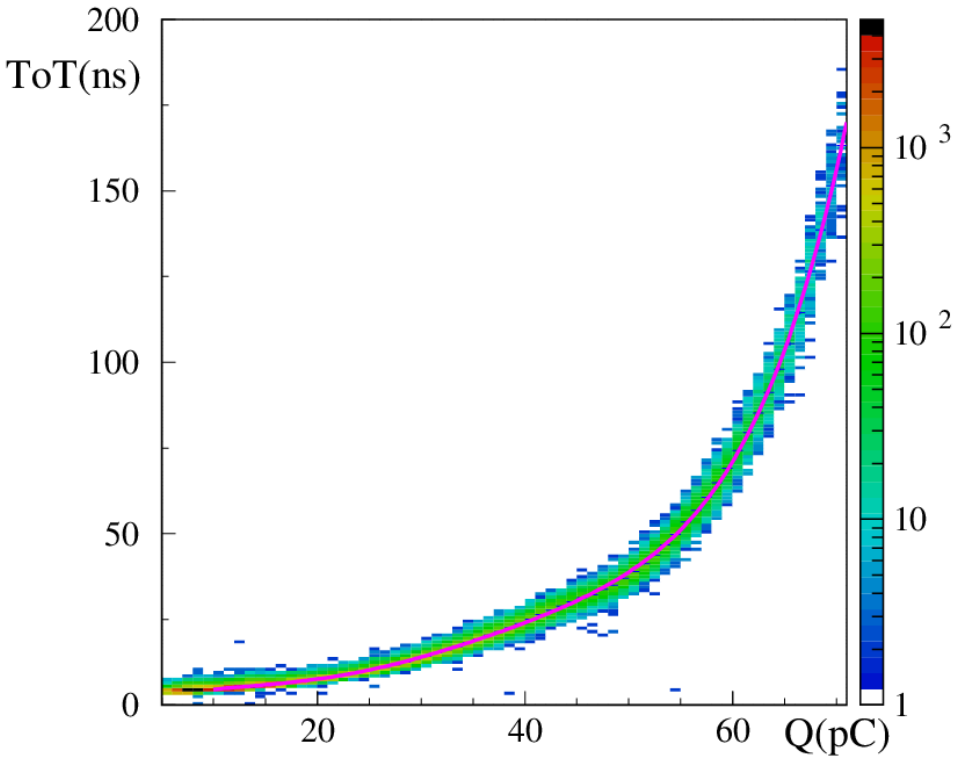

Figure 3.35: ToT versus charge obtained with new dividers and 3 GeV electrons.

Chapter 4

CHarged ANTIcounter

The CHarged ANTIcounter (CHANTI) detector is required in order to reduce critical background induced by inelastic interactions of the beam with the collimator and the Gigatracker (GTK) stations as well as to tag beam halo muons in the region immediately close to the beam. The most critical events are the ones in which the inelastic interaction takes place in the last GTK station (GTK-3). In such cases, pions or other particles produced in the interaction, if emitted at low angle, can reach the straw tracker and mimic a K decay in the fiducial region. If no other track is detected, these events can appear like a signal event, i.e. one single π^+ in the final state.

A GEANT4 simulation has shown that kaon inelastic interactions with GTK-3 happens in about $1/10^3$ cases, so that the combined rejection factors of the analysis cuts and the CHANTI veto must lead to a remaining inefficiency of 10^{-8}.

Given that it will be sensitive to the muon halo and to the inelastic interactions the expected rate of particles that release enough energy to be detected will be around 2 MHz. Even if it is not intended as a trigger veto at L0, the CHANTI must have a good time resolution ($\leq$ 2 ns) to keep the random veto rate at an acceptable level: for instance, assuming a 5 sigma (10 ns) time coincidence window with the event fine time at reconstruction level, a 2% inefficiency on the signal would be induced by CHANTI random vetoes. Although tracking capability may be not mandatory for the system, it can help in distinguishing beam halo events from inelastic interactions and in monitoring the beam halo itself very close to the beam. Last but not least, position sensitivity is useful in improving time resolution without increasing too much the granularity of the detector.

4.1 Requirements

CHANTI will work in vacuum. This means that we will not have many recovery opportunities if hardware fails. So we have to reduce components inside vacuum to the ones strictly necessary. The detector shape needs to be as precise as possible because CHANTI is very close to the beam and any interference must be avoided, is also preferred a compact geometry in order to reduce vacuum tank dimensions. Moreover our layout choice must take into account the difficulties of heat dissipation due to vacuum, and also out-gassing must be as low as possible in order not to compromise the vacuum itself.

Of course we have other constraints due to the general layout of NA62 apparatus and the beam. As for LAV in order to synchronize signals coming from CHANTI

with all the other detector and 800MHz beam time upper limit is 1ns. On the other side also dead time needs to be as small as possible, this is suggested by detector position close to the beam, and hence with high signal rate.

With these requirements in mind we can describe the CHANTI in its general layout.

4.2 General Layout

CHANTI general layout is sketched in Figure 4.1. It is composed of six stations, placed inside the vacuum tube respectively at 27-77-177-377-777-1577 mm distance from the GTK-3. The rectangular hole inside each station is 50 mm in Y and 90 mm in X due to the rectangular shape of the beam. Outer square side length is 300 mm.

For particles hitting the GTK-3 center the CHANTI covers hermetically the angular region between 34 mrad and 1.38 rad respect to the beam axis, for particles hitting one of the GTK-3 corners the coverage is hermetic between 50 mrad and 1.16 rad. This must be compared to the highest angle under which a LAV station is able to detect particles produced in the GTK-3 that is 49 mrad for particle produced at GTK-3 corner, so that LAV complements at low angles the information given by CHANTI.

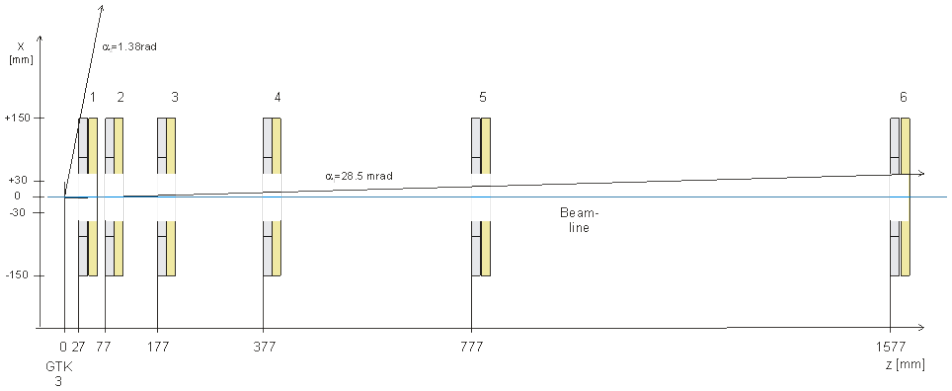

Figure 4.1: Positioning of the six CHANTI stations on the beam line (top view). The first colored line is GTK-3, the distance between GTK-3 and the first CHANTI station is 27 mm.

Each station is made up of two layers, called layer X and Y respectively. A Y(X) layer is composed of 22(24) scintillator bars arranged parallel to the X(Y) direction and individually shaped at the appropriate length (see Figure 4.2). Each layer is in the end composed by two sub-layers, made up by 10+12 (10+14) bars, and staggered by half bar. Each bar is triangularly shaped, and two staggered bars face oppositely as shown in Figure 4.3. Light is collected by means of one WLS fiber placed inside each bar and read at one side by a photodetector.

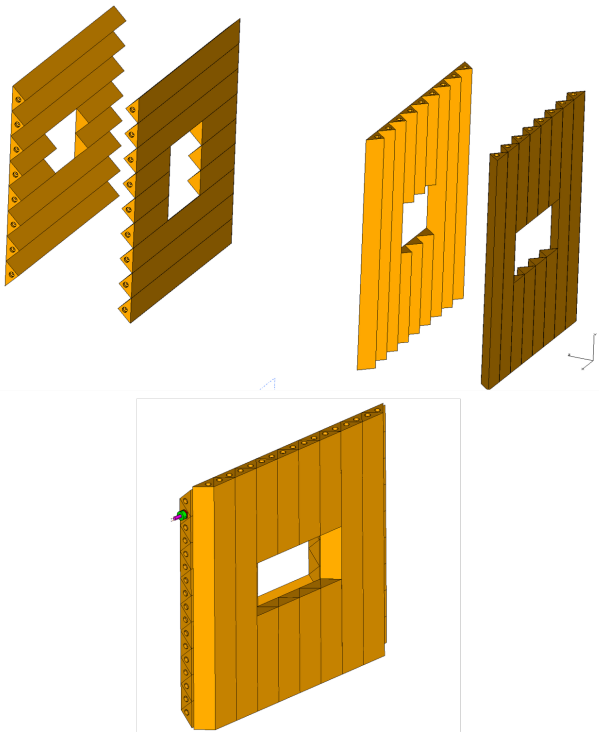

Figure 4.2: Layout of a complete CHANTI station. Top: exploded view; bottom: assembled station.

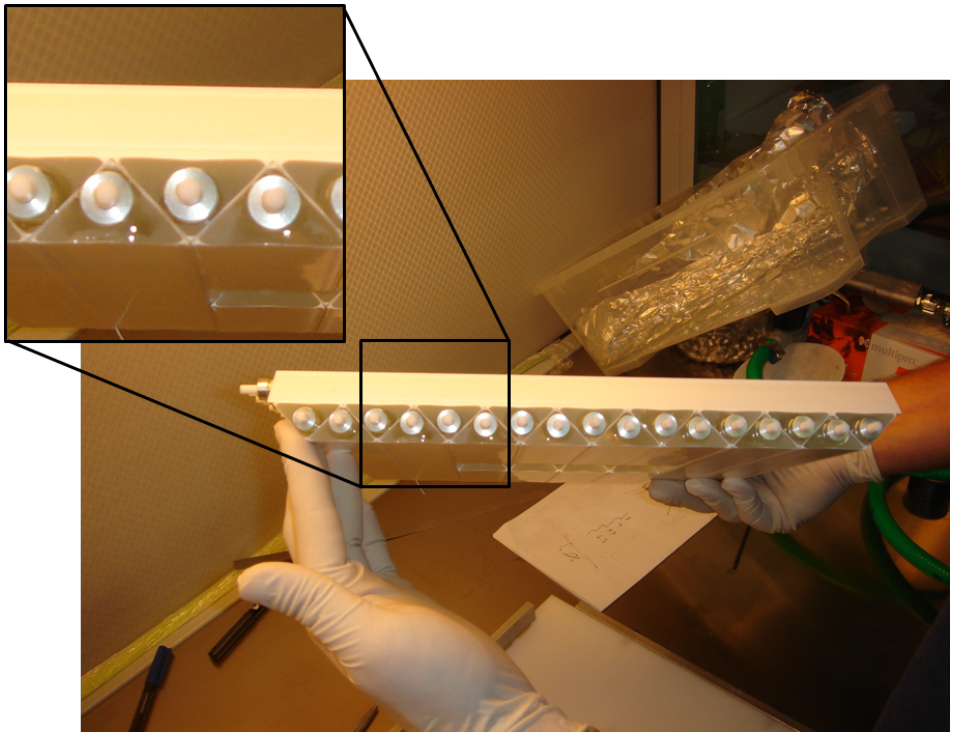

Figure 4.3: Staggering of triangular scintillator bars to form a plane.

4.3 Basic Scintillator Layout

The basic building block of the CHANTI is a scintillator bar in form of a triangular prism similar to the ones used in the D0 preshower detectors [19] and the MINERVA experiment [20]. It is produced at the NICADD-FNAL extruded scintillator facility [15] and consists of an extruded polystyrene core (Dow Styron 663 W) doped with blue-emitting fluorescent compounds (PPO 1% by weight and POPOP 0.03% by weight) and a co-extruded TiO_2 coating (0.25 mm thick) for reflectivity. The cross-section of the bar is a isosceles triangle with a base 33 mm and height of 17 mm, with a hole placed at 8.5 mm from the base. The hole has 1.7 mm diameter to host a WLS fiber for read-out. Optical glue ensures the coupling between the fiber and the scintillator. The main characteristics of the scintillator are:

- Good LY
- Radiation hardness (5% degradation observed after 1Mrad γ irradiation)
- Low cost
- Fast response (τ few ns)

The triangular shape allows a gap-free assembly when two bars are put one facing the other, in an almost self-sustaining shape. Moreover, the amount of light

shared between two adjacent bars depends on the position of the impact point of the particle respect to the triangle centers (i.e. the position of the WLS fibers). This allows to determine the impact position in the direction orthogonal to the fiber with about 3mm resolution, much better than the one expected for rectangular shaped bars (roughly 10 mm) given the 33 mm spacing of the fibers.

For what concerns WLS fiber we did not decide to use Kuraray Y11, that are extensively used in this kind of detectors, without any comparison with other fibers. We were motivated by time resolution constraints (see Section 4.1), in fact fluorescence time of Kuraray Y11 is O(10ns) that could be potentially worse if compared with other kinds of fibers. A fiber produced by Bicron was considered: Bicron BCF92 [2]. BCF92 and Kuraray Y11 main characteristics are compared:

Fiber	*Attenuation Length (m)*	*Decay Time (ns)*	*Emission Peak (nm)*
Kuraray Y11	3.5	O(10)	476
Bicron BCF92	3.7	2.7	492

Our figure of merit for fibers was the time resolution. We measured time resolution in a realistic experimental setup. We constructed two bars equipped with testing fibers, and cosmic rays were used as signal source. Read-out was provided by the same photodetector, a Silicon PhotoMultiplier (SiPM; see Appendix A) produced by IRST. Trigger was provided by the AND of a couple of small scintillators positioned on top of each bar.

The threshold used for bar signal discrimination was defined in terms of number of SiPM photo-electron (p.e.) . A TDC was used to measure the time difference among trigger and and discriminated bar signal. Comparison between Kuraray Y11 and Bicron BCF92 for two different threshold is reported in Figure 4.4. With this

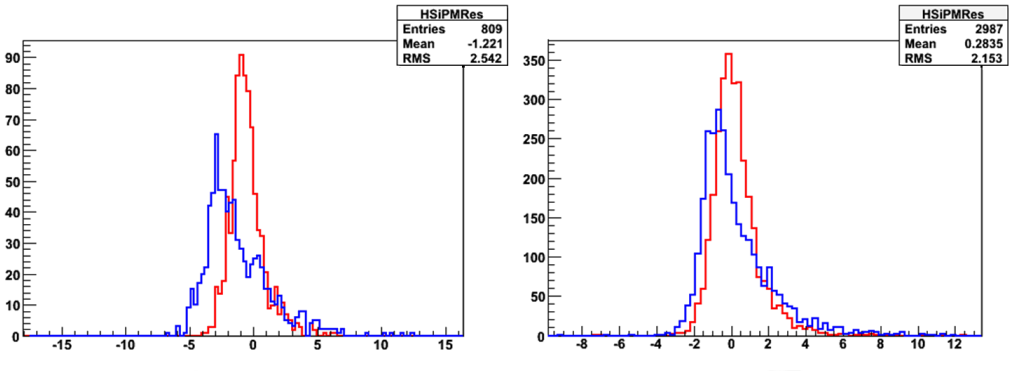

Figure 4.4: Bicron BCF92 and Kuraray Y11 time resolutions compared for two different bar signal threshold.

mind we can conclude that Bicron BCF92 has a better time resolution and then is our choice.

The fiber is read only at one side, and in order to recover light emitted in the direction opposite to the photodetector it is mirrored at one end, by means of Al sputtering in vacuum, using the same technique developed for the fibers of the ALICE Electromagnetic Calorimeter (EmC) [42].

The read-out was provided by Silicon Photomultipliers (see Section 4.5) coupled with fibers through a precisely machined connector.

4.4 Mechanics and Supports

The six CHANTI stations are placed inside a single vacuum tight vessel together with the GTK-3 station. A possible solution, using a rectangular vessel with a vacuum tight removable cover, is sketched in Figure 4.5 where the last GTK station and the CHANTI stations are visible. Mechanics and supports for GTK-3 will be the same as for the other two stations.

Each CHANTI station is composed of scintillator bars glued together, but in order to reduce the risk of mechanical breakdown (and consequent interferences with beam) a light Aluminum frame is supporting mechanically each station. A sketch of a single station with safety frame is shown in Figure 4.6.

One station is composed of 46 bars with different length. The bars outside the beam gap are all of the same length, the so-called long bars (L). Since the gap is of rectangular shape, the bars in the central parts are of two different lengths, depending whether they are in the horizontal layer or in the vertical one. There are so-called middle (M) bars and short (S) bars respectively. The full length is 300mm (L), 117.5mm the middle type (M) and 102.5mm the short type (S). Following table summarizes the composition of one station:

Bar type/Layer	*L*	*M*	*S*	*Total*
Layer Y	10	-	12	*22*
Layer X	10	14	-	*24*
Full station	20	14	12	*46*

Every scintillator bar is provided with a custom designed connector (see Figure 4.7) which is inserted in a precision hole (⌀ 1.02 mm) made on the bar and coupled to the photodetector.

A precisely machined screw cap holds the photodetector in the right position. Of course it's characteristics were fixed only once we defined the photodetector technology to adopt (see Section 4.5).

The precise definition of the position of the bars is given by a custom machined reference jig (see Figure 4.8), on which each bar is placed "cusp down" to form a planar surface with the nominal dimensions. Bars in the orthogonal direction are then glued to these ones to form a "waffle-like" structure. The complementary bars are finally added in both directions to form the final planar station. See also Section 4.6, Figure 4.19 and Figure 4.20 for details. Figure 4.20e shows the final geometry with the read-out connectors on the four sides of the station.

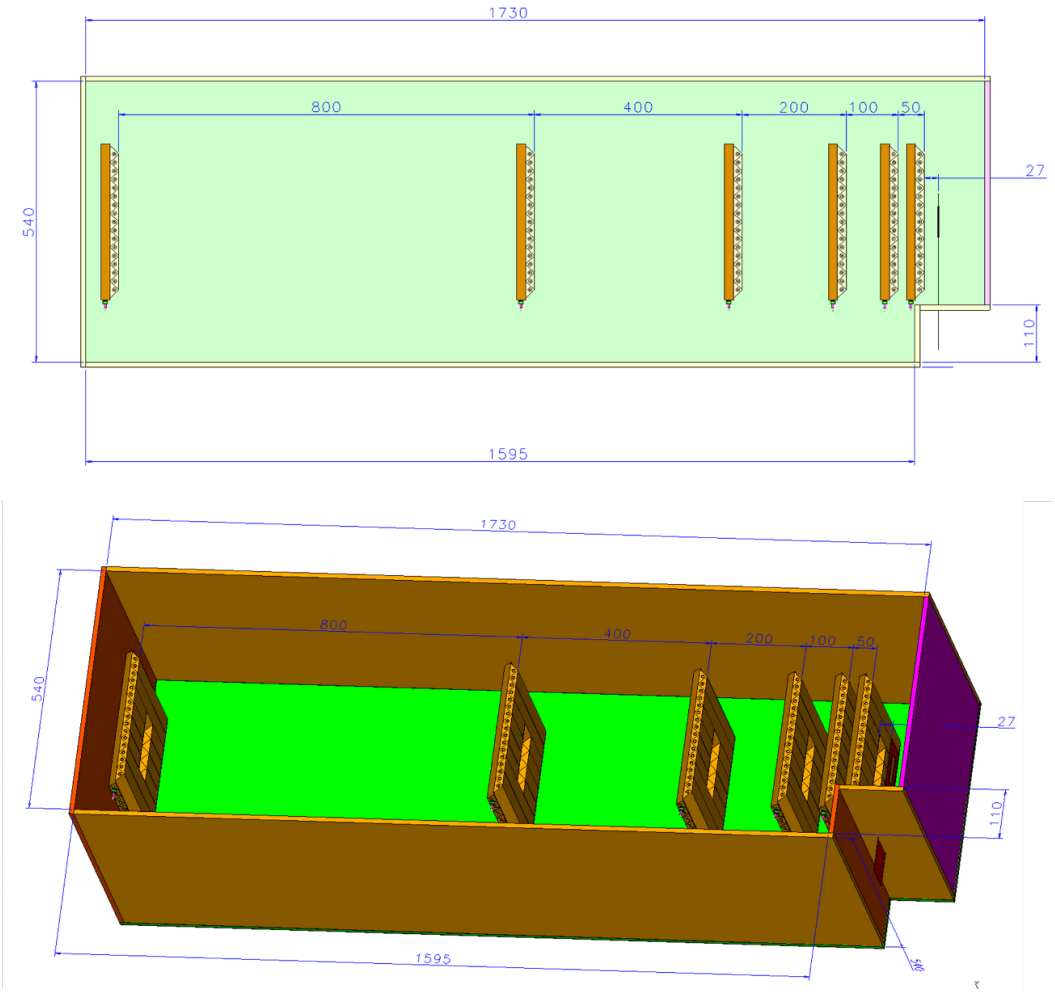

Figure 4.5: Layout for GTK-3 - CHANTI vessel. Vacuum flanges are not shown.

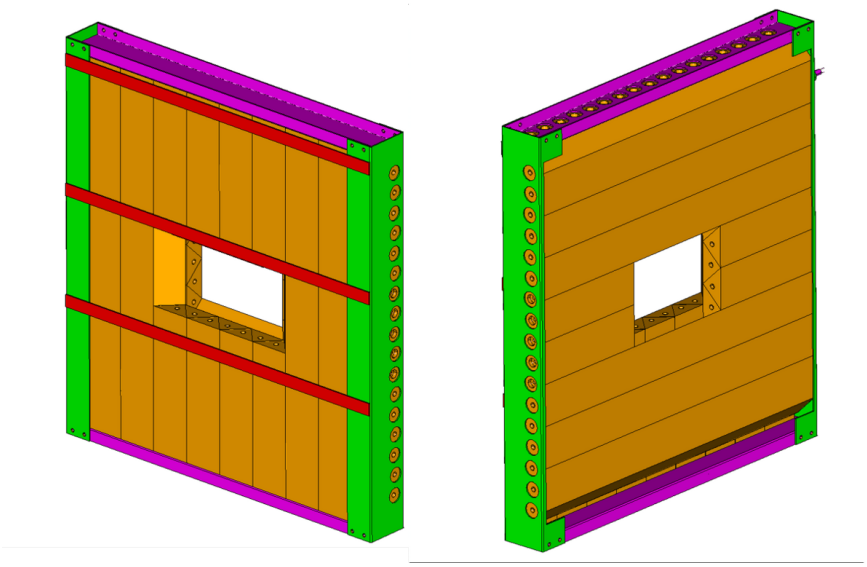

Figure 4.6: A sketch of a single CHANTI station, with the elements of the supporting frame (in green, violet and red). Left: beam view; right: rear view.

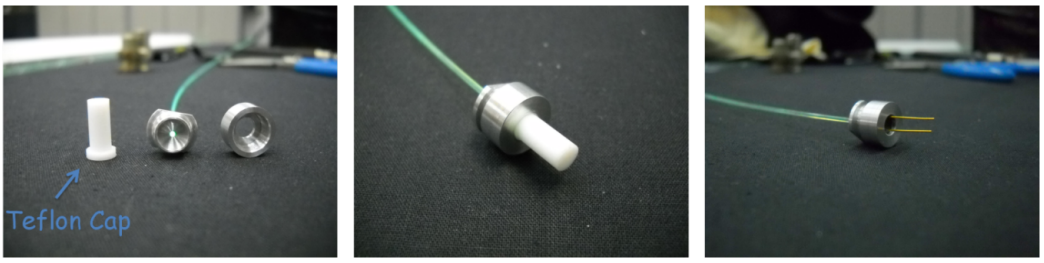

Figure 4.7: Connector designed in order to accommodate an Hamamatsu SiPM a) connector in its basic parts b) assembled connector with protective Teflon cap c) connector in its final shape with SiPM inside.

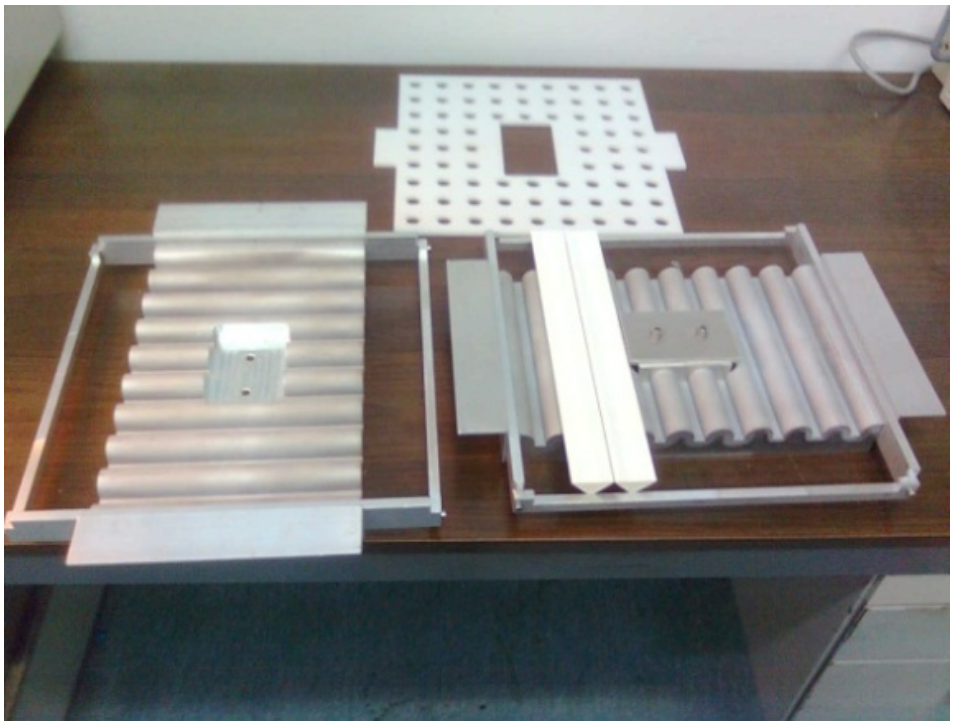

Figure 4.8: Jig used to align bars during gluing, on top Teflon mask to distribute glue spot.

4.5 Photodetectors

The technology choice for light collection must follow the specifications of Section 4.1. In particular we investigate the Silicon Photomultiplier (SiPM) solution (see Appendix A for a general view about SiPM). The use of SiPM devices as alternative to traditional photomultipliers tube (PMT) is becoming a widespread solution in particle detectors when high number of channels or high level of integration is needed. Moreover these devices are the answer to both low heat dissipation and compact geometrical dimensions.

However gain is comparable to standard photomultipliers and can be reached with no need for an HV system, since the operation voltage is typically between 30 and 70 V and the leakage current of order of few nA. They can sustain very high rate, O(10 MHz) without problems. The dark rate (i.e. the rate observed with a counter at 0.5 pe threshold), depending on manufacturer, on the pixel size and on the overvoltage, can vary from 100 kHz and few MHz at room temperature. It is not a concern if the number of expected photoelectrons is reasonably high, since it scales roughly by an order of magnitude per photoelectron as far as the threshold is increased to 1.5, 2.5, 3.5 pe and so on. Working with, for example, 3.5 pe threshold reveals a typical dark noise of about 100 Hz/channel.

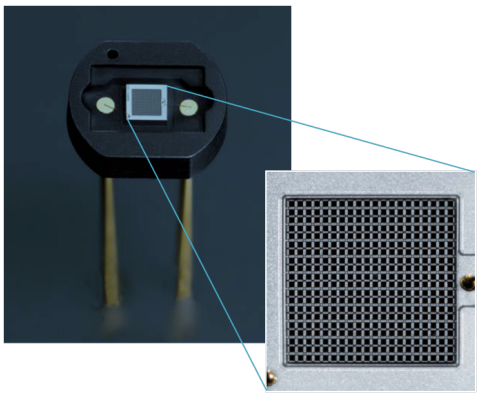

Figure 4.9: Hamatsu SiPM in ceramic packing.

SiPMs are intrinsically radiation hard devices. There is however, as for all semiconductor detectors, a known issue with their behavior after intense hadron flux irradiations [33]. In particular neutrons have generally a major role.

The ASTM E722-93 standard practice allows to compare damage on silicon devices from different neutron sources by normalizing it to the damage induced by mono-energetic 1 MeV neutrons. In this context the figure of merit of an environment for SiPM devices is the flux of equivalent 1 MeV neutron cm^{-2} crossing the detector, this normalized flux is called "fluence". It is known from literature [10] that a neutron irradiation corresponding to $4{\times}10^{8}$ cm^{-2} 1 MeV equivalent neutron or less gives no visible effect on SiPMs, while increasing further the irradiation the dark noise

starts increasing, reaching about 10 times its initial value at about 2-3$\times 10^9$ cm^{-2} neutron fluence. Even if a 10 times larger noise respect to the standard one could still be manageable by increasing the threshold by 1-2 p.e., we have checked that the radiation should be below this level at the CHANTI for at least two years of operation.

This discussion shows that before any definitive choice, we have to study neutron fluence. Protons have been neglected into the following analysis since largest part of neutrons and protons are produced by beam tails scattering in the material upstream the final collimator placed 1m upstream of the CHANTI, which will be able to drastically reduce the proton flux on the detector.

We developed a GEANT4 simulation. In particular we had a realistic beam and geometry implemented. For what concern neutrons, they were tracked using Monte Carlo truth information and were extrapolated on the surface of each CHANTI station. The function used to normalize the neutron flux to fluence is reported in Figure 4.10.

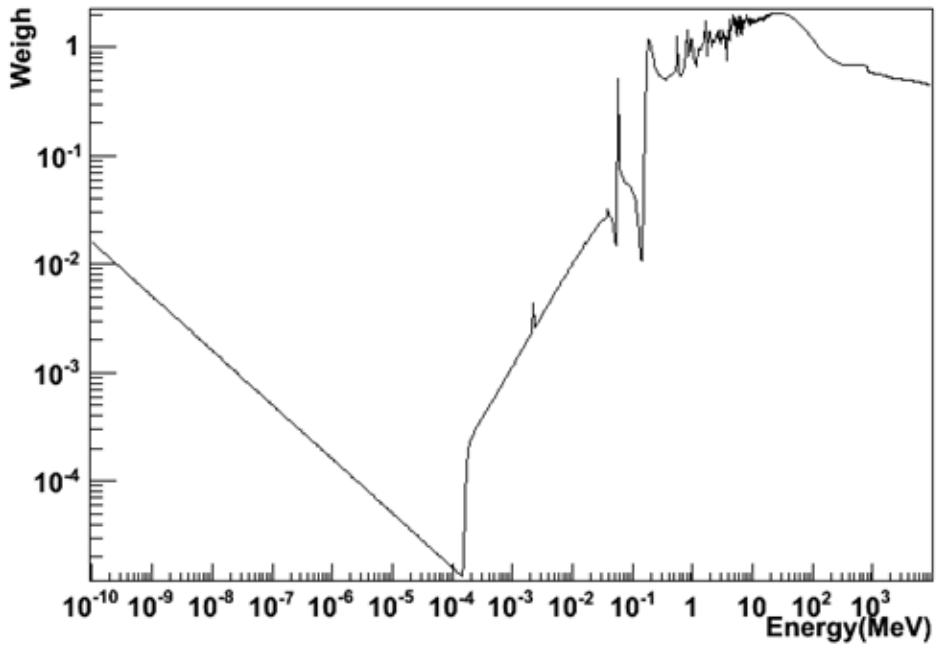

Figure 4.10: Function used to normalize flux to fluence.

Simulated neutron fluence on first CHANTI station is reported on right side of Figure 4.11, the continuous line is the CHANTI border and the dotted line is the region were SiPMs (see left side of same figure) will be placed, in this region mean value of fluence is 1.25$\times 10^8$ neq cm^{-2} y^{-1}.

Unfortunately this simulation does not take in account the neutrons coming upstream CEDAR detector. In this region the beam optic is very complicate and a GEANT4 simulation is not the best choice. For this reason a parallel simulation

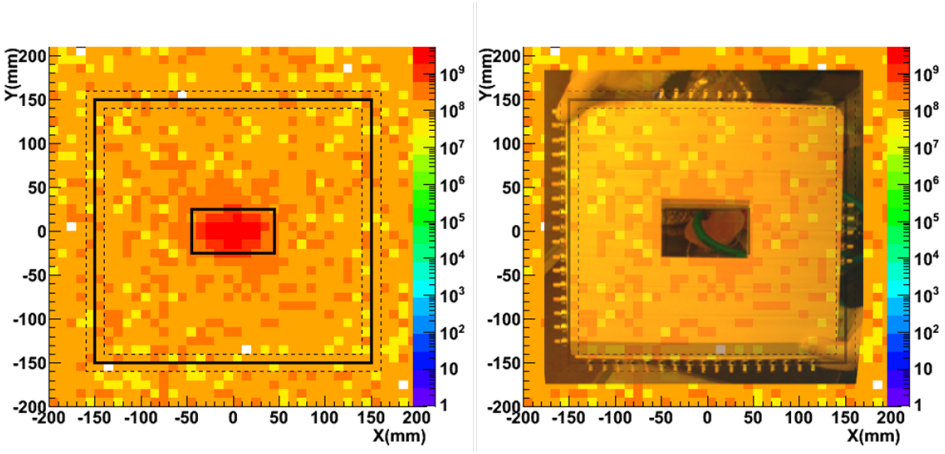

Figure 4.11: On left side neutron fluence on first CHANTI station, on right side same plot with CHANTI station in translucency.

was developed using FLUKA Monte Carlo simulation in order to estimate also this contribute. The result was 0.04 Gy/y that correspond roughly to 10^8 neq cm^{-2} y^{-1}.

Combining the two results we have that in two years running of NA62 the CHANTI SiPMs should integrate no more than 4×10^8 neq cm^{-2} i.e. should operate in safe conditions.

Once fluence was estimated and SiPM was chose as our baseline solution, we developed some tests able to decide the device to install on CHANTI. We took in account some Hamamatsu SiPM [3] series 13-50, 11-50 and 11-100 (first number 13 or 11 is the SiPM dimensions in tenths of millimeter, second number 50 or 100 is the pixel size expressed in microns). Hamamatsu provides, for each SiPM, specifications and working parameters as bias voltage, gain and dark rates (all of them measured at 25°C). In order to reproduce climatic conditions we used a thermostatic chamber that could fix temperature better than 0.1°C.

As the signal time characteristics were the same for all the families, our figure of merit was the relative light yield. Test consists to measure the light yield of each SiPM coupling them with a 30 cm long test bar using a reproducible signal source. In order to do that we used a collimated Sr^{90} source. Signals was amplified using a 20 db fast amplifier and 1 GHz bandwidth. Data was collected using a Tektronix TDS5054 5GS/s oscilloscope via GPIB connection and a custom LabView program. Oscilloscope bandwidth was 500MHz, enough to follow few nanoseconds signal rise time. A part of experimental apparatus is reported in Figure 4.12.

As above our figure of merit was thr relative comparison in terms of number of photoelectrons collected. First of all we measured for each SiPM Single Photoelectron Response (SPR) or in other words the conversion factor between integrated charge and the number of photoelectron. This operation has been done using the thermal-generated signals (see Figure 4.13). Each peak corresponds to a defined number of generated photoelectrons, each peak was fitted using a gaussian in order

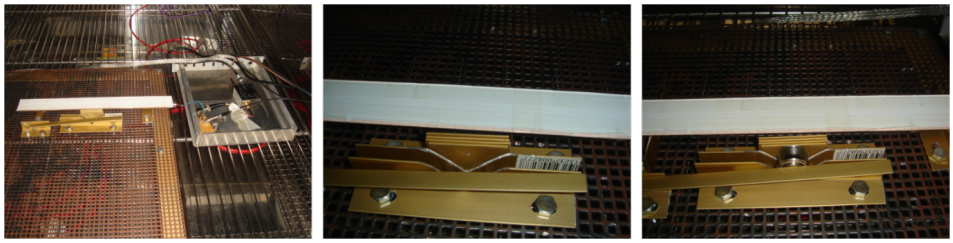

Figure 4.12: Experimental apparatus for bar test. a) Setup overview on the right the read-out electronics and amplifier. b) Collimator detail. c) Source in finial position.

to measure mean value. To reduce systematics contribution, SPR was measured taking the difference of two adjacent peaks (in this case 2^{th} p.e. minus 1^{th}).

Once obtained the single photoelectron normalization factor the ratio signal/SPR for the irradiated bar could be used to compare different devices.

Measured light yield for each SiPM is reported in Figure 4.14. We can conclude that SiPM serie 11-50 has a significantly lower photoelectron yield, while both 13-50 and 11-100 series seem viable solutions for our purposes.

4.6 Prototype construction

Once photodetection technology was chosen in definitive way we started to design all the details with the idea to realize a prototype. First of all we needed to design a connector able to accommodate each SiPM. Moreover the connector must provide the best alignment between the fiber center and the photodetector sensitive area. This was guaranteed at the level of 50 μm and is dominated by the tolerance in the position of the photodetector area respect to its frame as provided by Hamamatsu. It is worth to note that it is possible to substitute a photodetector by just unscrewing the connector. In Figure 4.7 there is one connector realized and coupled with a fiber.

CHANTI prototype has been assembled in Napoli at the end of July 2010. It is a full dimension prototype of a X-Y station. Scintillator bars for the prototype were obtained courtesy of FNAL and Al sputtering of the fibers was performed at LNF.

The construction procedure adopted is hereby briefly described. First, some custom tools to simplify the mechanical assembly were developed. The assembly took about 20 days, and can be divided in three main parts:

1. Gluing fibers into bars,

2. Test of the bars,

3. Assembly all test-passed bars into final X-Y station.

A single X-Y station contains three different types of bars: 300mm (L), 117.5mm (M) and 102.5mm (S). All operations have been done in a class 100 clean room

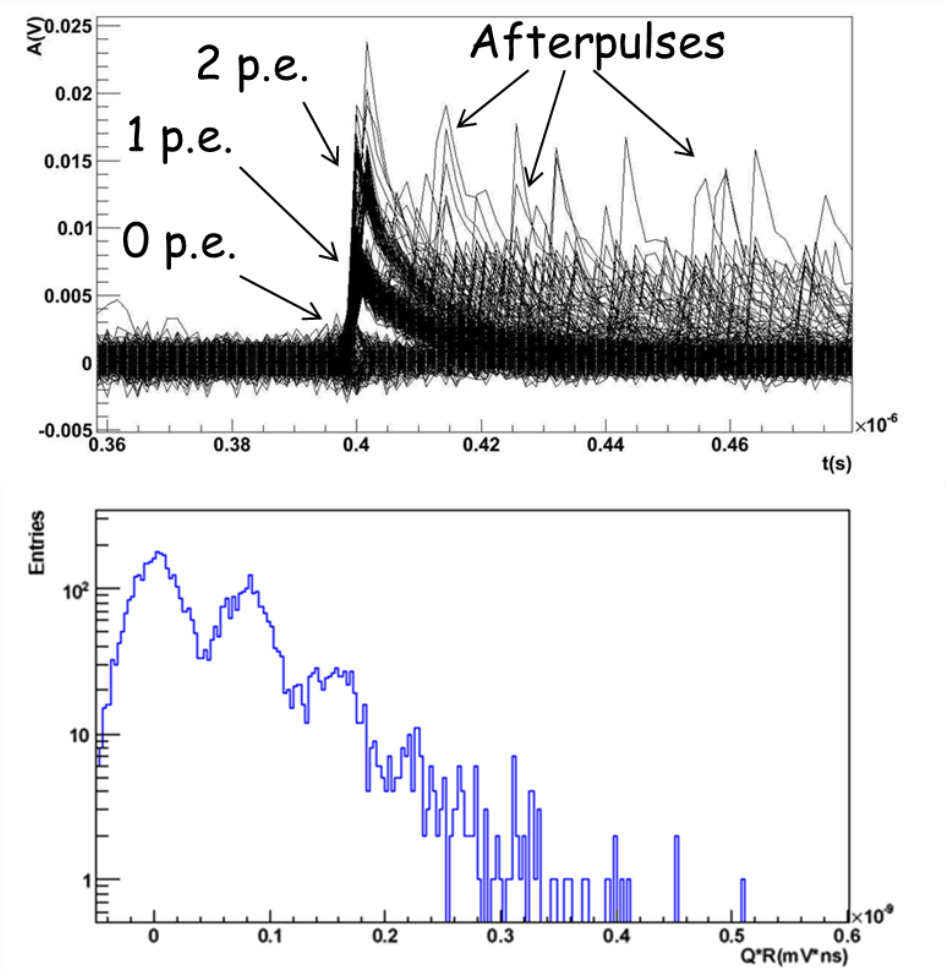

Figure 4.13: a) Thermal generated waveforms at 25°C, b) Dark noise spectrum obtained integrating waveforms shown on top.

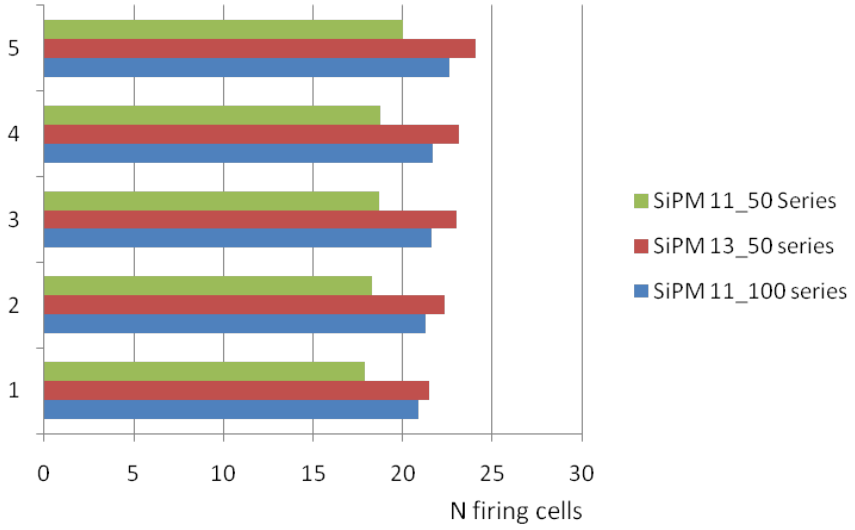

Figure 4.14: Photoelectron yield for photodetectors of three different Hamamatsu SiPM series. Five photodetectors have been measured for each series using the Sr^{90} source.

environment and all components have been accurately washed using an ultrasound cleaning before handling.

Gluing of the Fibers into the Scintillator Bars

This operation is itself done in two steps. First mirrored fibers and connectors are glued together and finally this ensemble is glued into a bar.

Fibers-Connectors Gluing

Each connector is provided together with a Teflon© cap. It is a multi-purpose tool (Figure 4.7) to define a reference plane for the fibers as well as to protect the polished side of the fiber during transport and handling.

During the prototyping phase different glues were tested and the epoxy ARALDITE 2011 was found the best choice for this application. It has a high viscosity which helps to prevent glue leaking into the wrong connector side through the very thin gap between fiber and connector. This glue is also solvent-free avoiding cladding damages. Optical properties are not important at this level, because no coupling is required. Fibers are plugged in their final position into connector, being careful they reach the Teflon cap. A special support (Figure 4.15) has been developed in order to parallelize this operation. It is able to carry 24 fiber-connector couples. When the fiber is in its correct position glue is spilled using a syringe (with a $\oslash$ 1.3 mm needle).

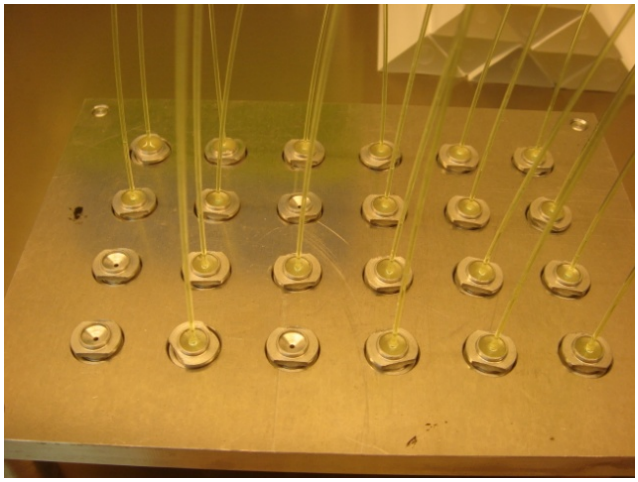

Figure 4.15: In order to reduce uncertainties in fiber positioning we developed this tool, connector with its Teflon cap is positioned in a hole and fiber is positioned into the right position before to spill the glue.

Fibers-Bar Gluing

Once obtained the fiber-connector ensemble they were glued into the bars. An other custom tool (Figure 4.16) allows the user to fix the bars in vertical position. It can host up to 10 bars, and was used to hold the bars during the hardening of the glue. Five days are necessary to glue all the bars for one station.

Glue used is a SCIONIX Silicon Rubber Compound, that guarantees a good fiber-scintillator optical coupling and is known from NASA database [4] to be low outgassing. Several other compounds were tested but showed worse spatial properties, in particular for what concern bubble production (in Figure 4.17 are reported some tests). Before the use the glue is outgassed in order to reduce air bubble held inside. The glue is injected from the bottom using again a syringe. This method was found to reduce the risk of trapping air bubbles in the glue. Required glue quantities are adapted for each bar length (L $\rightarrow$ 2.1 ml, M $\rightarrow$ 1.0 ml, S $\rightarrow$ 0.9 ml). This is important in order to avoid leaking at the top of the bar.

The whole prototype contains about 65 ml of glue.

Scintillator Bar Test

Since after complete assembly any bar substitution is impossible a quality test before assembly is needed. For each bar the response to a Sr^{90} collimated beta-source is measured. Measurements have been carried out with the same setup described in Section 4.5 for the SiPM comparison, in a controlled temperature environment using the same photodetector (an Hamamatsu 13-50 type) coupled each time to a different bar. Experimental apparatus is in Figure 4.12.

Relative comparison among different bars in terms of number of photoelectrons

Figure 4.16: The fiber-bar gluing tool in action. Its back side is identical to the one shown. Glue is injected from bottom using syringe.

Figure 4.17: Here are reported the results of some tests did in order to chose the optical glue, to test different glues a glass capillary has been used in order to simulate the hole inside each bar, moreover a fiber has been inserted.

collected is again our figure of merit. Figure 4.18a shows all bars normalized source-response in terms of number of photoelectrons. Mean values for each curve are given in Figure 4.18b : one can conclude that the bars quality is very uniform. Only one bar showed a significant difference, the cause of low light response was understood, after inspection of the bar: the fiber edge was found slightly backward with respect to its reference plane facing the SiPM sensitive surface, leading to lower light collection efficiency.

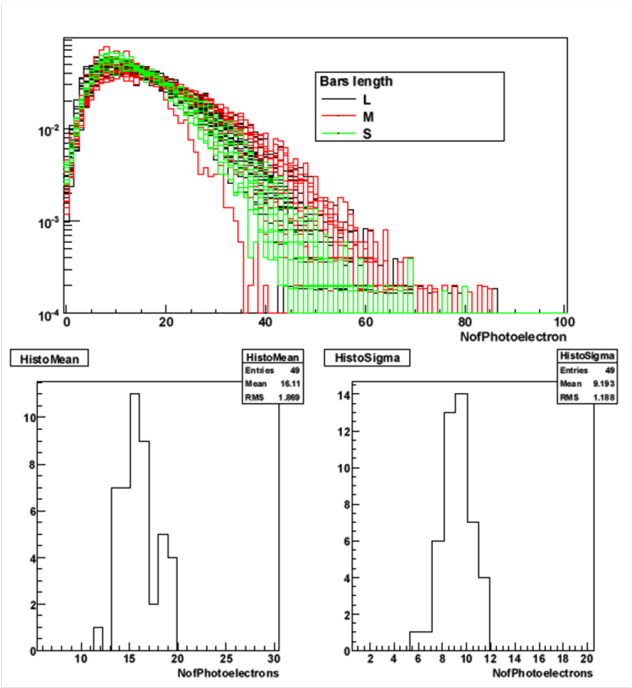

Figure 4.18: On top is reported the response, in terms of photoelctrons, of each bar if exposed to the source, on bottom the mean values and RMS' of such distributions.

Module Assembly

Once all the material was ready, a prototype could be assembled in 2 steps. Each step takes one day.

During the first day a half-layer X and Y are glued together. First of all bars are arrange on a jig (Figure 4.8), afterwards glue points are defined using a Teflon mask. Then the bars of the other half-layer were aligned on top. A second jig is put on top of the assembly to align the last half-layer. Pressure is added to increase the glue uniformity. Each glue spot contains 0.1 ml of glue.

On the second assembly day the prototype is completed. Figure 4.20 shows all the steps of the procedure. First of all bars of a half-layer are aligned on the jig and glue spots are applied (3 for L-type bars and 2 for M and S type bars). Then the complementary half-layer is put on top. Again glue spots are placed and the

last half-layer placed. A weight has been applied in order to uniformly distribute glue. For the whole module about 9.5 ml of structural low outgassing epoxy glue (3M DP490), identical to the one used for the reinforcement of the LAV blocks, was used.

Figure 4.19: Assembling "First step": a) A half-layers is arranged on the jig, b)Teflon mask is aligned, c) Glue spots are applied, d) Mask is removed, e) f) Bars of the other half-layer are placed, g) h) second jig is applied on top to align last placed half-layer and to redistribute pressure, i) Half-module as appear the day after gluing.

4.7 Read-out

The conceptual scheme of the CHANTI read-out is shown in Figure 4.21. As previously sketched each scintillator bar is coupled individually to a SiPM which converts light collected by the fiber into electrical signals. Each SIPM has two pins which are used both to polarize it and to read these signals. The bias voltage is brought to the SiPMs inside and the signal are carried out from the vacuum tube using appropriate vacuum tight flanges as done for the LAV signals and HV. Both twisted pair and coaxial cables are being investigated as possible solution for the internal cabling , the final choice being the one which optimizes cost/benefits ratio. A small amplification board is placed just outside vacuum in order to be able to transfer signals from the detector to the FEE crate with an acceptable S/N level. Typical signals are expected of order few mV (on 50 Ω impedance) with a fast rise time (1 ns) and

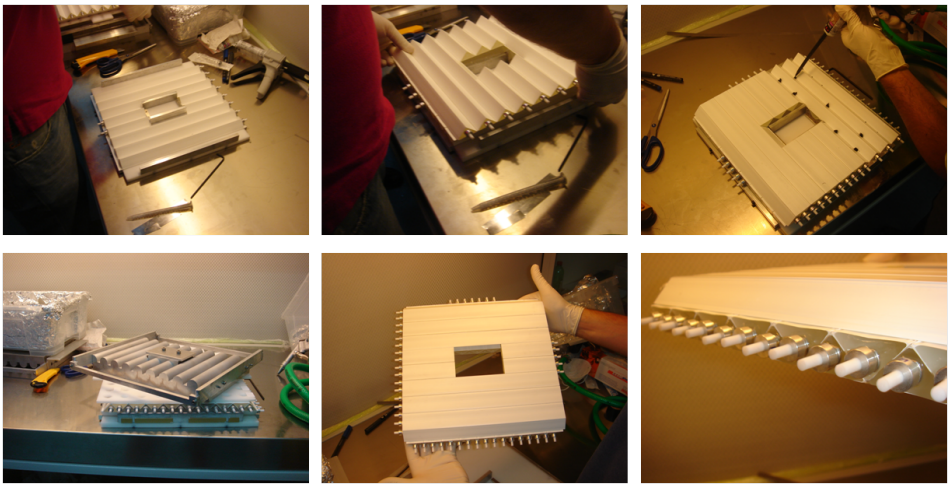

Figure 4.20: Assembling "Second step": a) Half-layer bars ready to be glued to half-module, b) Gluing half-module, c)Last half-layer gluing, d) Weight applied, e) Prototype as appears after one day, f) Connectors detail.

a somewhat long decay time (in the range 10-100 ns). The maximum expected rate in input to the FEE will be, for the inner bars, of the order of about 1 MHz per bar, as shown by Geant4 simulations, plus the dark rate (for Hamamatsu SiPMs, some 100 kHz). In order to keep some safety factor, the electronics will be designed to cope with a 5 MHz rate.

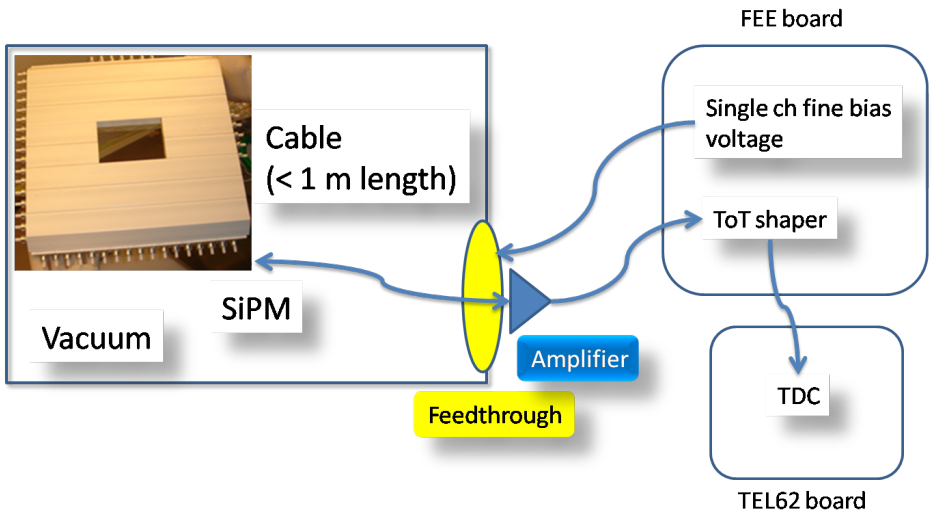

Figure 4.21: CHANTI read out scheme.

4.7.1 Front End Electronics

The FEE boards provide for each channel:

- a way to control the V_{bias} with O(10 mV) accuracy,
- a fast, DC coupled, conversion to a Time Over Threshold-LVDS signal output,
- a temperature and/or a dark current (with nA resolution) monitor for slow control adjustment of the V_{bias}.

Thresholds and V_{bias} settings will be controlled using the CANOpen standard. The LVDS output will be directly sent to a TEL62 board equipped with HPTDC for both leading and trailing edge measurement. The total number of channels needed is 46×6 = 276. One TEL62 board equipped with three 128 ch TDC boards will be able to readout the whole system and provide also a large number of spare channels.

The TOT technique will approximate charge measurement to improve the spatial resolution of the system, and correct for time slewing effects.

4.8 Preliminary prototype test

The prototype (Section 4.6) has been tested using cosmic rays with the aim to measure the time resolution and MIP response of a couple of bars.

The experimental setup is scratched in Figure 4.22. The coincidence of two small (2×4 cm^2) scintillators give the trigger signal. Data have been acquired using a 4-channel oscilloscope (Tektronix TDS3054) coupled via GPIB to a PC. A LabView program has been used to manage and store data. Oscilloscope choice was done considering its high sample frequency (5 GS/s), this in order to avoid any degradation of the rising edge and then of the time resolution.

Bars read-out was done using two Hamamatsu SiPM of 13-50 family. Signal are amplified after a 1.5 m long coaxial cable in order to reproduce the environmental condition of the future experiment. The amplifier is a custom solution that we want to test in order to use it as front-end amplifier. The amplification is ∼8.

First of all we were able to study the mean number of photoelectrons that a MIP excite in a half-plane. As for SiPM characterization (see Section 4.5) we started to measure the SiPM response to single photoelectron, using thermal generated signals (as described in Section 4.5). Now we can convert charge collected in number of photoelectrons obtaining the plot in Figure 4.23. The mean number of photoelectron per plane is ∼120 (→60 per bar). This suggests that we can set the energy threshold to 1/3 of MIP signal (corresponding to ∼20 pe) without efficiency loss. Increasing the threshold helps to reduce noise due to the dark counts, however this is possible, without any time resolution degradation, only because we will have ToT information for time slewing corrections.

Time resolution was also measured. Oscilloscope permits to collect the waveform of signals; both charge and time information were available. We implemented an algorithm that simulate the time over threshold measurement. The threshold

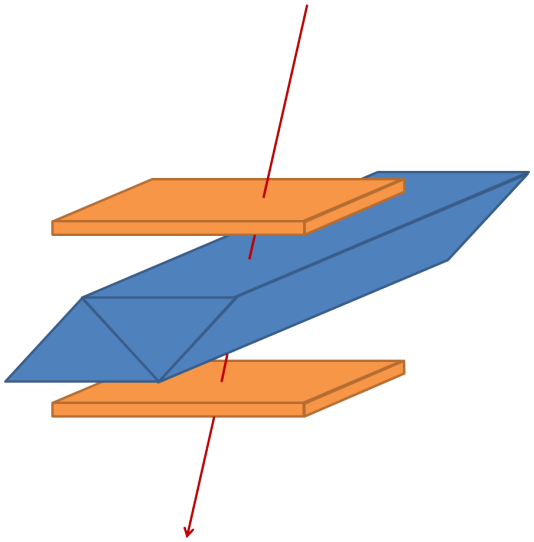

Figure 4.22: Experimental setup for CHANTI prototype cosmic rays test is scratched.

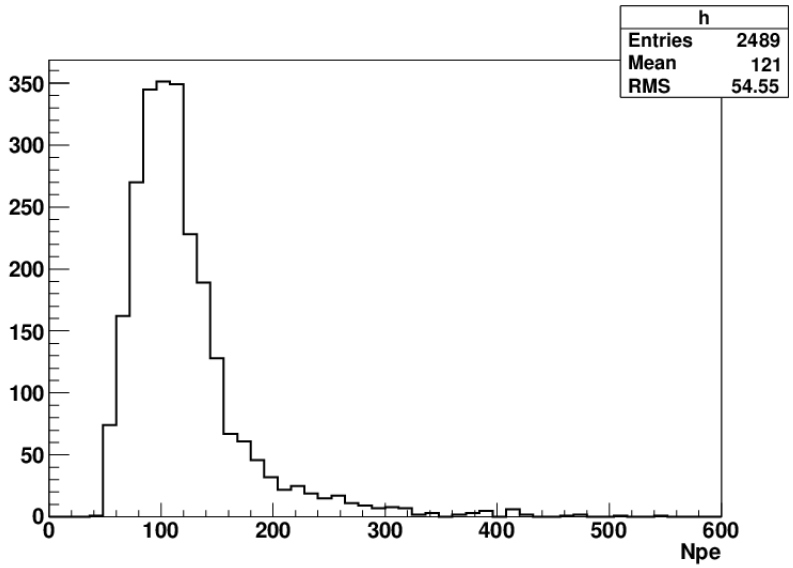

Figure 4.23: The distribution of number of photoelectrons produced by a MIP travelling a half plane.

was fixed at 30 mV (corresponding roughly to 15 pe). Moreover charge integral could be easily obtained. As usual time information need to be corrected for the signal amplitude. As described in Section 4.7 our read-out will be based on ToT technique, this means that this kind of correction must be done using only time informations and not the charge. Time slewing correction was obtained using both informations. Results were compared. An example plot and relative curve used for slewing correction, is reported in Figure 4.24

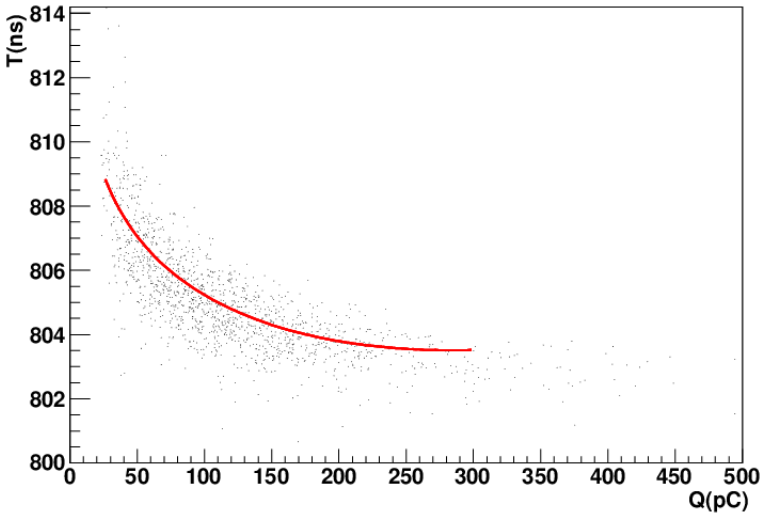

Figure 4.24: An example of charge versus time plot has been reported, in red the curve used to correct times; a similar plot could be implemented with ToT instead of charge integral.

The reference time was provided by trigger time (t_0). From a separate measurement of the time difference among the two trigger palettes we extract a time resolution of O(400) ps for the single palette. The related trigger jitter contribution to the estimated time resolution for the prototype should be subtracted in quadrature but will be negleted in the following: our time resolution estimates are thus conservative. Time resolution for each channel was estimated plotting the difference $T = t_{channel}$-t_0 where $t_{channel}$ is the time of first positive edge with a threshold of 30 mV. In Figure 4.25 are reported the distribution of T for two channels using both ToT and charge time slewing corrections. We can summarize the time resolutions in a table (channel name are referring to oscilloscope input):

	Time slewing by charge	*Time slewing by ToT*
Channel 3	(846±15) ps	(880±16) ps
Channel 4	(927±22) ps	(963±26) ps

We can observe that there are no large variations between time resolution estimation done using different time slewing corrections. The difference in time resolution

among the two channels is easily explained by a slightly different energy release in the two bars, caused by the non perfect alignment of the trigger system with the mid line of the two bars .

We estimated, also, the time resolution of a couple of bars. One more time, we defined T = t_{pair}-t_0. Now t_{pair} is the time weighed with ToT or charge collected. In Figure 4.26 are reported these results. Finally a time resolution using as t_{pair} the smallest time among bars, has been computed and reported in the Figure 4.27.

4.9 Simulation

A GEANT4 simulation was developed. With this tool we could estimate some crucial parameters like efficiency, data rates and fake rates.

Neither digitization nor mechanical supports have been simulated. Only energy release information have been stored.

4.9.1 Efficiency

For efficiency measurements we simulated 10^7 Kaons.

We are interested on inelastic events. Figure 4.28 represents the topology these events. It is clear that CHANTI could provide only an indirect veto, detecting associate particle produced during interaction.

We have to define also what we consider a veto signal. This means to fix an energy threshold over which a bar is considered to fire. This threshold has been fixed using the mean value of energy released by a Minimum Ionizing Particle passing orthogonally through a bar. In particular we decide to use an usual value of 1/3 of a MIP that in our case it corresponds to 0.5 MeV.

The sample of events we consider, in our first approach, takes in account all inelastic events. A CHANTI inefficient event was considered as an event that have no enough bars crossing the threshold we fixed. We stared using a cut of 3 firing bars. This means that an inelastic event in which less than 3 bars are fired, is considered inefficient.

With this preamble we can proceed to discuss the Figure 4.29 were are reported the number of particles (e.g. all the particles produced into interaction) tracks for inelastic events. In black are reported all events and in red only events not efficient. The left side plot is very interesting, it is the magnification of right side plot. We can see how the residual inefficiency is limited to very low number of tracks. Particularly enhanced are 3 and 5 tracks. So we decide to study the topology of these events following each particle using raw Monte Carlo truth information.

Referring to Figure 4.30 we can see the interpretation of these events. The incoming Kaon has a "quasi elastic" interaction. These events are topologically characterized by an out-coming Kaon almost identical to the incoming one and the production of low momentum nucleon. This explains the 3 tracks peak. For what concerns the 5 tracks peak, it is a subsample of these basic events, but with the Kaon decay in 2 body. These events are in someway not really dangerous if Kaon

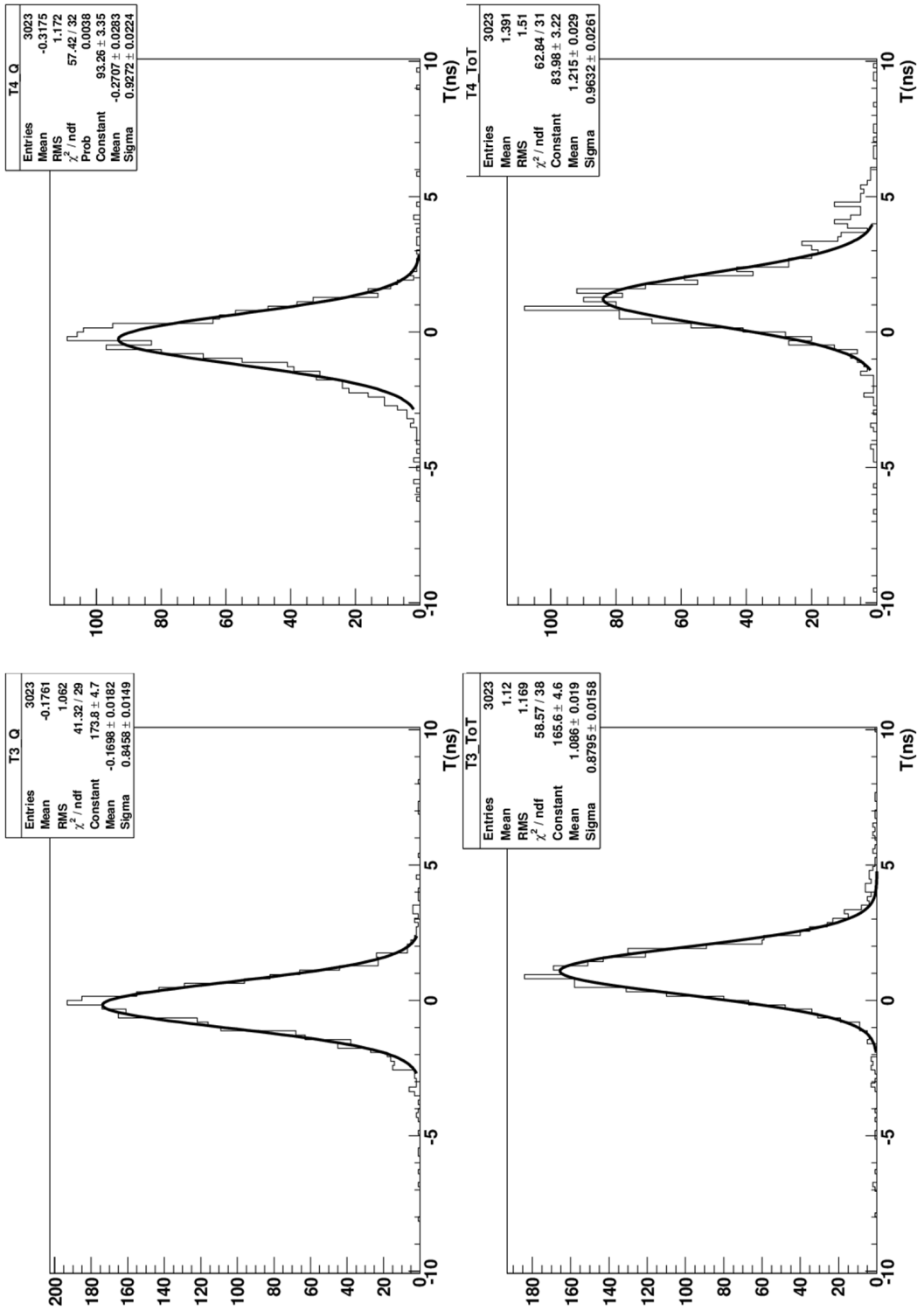

Figure 4.25: Time resolutions for both charge (top line) and ToT (bottom).

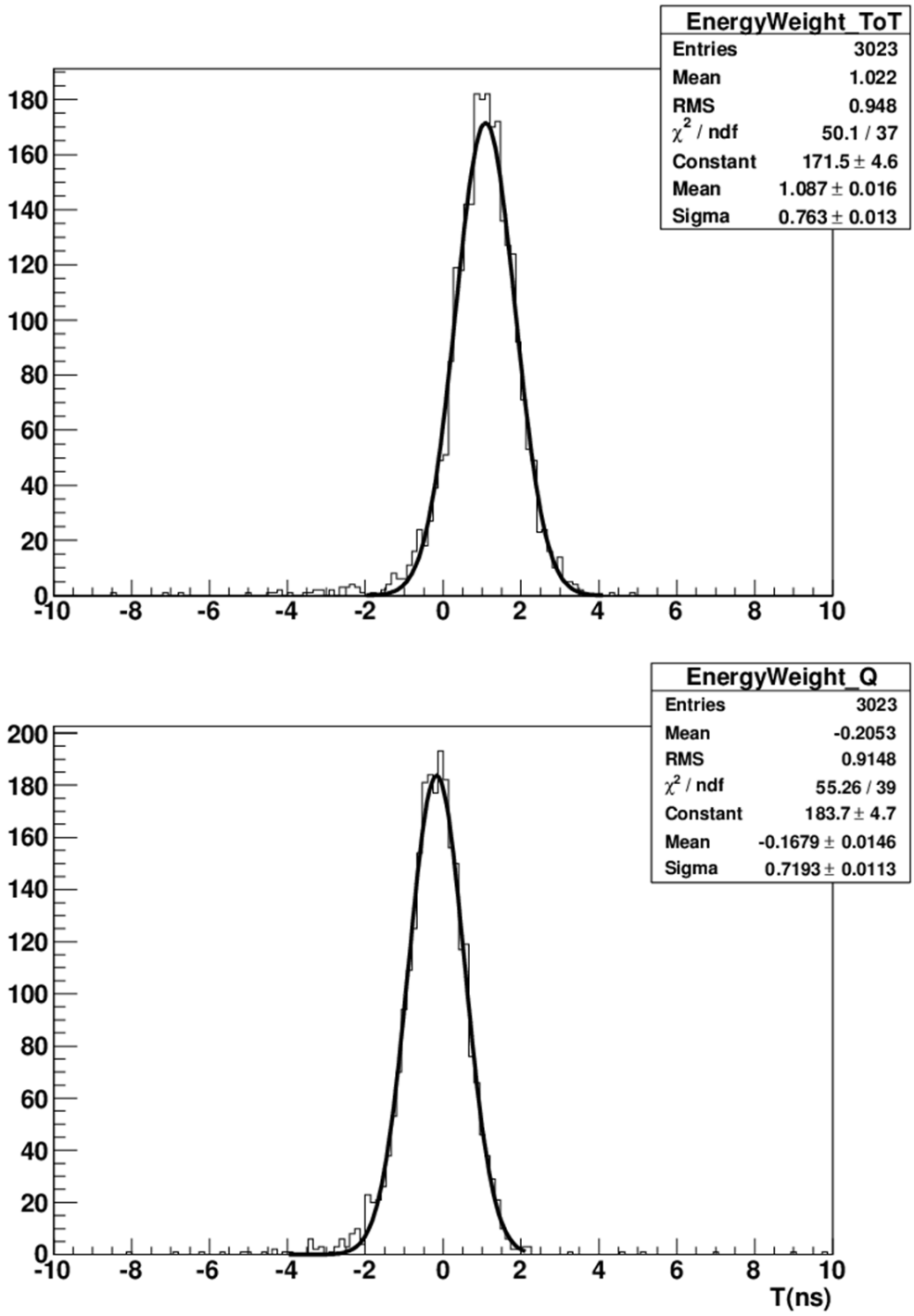

Figure 4.26: Bar-couple time resolution obtained weighing time with ToT (Top) or charge (Bottom); we compare two different time slewing corrections: charge (bottom) and ToT (top).

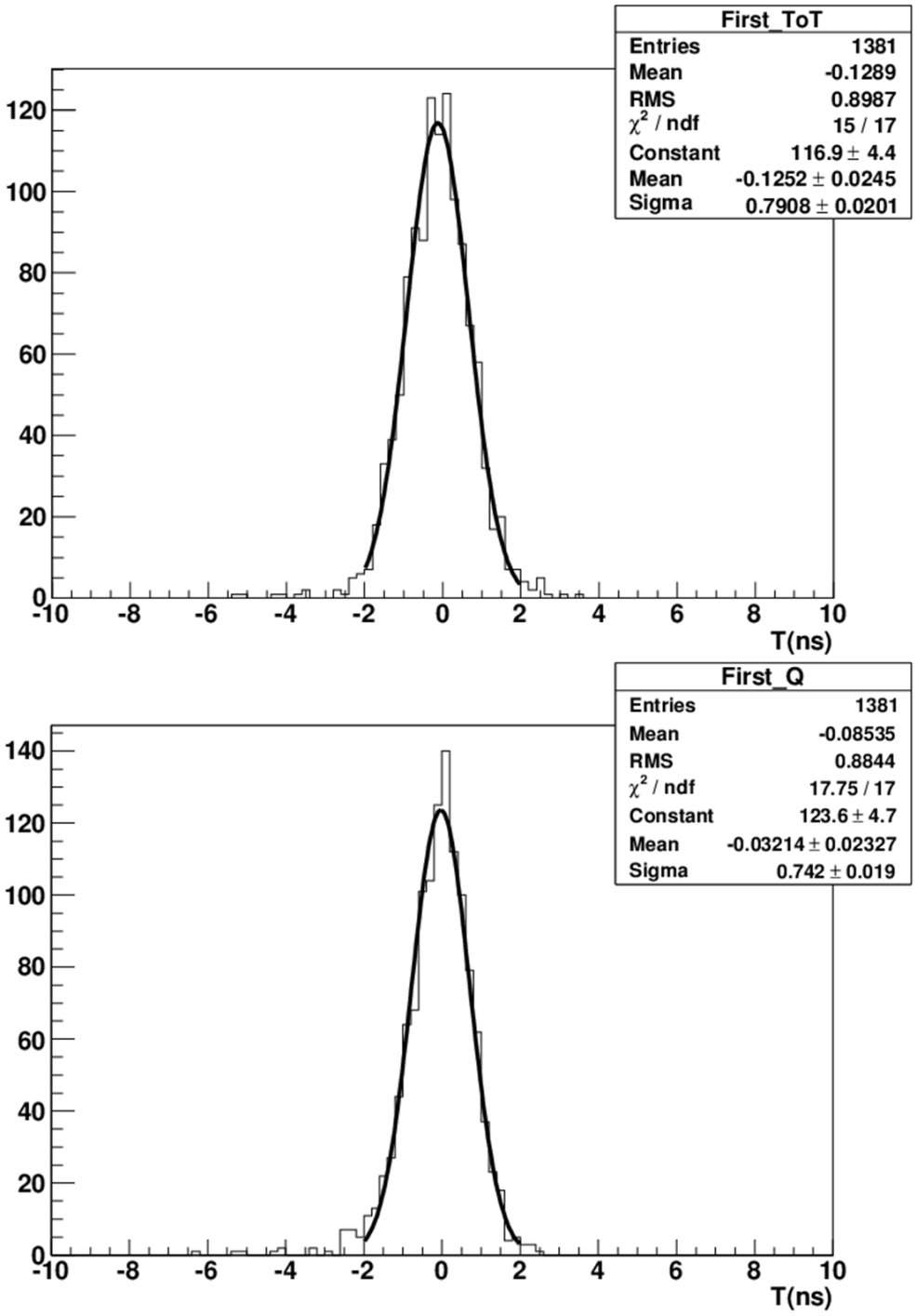

Figure 4.27: Bar-couple time resolution obtained using the smallest time among the bars; once more we compare two different time slewing correction: charge (left column) and ToT (right column); once top line concerns the time resolution obtained using the fastest bar, the bottom line plots are made using the weight mean of time bars with signal amplitude (calculated using once ToT and once charge integral).

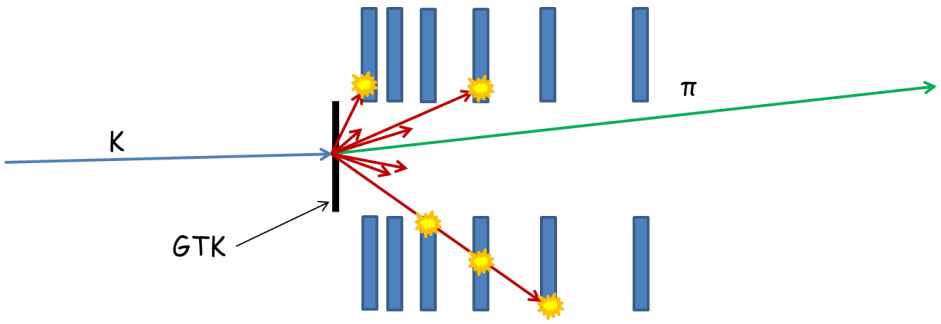

Figure 4.28: Inelastic event topology.

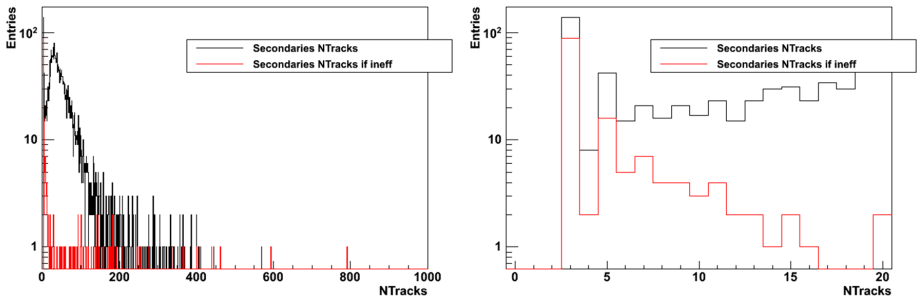

Figure 4.29: Black line represents the number of tracks in inelastic events, and the red line the same but only if CHANTI is inefficient (less than 3 firing bars); on the left side we have the magnification for low number of tracks of right side plot.

momentum variation is more than 1%. We reduced our sample to those inelastic events with an out-coming Kaon momentum that differs from incoming one by less than 2 GeV (3σ from mean value).

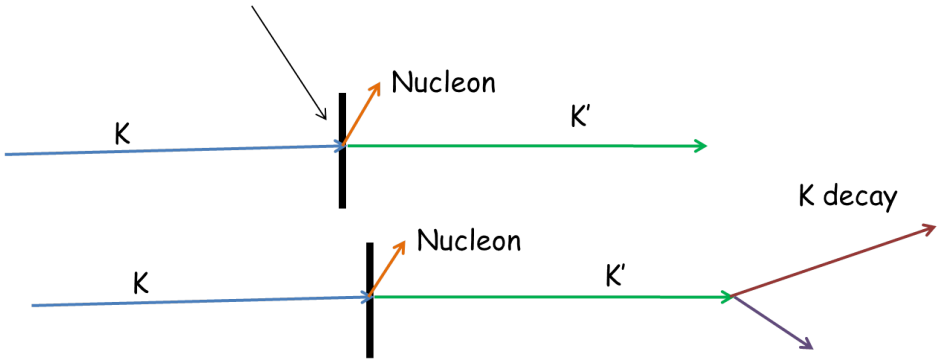

Figure 4.30: Quasi elastic event topology for 3 and 5 tracks.

Finally efficiency was estimated using this new sample. In Figure 4.31 we present the number of firing CHANTI bars for three different energy threshold. The mutual comparison is explicative of a persistent "geometrical inefficiency", in fact zero energy threshold sample is not different if compared to others. We can thus conclude that our main source of inefficiency is geometrical and not reducible using only CHANTI detector. Efficiency is reported into following table:

Nbars/Th	*0 MeV (%)*	*0.3 MeV (%)*	*0.5 MeV (%)*
0	0.68	0.68	0.78
1	0.78	0.78	0.78
2	0.88	0.98	1.17
3	1.47	1.66	1.76
4	1.76	1.76	1.96

4.9.2 Data Rate

Using our simulation also data rate was estimated.

We can distinguish two contributions: beam particles and muon halo.

Beam contribution

Data rate estimation needs to fix some parameters. As discussed in section 2.11 the level 0 trigger is fixed at a rate of 1 MHz and a temporal width multiple of 25 ns (a reasonable choice could be 100 ns). Now each subdetector answers to the trigger supervisor with a sample of events corresponding to the temporal window opened by level 0 trigger. This means that the data rate is proportional to the mean number of events present into this time interval and the number of firing bars per

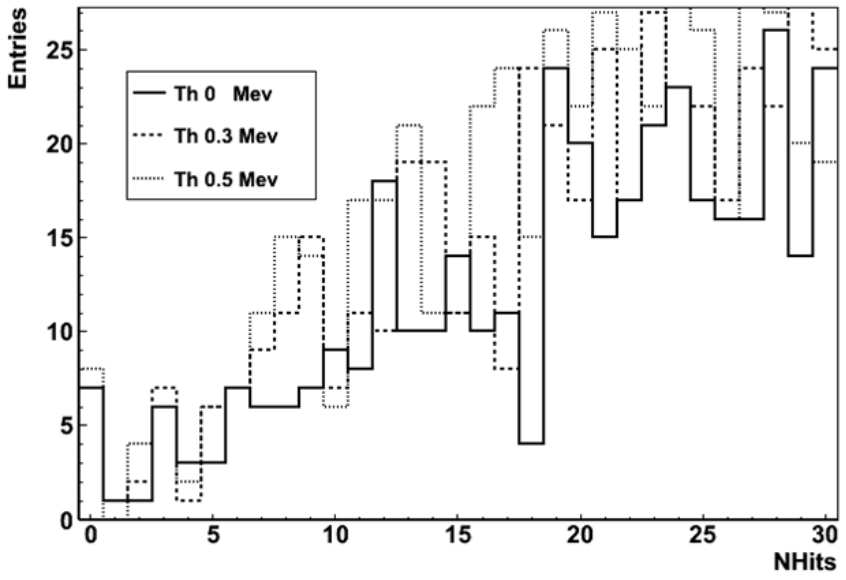

Figure 4.31: Number of fired bars if inelastic event but not quasi elastic.

event (of course zero suppression is adopted). If ν_{CHANTI} is the detector rate (an event is triggered if at least 1 bar is above energy threshold), M is the mean value of firing bars multiplicity, W the dimension (= 4 bytes) of a word that carries out the temporal informations of rising/trading edge, ν_{L0} is the 1 MHz level zero rate and Δt is the 100 ns level 0 trigger temporal window. Finally Data rate (R_{data}) can be expressed as:

$$R_{data} = 2 \cdot \nu_{L0} \cdot W \cdot M \cdot N \tag{4.1}$$

where N is the mean value of the number of events in trigger window: $N = \nu_{CHANTI} \cdot \Delta t$.

Thus we have to estimate ν_{CHANTI} and M.

We defined as energy threshold the value of 0.5 MeV (1/3 of MIP release). A sample of $3.5{\times}10^7$ beam events was generated.

In Figure 4.32 is reported the distribution of the number of firing bar in an event. The firing bars multiplicity M is easily the mean value of this distribution neglecting the bin at zero.

For what concerns the rate, it could be estimated using the integral (I) of this distribution above 1 firing bar, that represents the number of events in which CHANTI has at least two bar over threshold (because zero suppression will be implemented). If ν_{beam} is the beam rate (800 MHz), N_{Gen} the number of generated events ($3.5{\times}10^7$) and N_{Oth} the number of MC events with at least one firing bar, CHANTI rate is:

$$\nu_{CHANTI} = \frac{\nu_{beam} \cdot N_{Oth}}{N_{Gen}} \tag{4.2}$$

Our results are: $M = 7.1$ and $\nu_{CHANTI} = 1.64$ MHz.

Finally referring to 4.1 we can estimate for CHANTI data rate from beam particle: $R_{data} \sim 9.4$ MB/s.

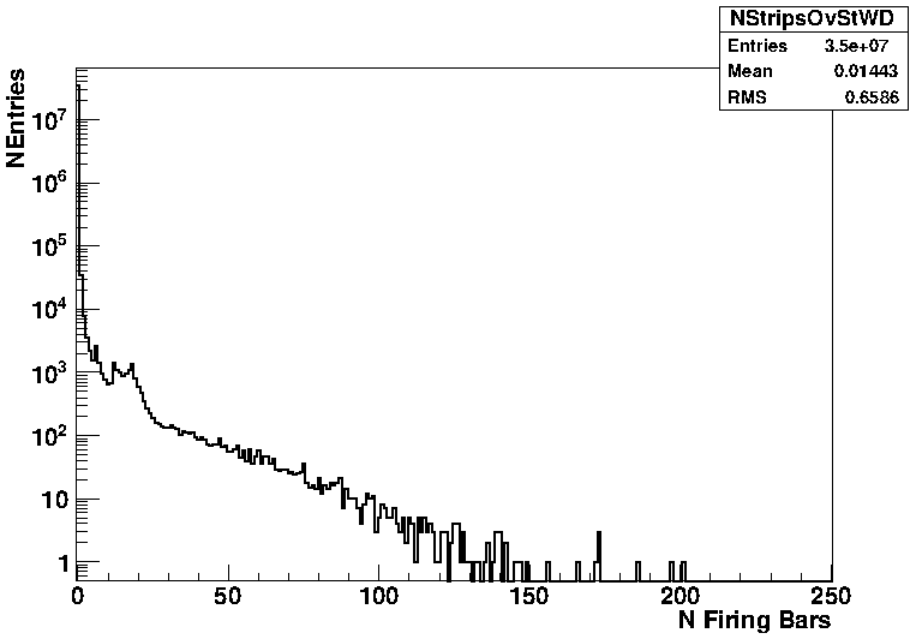

Figure 4.32: Number of fired bars per event, including the (largely dominant) zero fired bars bin.

Muon halo

For what concerns muon halo contribution we have an event rate estimation on CHANTI ($\nu_\mu = 1.3$ MHz) made using a TURTLE simulation.

Moreover as above we need to estimate the bar multiplicity for these events. Muon halo is composed by straight μ, thus is not a mistake to consider that 4 is the number of firing bars per plane, this means an overall number of firing bars of 24. Finally data rate from muon halo is:

$$R_{muon} = 2 \cdot \nu_{L0} \cdot W \cdot M \cdot N \tag{4.3}$$

where now M is 24 and $N = \nu_\mu \cdot \Delta t$.

Using number we presented we have a data rate from muon halo of: $R_{muon} = 24.9$ MB/s.

Summing the two contribution 4.3 and 4.1, total data rate can be estimated: $R = R_{muon} + R_{data} = 34.3$ MB/s.

4.9.3 Fake veto percentage

Fake veto rate has essentially two contribution. Good events in which bars are triggered (e.g. by δ rays produced in GTK3) and random coincidence of CHANTI rate within the time window used to match the trigger time at reconstruction level. The first contribution has been estimated using the MonteCarlo, by counting the number of non-inelastic events where at least one bar of the CHANTI is firing and is reported in the following table (see also Figure 4.33):

Nbars	*0.5 MeV (%)*
1	0.93
2	0.28
3	0.16
4	0.10
5	0.06

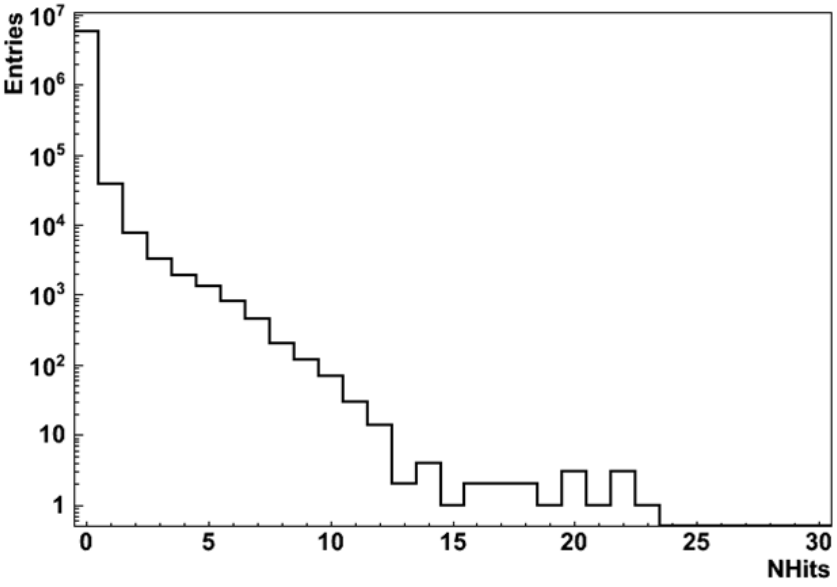

Figure 4.33: Number of firing bars (Threshold 0.5 MeV) if non inelastic event.

From this numbers we can deduce that the main source of fake veto will be the coincidence of CHANTI events with trigger. In fact at L2 level we have a trigger time resolution of ∼100 ps : this means that the width of the time window needed to match activity in the CHANTI with the event time will be determined only by CHANTI time resolution σ_t. If we think of a 10 ns window ($\pm 5\sigma_t$) around the event t_0 and recall that we will measure activity in the CHANTI with about 3 MHz rate (accounting for both inelastic events and muon halo) one can state a conservative

estimate of 3-4% fake veto introduced by CHANTI. This could be further reduced if appropriate algorithms to identify muon halo events are implemented, exploiting the tracking capabilities of the system.

Conclusions

As many time stressed in this thesis, my work was essentially focussed on the design, development and construction of two among the different detectors of NA62 apparatus, namely LAV and CHANTI.

LAV is a crucial detector into the general framework of the experiment. Its inefficiency in photon detection (10^{-4} for γ energy above 50 MeV) and time resolution (better than 1 ns) are crucial parameters for NA62. Thus a long R&D program was developed and three different technologies were compared:

- KLOE-like: a prototype was designed and constructed, consisting of a U shaped module made of a matrix of scintillating fibers in lead,
- CKM tile: a small prototype was loaned by Fermilab; it consists of a sandwich of lead and scintillating tiles read by WLS fibers,
- exOPAL: it consists of 25 lead glass blocks arranged to assure that at least three blocks are involved in a single particle detection.

The three prototypes were tested using an electron beam of energies in the range from 300 to 500 MeV. The inefficiency, time resolution and energy resolution requirements were accomplished by all of them. Even if KLOE-like prototype showed better performances we chose, for cost reasons, the exOPAL lead glass solution as our base line .

Once the technology was fixed, an operative design was developed for mechanics and Front End Electronics (FEE). As LAV is mainly a veto system, there are no strong requirements on energy resolution ($10\%/\sqrt{E((\mathrm{GeV}))}$), so a simple FEE electronics, based on the Time over Threshold (ToT) concept can be used.

In order to build all 12 station, $\sim$2500 blocks are needed. Unfortunately in February 2008 there was a flood that compromised the blocks usefulness. A recovery procedure was setup and about 1800 of a total amount of $\sim$3400 blocks have been routinely treated until now. During this routine we found that about 20% of counters shown irreparable damages (discharging and broken blocks). Fortunately if these will be the final percentage we still have enough blocks for all 12 stations.

The production line of LAV station was started in June 2009. The first module, called ANTI-A1, was build and tested. Both charge (Q) and time (T) signal measurements were performed in order to validate the ToT. First results showed that the Q versus T relation is not single valued. The source of this abnormal behaviour, potentially harmful, was found and cured substituting all the PMT voltage dividers.

Even the second module (ANTI-A1) was built and tested. Preliminary analysis of the test data does not show any multivalued curve.

The third module is next to be ultimated, and the time schedule for the remaining stations has been fixed.

For what concerns CHANTI, a lot of work has been done. Final realization is planned to start in 2011. However we have the design, all the tools, part of materials and a full scale of prototype.

CHANTI aims to veto inelastic events produced on GTK3 that could mimic the signature of the decay we are looking for if a pion is produced in such kind of events and no other particles are detected. The basic CHANTI structure is a triangular shape scintillating bar read by a WLS fiber coupled to a SiPM.

Each detail has been carefully studied. To do that a MC simulation was developed in GEANT4. It helps us to fix safety working conditions for SiPM. This device is sensible to neutron flux and the figure of merit is the neutron fluence (1 MeV neutron equivalent flux). We have estimated this parameter to be 1.25×10^{8} neq cm^{-2} y^{-1} (for y=year we intend an equivalent "data taking year"). However we found in literature that SiPM begin to show problems (mainly they start to increase the dark rate) if the integrated fluence reach 4×10^{8} neq cm^{-2}, so CHANTI will be able to run in a safety mode at least for 2 years. MC helps also to estimate data and fake rates which are constrained by Data Acquisition System (DAQ). In order to estimate data rate we have to know the mean firing bars multiplicity and the detector rate (defined as the rate of events in which at least 1 bar fires). Using MC we estimated a data rate of 34.3 MB/s well below DAQ limits. Fake veto due to real energy deposit in coincidence with no inelastic events contributes by less than 0.3%. This means that real fake veto will be dominated by accidental coincidence of detector rate and trigger gate. Once main questions were solved, and technology was chosen, a full size XY prototype was designed and built. It adopts some custom solutions like the SiPM connector, developed in order to have the best alignment between fiber and SiPM active area (reducing the light loss), or jig used to align bars during gluing operations. Finally some preliminary tests have been done on the prototype. In particular we have a preliminary time resolution estimation for a bar couple: $\sim$770 ps. Moreover we have found that there is no difference if ToT or charge correction are applied.

Appendix A

Solid State Photon Detector

A.1 Introduction

Silicon photon detectors nowadays are a useful solution in many applications. Their development began in 1940 when at Bell Telephone Labs, Russel Ohl discovered p-n junction in silicon. Almost twenty years later first silicon photon detector was born. It was an intrinsic piece of high-ohmic semiconductor sandwiched between two heavily doped n+ and p+ so a p-i-n junctions (then called PIN). This configuration produces a field, which, even without an external field supplied, will tend to separate charges (electron-hole couples), produced by incident photons, in the depleted region. The separated charges will be swept to the terminals and detected as current. Their sensitivity is limited to several (hundreds) of incident photons. PIN with areas of 10 cm^2 and more are nowadays available, and it is easy to fabricate position sensitive devices using PIN arrays with a large number of elements.

A step towards increase sensitivity to incident light, was the APD (Avalanche PhotoDiode). It was the first silicon device with of internal signal amplification (50→200). APD compared with PIN increases photon sensitivity by 2 orders of magnitude (dozen of photoelectrons).

In 60s Geiger-mode APD (G-APD) was designed and realized for first time. It was first silicon device with single photoelectron capabilities. But only at beginning of this century last step was done: arrange single G-APD pixels into bigger sensors. Nowadays these devices are competitive if compared with PhotoMultiplier Tubes (PMTs). If compared with PMT they have a comparable gain and wavelength bandwidth; for this reason are called also Silicon PhotoMultiplier (SiPM).

Here we will discuss about APD and SiPM within main features. Some measurements will be also presented as a feasibility study for a scintillator readout based on SiPM technology.

A.2 Photon detectors with internal gain

In this section we will briefly discuss about APD in order to introduce Silicon Photomultipliers.

A.2.1 Avalanche PhotoDiode (APD)

The APD was the first silicon photon detector able of internal gain. An APD is a p-n junction with internal gain. Signal is amplified by high value of internal field reached

near the junction. In an APD, a photoelectron in this field gains enough energy to create an electron-hole pair by impact ionization; both the initial electron and the additional electron again undergo high acceleration and can initiate further electron-hole pairs, thus starting an avalanche. For what concern holes, if the electrical field is not too high, the accelerated holes do not gain enough energy to create e-h pairs in addition, or else the process runs out of control and a breakdown can occur.

There are many theories describing impact ionization. It is generally accepted that the electric field must reach a critical value [41], called the impact ionization threshold, which is approximately 1.75×10^5 V/cm for silicon, before electrons can gain sufficient kinetic energy to generate electron-hole pairs [37]. The field strength for holes to generate impact ionization is around 2.5×10^5 V/cm [29].

The APDs are realized in three different architectures: beveled edge, reach-through and reverse APD. We will discuss briefly only about the last one, for those interested to the other see [41].

In Figure A.1 is scratched a scheme of a reverse APD used in CMS experiment [23]. A structural low resistive silicon layer is the bulk, on top of which an epitaxial grown layer of low doped n-silicon is placed. In this top layer with a thickness of 50 μm, the p-n junction is created by ion implantation at a depth of $\sim$ 5 μm, here high filed value is reached. About 40 μm of the epitaxial grown layer of low doped n-silicon remains unaltered and acts only as a drift region but this reduces the capacitance and, consequently, the noise of the device. A groove close to the edge of the device prevents the flow of surface currents.

The size of APDs is limited due to the production yield to achieve an extremely uniform field distribution over the sensitive area. The biggest area available commercially is 2.5 cm^2.

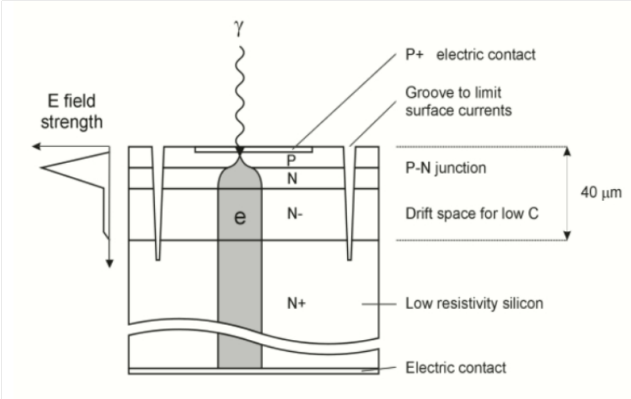

Figure A.1: Schematic of a Hamamatsu S8148 APD.

A.2.2 Geiger-mode Avalanche PhotoMultiplier (G-APD)

At the beginning of this millennium the Geiger-mode Avalanche PhotoDiode (G-APD) has been developed.

Geiger-mode describes the feature of these devices whereby a photo-generated carrier in the depletion region can trigger a diverging avalanche multiplication of carriers by impact ionization. Both positive and negative carriers are involved with a positive feedback effect, which, when the electric field is high enough, makes the carrier multiplication self-sustaining. In linear mode APDs, avalanches develop basically only in one direction (from the p- towards the n-material) and stop multiplying when the charge carriers reach the low field area of the n-zone. Very rarely are secondary avalanches started by holes or secondary photons in the p-layer. In G-APDs, the essential new process is the additional initiation of secondary avalanches, triggered by holes and secondary photons in the p-layer. A G-APD, therefore, does not turn off by itself and, as a consequence, the avalanche process must be quenched by the voltage drop across a high-ohmic serial resistor or by an active quenching circuit. For a G-APD avalanche multiplication could be obtained because it works with a reverse bias well above the breakdown voltage, in a way that completely differs from normal APD, operated below the breakdown level. Operational voltage is called bias voltage (V_{bias}) and is above breakdown value, field strength at bias working point is about $3{\times}10^5$ V/m [43]. In this configuration the device is in a critical status, any production of electron-hole couple (by photons or thermally generated) in depleted volume cause a discharge. It is obvious that large depleted volumes with a high electrical field could never be kept biased sufficiently long in time well over the breakdown voltage because sufficient free electrons would always be thermally generated. Due to improved technologies it was possible to keep the depleted volume free of electrons for sufficiently long time biased well above breakdown. The development led to the so-called Single Photon Avalanche Diode (SPAD).

A logical next step was to try to combine many small cells operated in the Geiger mode on a single wafer and either to use an external quenching element or to integrate it directly onto the wafer either near or directly onto the individual cells.

This device can detect single photon like a PMT, with a comparable gain and therefore it is also called Silicon PhotoMultiplier (SiPM). A magnification of a SiPM surface is in Figure A.2.

The quenching of the breakdown was done passively by adding a high-ohmic ($\sim$150kΩ) series resistor.

A.3 Main SiPM features and physical phenomena

A.3.1 Photon Detection Efficiency (PED) and Gain

The PDE is the product of a) quantum efficiency (QE) of the active area, b) geometric fill factor ε (ε = ratio of sensitive to total area) and c) probability that an incoming photon triggers a breakdown ($P_{trigger}$). A small correction that the hit

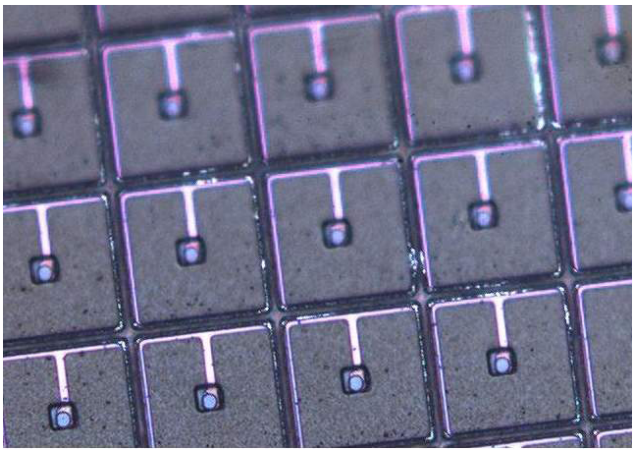

Figure A.2: Magnification of a SiPM surface, pixel structure is clearly evident.

cell is still recovering from a previous breakdown (from noise or a previous light signal) is neglected in current discussions:

$$PDE = QE \cdot \varepsilon \cdot P_{trigger} \tag{A.1}$$

The geometric factor ε needs to be optimized depending on the application. The QE of the active area can reach 80 to 90% depending on the wavelength.

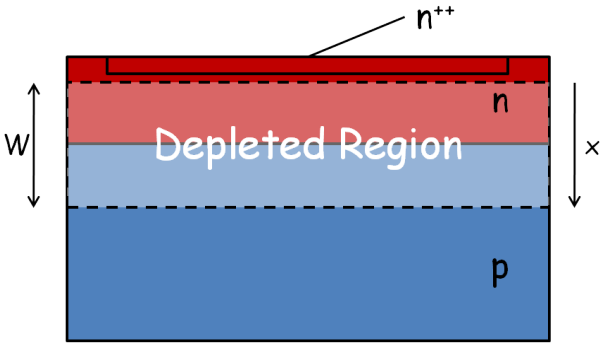

Figure A.3: Depleted region width and position variable definition.

The avalanche triggering probability is defined as the probability that a hole-electron pair trigger a self-sustaining avalanche. If $P_n(x)$ is the probability that an electron starting from the position x inside the depletion volume with the width W triggers a breakdown (Figure A.3) and $P_p(x)$ is the same probability for holes. We can define $P_n(x)$ as the probability that an electron, starting from a position x trigger a breakdown, and $P_p(x)$ the same probability for the holes [36]. Then the probability that at least one between electrons and holes trigger an avalanche is $P_{pair}=P_n+P_p-P_nP_p$. Now consider the probability that an electron generated in

$x + \Delta x$ (then electron travel from $x + \Delta x$ to x) trigger an avalanche, it is the sum of three terms:

1. the probability that the electron trigger an avalanche in x: P_n,
2. the probability that the electron ionize going from $x + \Delta x$ to x, it is the ionizing probability $\alpha_n \delta x$ (were α_n is the ionization parameter) multiplied the probability that the generated pair will trigger an avalanche, we obtain: $\alpha_n \delta x \ \mathrm{P}_{pair}$
3. moreover the electron can trigger only one of these two processes, then the coincidence probability of these two events must be subtracted: $\mathrm{P}_n \ \alpha_n \delta x \ \mathrm{P}_{pair}$

in conclusion we have:

$$P_n(x + \Delta x) = P_n(x) + \alpha_n \Delta x P_{pair} - P_n \alpha_n \Delta x P_{pair} \tag{A.2}$$

differentiating we obtain:

$$\frac{dP_n}{dx} = (1 - P_n) \cdot \alpha_n \cdot (P_n + P_p - P_n \cdot P_p) \tag{A.3}$$

A similar equation can be found for holes:

$$\frac{dP_p}{dx} = -(1 - P_p) \cdot \alpha_p \cdot (P_n + P_p - P_n \cdot P_p) \tag{A.4}$$

The total triggering probability P_{pair} can be calculated by integrating the equations with the boundary conditions that $\mathrm{P}_n(0)$=0 and $\mathrm{P}_p(\mathrm{W})$=0 (the probability to trigger a breakdown is zero for carriers exiting the high field region). P_t depends on the shape of the electric field and hence on the doping profiles. It always increases with the applied excess bias voltage (Figure A.4).

Signal from SiPM is proportional to the number of firing cells. Single cell signal is always the same (because breakdown occurs) for a fixed V_{ex}, the amplitude A_i is proportional to the capacitance of the cell divided by the electron charge times the overvoltage.

$$A_i \sim \frac{C}{q \cdot V_{ex}} \tag{A.5}$$

V_{ex} is the excess voltage (V-V_b; V is the operating bias voltage and V_b is the breakdown voltage). In general single cell signal amplitude is few millivolts (with a load of 50Ω) and for many applications no more amplification is needed. If many cells fire at same time the signal is the sum of standard response A_i. Of course the output signal is proportional to the number of firing cells as long as the number of photons in a pulse (N_{photon}) times the PDE, is significant smaller than the number of cells N_{total}. If two or more photons, which convert within the same time in one cell, produce exactly the standardized signal of 1 single photon. For example if the number impinging photons times the PDE exceeds 50% of the available cells, the

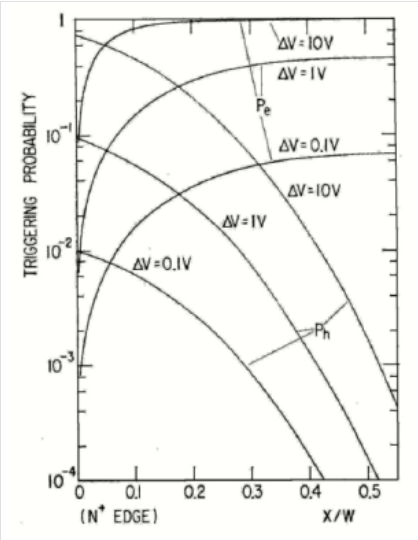

Figure A.4: Avalanche trigger probability for electrons and holes for different values of V_{ex}.

deviation from linearity is more than 20%. Equation A.6 is not exact but describes the data very well.

$$A \sim N_{firedcells} = N_{total} \cdot (1 - e^{-\frac{N_{photon} \cdot PDE}{N_{total}}}) \tag{A.6}$$

Gain is typically in the range of 10^5 to 10^6.

The breakdown voltage V_b strongly depends on the junction temperature and therefore the gain. The thermal coefficient value depends on the SiPM device structure. At a constant supply voltage V, the increase of V_b causes a decrease of the V_{ex} which in percentage is greater than that of V_b by the factor V_b/V_{ex}. The resulting percent variation of V_{ex} is very strong at low V_{ex} level, about 30%/°C, and fairly high also at high V_{ex} level, about 3%/°C. The resulting effects on the device performance are strong.

A.3.2 Dark current, afterpulses and optical cross talk

In a SiPM, thermally generated carriers trigger the avalanche and produce output current pulses even when the device is kept in dark conditions. The mean value of the output pulse rate is called dark count rate. Dark rate is in the rage from 0.1 to 1 MHz per mm^2 at 25°C and with a threshold at half of the one photon amplitude. Of course dark rate falls dramatically with temperature (about a factor 2 every 8°C) and increasing the threshold of the readout electronics.

In an avalanche breakdown, there are on average 3 photons emitted per 10^5 carriers with photon energy higher than 1.14 eV (the band gap of silicon) [28]. When these photons travel to a neighboring cell they can trigger a breakdown there. This

effect is called optical cross talk. Therefore we have a dark count spectrum that could be used to measure SiPM gain.

In the silicon volume where a breakdown happened a plasma with high temperatures (a few 1000°C) is formed and deep-lying traps in the silicon are filled. Carrier trapping and delayed release causes afterpulses during a period of several 100 nanoseconds after a breakdown.

Figure 4.13 shows dark signals and also afterpulses are visible.

A.3.3 Nuclear counter effect and radiation hardness

Solid state photon detectors suffer for energy release of ionizing particles passing through depleted region. This is called Nuclear Counter Effect (NCE). In particular in a SiPM a breakdown is triggered only in the cell crossed by particle. The signal looks exactly like the signal produced by a single photon, therefore due to SiPM pixel segmentation the NCE is negligible.

However when a silicon device needs to operate in a harsh radiation environment, its radiation hardness also need to estimated. Some works could be find in literature concerning different kind of radiation (gammas [32], neutrons [34], protons [38] and electrons [39]). Hadrons create defects in the bulk silicon, which act as generation centers, and the dark current, the dark count rate and the afterpulsing probability will increase during an irradiation.

A.3.4 Signal shape

The signal rise time is determined by the resistance of the silicon in the breakdown channel, the space charge, the resistance of neutral regions and the parasitic capacitance of the whole device, which is 2 orders of magnitude higher than the capacitance of one single cell (∼10fF). The recharging of the cells defines the signal fall time. The time needed to recharge a cell after a breakdown has been quenched, depends mostly on the cell capacitance and the individual quenching resistor ($\tau \sim$ RC).

These devices show a short peak with a duration of 2 to 3 ns followed by a slow tail due to the recharging of the cell (Figure A.5).

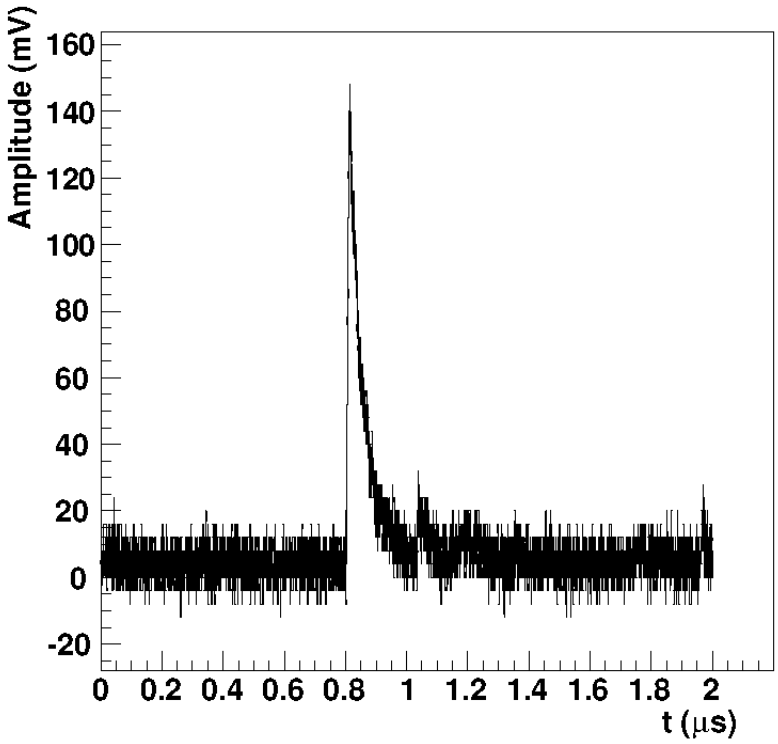

Figure A.5: Signal from a Hamamatsu SiPM (amplified 10×).

Bibliography

[1] http://ttc.web.cern.ch/ttc/intro.html.

[2] http: //www.detectors.saint-gobain.com.

[3] http: //sales.hamamatsu.com/en/products/solid-state-division/si-photodiode-series/mppc.php.

[4] http: //outgassing.nasa.gov/.

[5] S. et al. Adler. Measurement of the $k^+ \to \pi^+\nu\bar{\nu}$ branching ratio. *Phys. Rev. D*, 77(5):052003, Mar 2008.

[6] K. Ahmet et al. The OPAL detector at LEP. *Nucl. Instrum. Meth.*, A305:275–319, 1991.

[7] J. K. et al. Ahn. Search for the decay $k_L^0 \to \pi^0\nu\bar{\nu}$. *Phys. Rev. Lett.*, 100(20):201802, May 2008.

[8] A Ali. Ckm phenomenology and b-meson physics: Present status and current issues. oai:cds.cern.ch:694214. (hep-ph/0312303. KEK-TH-928):66 p, Dec 2003.

[9] G. Anelli et al. Proposal to measure the rare decay $K^+ \to \pi^+\nu\bar{\nu}$ at the CERN SPS. CERN-SPSC-2005-013.

[10] M. Angelone, M. Pillon, R. Faccini, D. Pinci, W. Baldini, R. Calabrese, G. Cibinetto, A. Cotta Ramusino, R. Malaguti, and M. Pozzati. Silicon Photo-Multiplier radiation hardness tests with a beam controlled neutron source. *ArXiv e-prints*, February 2010.

[11] B. Angelucci et al. Pion-muon separation with a RICH prototype for the NA62 experiment. *Nucl. Instrum. Meth.*, A621:205–211, 2010.

[12] Mario Antonelli et al. Flavor physics in the quark sector. *Phys. Rept.*, 494:197–414, 2010.

[13] M. Battaglia et al. The CKM matrix and the unitarity triangle. Workshop, CERN, Geneva, Switzerland, 13-16 Feb 2002: Proceedings. 2003.

[14] B. Bencheikh, R. DeSalvo, W. Hao, C. Xu, and K. You. A simple light detector gain measurement technique. *Nucl. Instrum. Methods A*, 315(1-3):349 – 353, 1992.

[15] D. Beznosko, A. Bross, A. Dyshkant, A. Pla-Dalmau, and V. Rykalin. FNAL-NICADD extruded scintillator. Prepared for 2004 IEEE Nuclear Science Symposium and Medical Imaging Conference (NSS / MIC), Rome, Italy, 16-22 Oct 2004.

[16] Gerhard Buchalla and Andrzej J. Buras. $k \to \pi\nu\bar{\nu}$ and high precision determinations of the ckm matrix. *Phys. Rev. D*, 54(11):6782–6789, Dec 1996.

[17] Andrzej J. Buras, Selma Uhlig, and Felix Schwab. Waiting for precise measurements of $k^+ \to \pi^+\nu\bar{\nu}$ and $k_l \to \pi^0\nu\bar{\nu}$. *Rev. Mod. Phys.*, 80(3):965, Aug 2008.

[18] Vincenzo Cirigliano and Ignasi Rosell. Two-loop effective theory analysis of $\pi(k) \to e\bar{\nu}_e\gamma$ branching ratios. *Phys. Rev. Lett.*, 99(23):231801, Dec 2007.

[19] D0 collaboration. The upgraded d0 detector. *Nucl. Instrum. Methods A*, 565:413, 2006.

[20] MINERVA collaboration. The physics case and technology of the minerva experiment. *MINERvA Document*, 218, 2006.

[21] NA48 Collaboration. The beam and detector for the na48 neutral kaon cp violation experiment at cern. *Nucl. Instrum. Methods A*, 574(3):433 – 471, 2007.

[22] G. D'Ambrosio, G. F. Giudice, G. Isidori, and A. Strumia. Minimal flavour violation: An effective field theory approach. *Nucl. Phys.*, B645:155–187, 2002.

[23] K. Deiters, Y. Musienko, S. Nicol, B. Patel, D. Renker, S. Reucroft, R. Rusack, T. Sakhelashvili, J. Swain, and P. Vikas. Properties of the most recent avalanche photodiodes for the cms electromagnetic calorimeter. *Nucl. Instrum. Methods A*, 442(1-3):193 – 197, 2000.

[24] M. Adinolfi et al. The kloe electromagnetic calorimeter. *Nucl. Instrum. Methods A*, 482(1-2):364 – 386, 2002.

[25] M. Antonelli et al. *CERN report*, 002, 2003.

[26] J. Frank et al. Charged Kaons at the Main injector (CKM): A proposal for a precision measurement of the decay $K^+ \to \pi^+\nu\bar{\nu}$ and other rare K^+ processes at Fermilab using the Main Injector. FERMILAB-PROPOSAL-0921.

[27] Ruggiero G. Measurement of the lkr calorimeter inefficiency using na48/2 data. *Nucl. Instrum. Meth.*, A621:205–211, 2010.

[28] A.L. Lacaita, F. Zappa, S. Bigliardi, and M. Manfredi. On the bremsstrahlung origin of hot-carrier-induced photons in silicon devices. *Electron Devices, IEEE Transactions on*, 40(3):577 –582, mar. 1993.

[29] C. A. Lee, R. A. Logan, R. L. Batdorf, J. J. Kleimack, and W. Wiegmann. Ionization rates of holes and electrons in silicon. *Phys. Rev.*, 134(3A):A761–A773, May 1964.

[30] M. Lenti. The NA62 RICH detector. *Nucl. Phys. Proc. Suppl.*, 197:117–120, 2009.

[31] A. Masiero, P. Paradisi, and R. Petronzio. Probing new physics through μ e universality in K $\to$ l ν. *Phys. Rev.*, D74:011701, 2006.

[32] T Matsubara. Radiation damage of mppc by γ-ray irradiation with co 60. *PoS*, PD07:032, 2007.

[33] T Matsumura. Radiation damage to mppcs by irradiation with protons. *PoS*, PD07:033, 2007.

[34] T Matsumura. Radiation damage to mppcs by irradiation with protons. *PoS*, PD07:033, 2007.

[35] G. Mazzitelli, A. Ghigo, F. Sannibale, P. Valente, and G. Vignola. Commissioning of the da[phi]ne beam test facility. *Nucl. Instrum. Methods A*, 515(3):524 – 542, 2003.

[36] R.J. McIntyre. On the avalanche initiation probability of avalanche diodes above the breakdown voltage. *Electron Devices, IEEE Transactions on*, 20(7):637 – 641, jul. 1973.

[37] R.J. McIntyre. A new look at impact ionization-part i: A theory of gain, noise, breakdown probability, and frequency response. *IEEE Trans. Electron. Dev.*, 46:1632 – 1639, 1999.

[38] Y. Musienko, D. Renker, Z. Charifoulline, K. Deiters, S. Reucroft, and J. Swain. Study of radiation damage induced by 82 mev protons on multi-pixel geiger-mode avalanche photodiodes. *Nucl. Instrum. Methods A*, 610(1):87 – 92, 2009. New Developments In Photodetection NDIP08, Proceedings of the Fifth International Conference on New Developments in Photodetection.

[39] Y. Musienko, D. Renker, S. Reucroft, R. Scheuermann, A. Stoykov, and J. Swain. Radiation damage studies of multipixel geiger-mode avalanche photodiodes. *Nucl. Instrum. Methods A*, 581(1-2):433 – 437, 2007. VCI 2007 - Proceedings of the 11th International Vienna Conference on Instrumentation.

[40] Palladino V. on behalf of NA62 photon veto working group. Searches for new physics at na62. *Proceeding prepared for the 14th Lomonosov Conference*, 2009.

[41] D. Renker and E. Lorenz. Advances in solid state photon detectors. *JINST*, 4:P04004, 2009.

[42] F. Ronchetti. The ALICE electromagnetic calorimeter project. *J. Phys. Conf. Ser.*, 160:012012, 2009.

[43] S.M. Sze. *Physics of Semiconductor Devices.* J. Wiley and Sons, 1981.

[44] Lkr calorimetry for the cp violation experiment na48: recent test beam results. *Nucl. Instrum. Methods A*, 360(1-2):224 – 227, 1995. Proceedings of the Sixth Pisa Meeting on Advanced Detectors.

[45] Lincoln Wolfenstein. Parametrization of the kobayashi-maskawa matrix. *Phys. Rev. Lett.*, 51(21):1945–1947, Nov 1983.